

122 GHz SiGe BiCMOS High Resolution FMCW  
RADAR Front-End for Remote Sensing  
Applications

by

Işık Berke Güngör

Submitted to the Graduate School of Engineering and Natural Sciences  
in partial fulfillment of  
the requirements for the degree of  
Master of Science

Sabancı University

Summer, 2020

122 GHz SiGe BiCMOS High Resolution  
FMCW RADAR Front-End for Remote Sensing Applications

APPROVED BY

Prof. Dr. Yaşar GÜRBÜZ  
(Thesis Supervisor)



.....

Asst. Prof. Dr. Melik YAZICI



.....

Assoc. Prof. Dr. Mehmet ÜNLÜ



.....

DATE OF APPROVAL: ..... 14.08.2020 .....

© Işık Berke G ng r 2020

All Rights Reserved

## Acknowledgements

First and foremost, I would like to thank my supervisor Prof. Yaşar Gürbüz for his invaluable support and motivation, starting from my sophomore year as my instructor and as my supervisor during my master's studies. His constant support and endless motivation have pushed me to improve myself to become a worthy researcher.

I would also like to thank Asst. Prof. Melik Yazıcı and Assoc. Prof. Mehmet Ünlü for taking their time to serve in my thesis committee, and for their precious comments and feedback.

I would like to thank all SUMER group members, Dr. Melik Yazıcı, Dr. Ömer Ceylan, Dr. Can Çalışkan, Abdurrahman Burak, Tahsin Alper Özkan, Mir Hassan Mahmud, Cerin Ninan Kunnatharayil, Umut Barış Göğebakan for creating a wonderful working environment, including the past members Dr. İlker Kalyoncu, Eşref Türkmen, Elif Gül Arsoy, Emre Can Durmaz, Alper Güner, and Atia Shafique. I would like to give special thanks to my comrade designer Hamza Kandış, for his effort in this thesis work as well as our collaborations in past works. I would also like to thank the laboratory specialist Ali Kasal for his help and support. In addition, thanks to Şeyma, Güneş, Murat, Jerfi, Orkun, and others for their friendship during my university and high school years.

Most importantly, I would like to express my deepest gratitude to my parents and family. I thank my mother Zerrin and my father Melikşah for their unconditional love, support, and motivation. I can not thank them enough for their patience, guidance, and the sacrifices they have made throughout my life.

# 122 GHz SiGe BiCMOS High Resolution FMCW RADAR Front-End for Remote Sensing Applications

Işık Berke Güngör

EE, Master's Thesis, 2020

Thesis Supervisor: Prof. Dr. Yaşar GÜRBÜZ

Keywords: FMCW, 122 GHz RADAR, short range RADAR, high resolution, SiGe BiCMOS, mm-wave Integrated Circuits.

## Abstract

RADAR systems are starting to see many new areas applications, becoming a part of our everyday life in our automobiles, cell phones, and more. The constant advances in the Silicon-based process technologies, such as SiGe BiCMOS and deep scaled CMOS, paved the way for the implementation of low-cost, highly integrated systems that work in millimeter-wave frequencies (30-300 GHz). The use of this frequency spectrum enables high-resolution sensing applications such as hand-gesture recognition, human gait tracking, vital sign detection, and imaging with the use of RADARs.

In this thesis, a 122 GHz FMCW RADAR Front-End is designed for high-resolution sensing applications. The designed system employs differential architecture and can operate in both the 122 GHz ISM band, and at an increased bandwidth of 110-130 GHz for sub-cm range resolution performance. The designed system is implemented using IHP 0.13 $\mu$ m SiGe:C BiCMOS technology, which offers HBT devices with  $f_t/f_{max}$  of 300/500 GHz. The system consists of an LNA, PA, Mixer, LO buffer amplifier, x16 active frequency multiplier, and a single-ended to differential power divider. The simulation results of the full system show 31 dB receiver conversion gain, 9.9 dB single-sideband noise figure, 10.1dBm output power with a DC power consumption of 247 mW. The full system occupies a die area of 4mm<sup>2</sup>, and is suitable for scalable implementations in future. The system simulations verify that the designed system can reliably detect a human hand at a range longer than 1m with a sub-cm range resolution.

# Kısa Mesafe RADAR Uygulamaları için Yüksek Çözünürlüklü 122 GHz SiGe BiCMOS FMCW RADAR Ön Uç Devresi

Işık Berke Güngör  
EE, Yüksek Lisans Tezi, 2020  
Tez Danışmanı: Prof. Dr. Yaşar GÜRBÜZ

Anahtar Kelimeler: Frekans Modülasyonlu Sürekli Dalga, 122 GHz RADAR, Kısa mesafe RADAR, SiGe BiCMOS, milimetre dalga boyunda entegre devre.

## Özet

RADAR sistemleri birçok yeni uygulama alanlar görerek otomobillerimizde, cep telefonlarımızda ve daha fazlasında günlük hayatımızın bir parçası haline gelmektedir. SiGe BiCMOS ve derin ölçekli CMOS gibi Silikon bazlı proses teknolojilerindeki devamlı gelişmeler, milimetre dalga frekanslarında (30-300 GHz) çalışan düşük maliyetli, yüksek seviyede entegre sistemlerin yolunu açtı. Bu frekans spektrumunun kullanımı, el hareketi tanıma, insan yürüyüşü izleme, yaşamsal belirti algılama ve RADAR kullanımıyla görüntüleme gibi yüksek çözünürlüklü algılama uygulamalarına olanak tanımaktadır.

Bu tezde, yüksek çözünürlüklü algılama uygulamaları için 122 GHz merkezli bir FMCW RADAR ön-uç devresi tasarlanmıştır. Tasarlanan sistem, diferansiyel mimari kullanır ve hem 122 GHz ISM bandında hem de <1cm aralık çözünürlüğü performansı için 110-130 GHz bant genişliğinde de çalışabilir. Tasarlanan sistem, 300/500 GHz  $f_t/f_{max}$  ile HBT aygıtları sunan IHP 0.13 $\mu$ m SiGe: C BiCMOS teknolojisi kullanılarak üretime gönderildi. Sistem bir LNA, PA, Mikser, LO yükseltici, x16 aktif frekans çarpanı ve diferansiyel güç bölücüsünden oluşur. Tam sistemin simülasyon sonuçları 31 dB alıcı dönüştürme kazancı, 9.9 dB tek yan bant NF, ve 247 mW DC güç tüketimi ile 10.1dBm çıkış gücü göstermektedir. Tam sistem 4mm<sup>2</sup>'lik bir kırmık alanı kaplar ve gelecekte ölçeklenebilir uygulamalar için uygundur. Sistem simülasyonları, tasarlanan sistemin 1 m'den daha uzun bir mesafeden bir insan elini <1 cm bir aralık çözünürlüğü ile güvenilir bir şekilde algılayabildiğini doğrular.

# Contents

<b>Acknowledgements</b>	<b>iv</b>
<b>Abstract</b>	<b>v</b>
<b>List of Figures</b>	<b>x</b>
<b>List of Tables</b>	<b>xi</b>
<b>List of Abbreviations</b>	<b>xii</b>
<b>1 Introduction</b>	<b>1</b>
1.1 Brief History of Remote Sensing . . . . .	1
1.2 Microwave Remote Sensing . . . . .	2
1.3 Fundamental RADAR Types . . . . .	5
1.3.1 Mono- and Bistatic RADAR . . . . .	5
1.3.2 RADAR Types by Carrier Modulation . . . . .	7
1.4 SiGe BiCMOS Technology . . . . .	8
1.5 Motivation . . . . .	11
1.6 Organization . . . . .	12
<b>2 FMCW Remote Sensing</b>	<b>13</b>
2.1 FMCW Fundamentals . . . . .	13
2.1.1 Distance Detection . . . . .	17
2.1.2 Range Resolution . . . . .	19
2.1.3 Velocity Detection . . . . .	20
2.1.4 RADAR Equation . . . . .	21
2.1.5 RADAR Cross Section (RCS) . . . . .	23
2.2 High Resolution Sensing . . . . .	23
2.2.1 Micro Doppler Effects . . . . .	25
<b>3 122 GHz High Resolution FMCW Radar Front-End</b>	<b>26</b>
3.1 Detailed Overview of the Designed System . . . . .	26
3.1.1 System Architecture, Specifications and Design Considerations	26
3.1.2 Theoretical Calculations of Possible Target Scenarios . . . . .	29
3.2 Low-Noise Amplifier . . . . .	31
3.2.1 Circuit Design and Implementation . . . . .	31
3.2.2 Simulation Results . . . . .	36
3.3 Down-Conversion Mixer . . . . .	39
3.3.1 Circuit Design and Implementation . . . . .	39
3.3.2 Simulation Results . . . . .	42
3.4 Power Amplifier . . . . .	47
3.4.1 Circuit Design and Implementation . . . . .	47
3.4.2 Simulation Results . . . . .	50
3.5 LO Buffer Amplifier . . . . .	54
3.5.1 Circuit Design and Implementation . . . . .	54
3.5.2 Simulation Results . . . . .	55
3.6 Differential Power Divider and Balun . . . . .	57
3.7 x16 Frequency Multiplier . . . . .	62

3.7.1	Circuit Design and Implementation . . . . .	62
3.7.2	Simulation Results . . . . .	65
3.8	System Implementation and Simulations . . . . .	68
<b>4</b>	<b>Future Work &amp; Conclusion</b>	<b>73</b>
4.1	Summary of Work . . . . .	73
4.2	Future Works . . . . .	73
	<b>References</b>	<b>81</b>

## List of Figures

1	Pigeons wearing cameras, 1903 . . . . .	1
2	Types of Microwave Remote Sensors . . . . .	2
3	Atmospheric attenuation for different conditions of relative humidity (RH) . . . . .	3
4	(a) Jason-3 AMR (b) FPS-117 RADAR and (c) Fully integrated 77-GHz Transceiver . . . . .	5
5	Schematic diagram of a (a) Monostatic RADAR and (b) Bistatic RADAR . . . . .	6
6	BEOL Cross-section view of IHP 0.13 $\mu$ m SiGe BiCMOS SG13G2 technology. . . . .	10
7	(a) A sawtooth-shaped chirp signal with amplitude as a function of time, and (b) its corresponding behavior on the frequency domain. . .	14
8	Transmitted and received signals and the resulting IF signal of a FMCW RADAR using sawtooth modulation. . . . .	16
9	Transmitted and received signals and the resulting IF tone(s) for both single and multiple target detection. . . . .	18
10	Transmitted and received signals and the resulting beat frequencies triangle modulated chirp. . . . .	20
11	The micro-doppler signature of a person for different movements. . .	25
12	The block diagram of the designed system . . . . .	27
13	The schematic of the designed LNA. (Electrical lengths of the transmission lines are given for 122 GHz, R-C sections used for biasing not shown.) . . . . .	32
14	Simulated MAG and NFmin of the designed LNA for different values of collector current density. . . . .	33
15	3D Layout view of the LNA. . . . .	35
16	Layout of the LNA breakout. . . . .	36
17	Simulated gain of the designed LNA. . . . .	37
18	Simulated input and output reflection coefficients of the LNA. . . . .	38
19	Simulated noise figure (NF) and minimum NF of the LNA. . . . .	38
20	Simulated input referred 1 dB compression point of the LNA at 122 GHz. . . . .	39
21	Schematic of the designed Mixer. (Electrical lengths are given for 122 GHz.) . . . . .	41
22	3D Layout view of the designed mixer. . . . .	42
23	Layout of the Mixer breakout. . . . .	43
24	Simulated CG of the mixer at a fixed IF of 20 kHz. . . . .	44
25	Simulated port matchings of the mixer at a fixed IF of 20 kHz. . . . .	45
26	Simulated port-to-port isolations of the mixer. . . . .	45
27	Simulated NF of the designed mixer versus RF frequency. . . . .	46
28	Simulated NF of the mixer versus IF frequency ranging from 50 Hz to 45 kHz in logarithmic scale. . . . .	46
29	The schematic of the designed PA. (Electrical lengths of the transmission lines are given for 122 GHz) . . . . .	49
30	3D Layout view of the designed PA. . . . .	50
31	Layout of the PA breakout. . . . .	51

32	Simulated small-signal gain of the designed PA. . . . .	52
33	Simulated input and output reflection coefficients of the PA. . . . .	52
34	Simulated output referred 1 dB compression point of the PA at 122 GHz. . . . .	53
35	Simulated power added efficiency of the PA at 122 GHz. . . . .	53
36	Schematic of the designed LO Buffer. (Electrical lengths are given for 122 GHz.) . . . . .	54
37	Layout of the Buffer Amplifier integrated into the Mixer's LO input. . . . .	55
38	Simulated small-signal gain of the LO Buffer for various control voltages. . . . .	56
39	Simulated input and output reflection coefficients of the LO Buffer. . . . .	56
40	Simulated output referred 1 dB compression point of the Buffer at 122 GHz. . . . .	57
41	3D Layout view of the Marchand Balun . . . . .	58
42	Simulated phase and amplitude difference of the Marchand Balun. . . . .	58
43	Schematic of the modified Marchand balun structure. . . . .	59
44	3-D Layout view of the Balun-splitter. . . . .	60
45	Simulated phase difference at splitter's outputs. . . . .	61
46	Simulated transmission coefficients of the splitter. . . . .	61
47	The schematic of the designed frequency multiplier. . . . .	63
48	3-D Layout view of the x16 Frequency Multiplier. . . . .	64
49	Layout of the x16 Frequency Multiplier. . . . .	65
50	Input reflection coefficient for the frequency multiplier. . . . .	66
51	Simulated conversion-loss of the multiplier for a fixed input power of 0 dBm. . . . .	66
52	The harmonic spectrum at the output of the frequency multiplier for $f_{rf} = 7.625$ GHz. . . . .	67
53	Full layout of the designed 122-GHz FMCW RADAR Front-End. . . . .	69
54	Receiver conversion gain of the full system for an IF frequency of 10 kHz. . . . .	70
55	Simulated SSB NF of the system for an IF frequency of 10 kHz. . . . .	71
56	Simulated transmitted output power for 0 dBm multiplier input power. . . . .	71
57	Possible measurement setup of the designed system. . . . .	74
58	Antenna in package approach. . . . .	75
59	2x1 Array implementation (Left) 2x2 Array implementation (Right) . . . . .	75

## List of Tables

1	Performance comparison of different semiconductor technologies for radio frequency integrated circuits (Excellent: ++; Very Good: +; Good: 0; Fair: -; Poor: --) . . . . .	9
2	Summary of the required system performance parameters for reliable short-range, high-precision detection. . . . .	30
3	Performance comparison of the designed LNA with previously reported LNAs implemented using silicon processes. . . . .	37
4	Performance comparison of the designed PA with previously reported PAs implemented using silicon processes. . . . .	51
5	Performance comparison of the designed 122 GHz FMCW Front-end with similar reported works in Silicon technologies. . . . .	72

# List of Abbreviations

<b>ADC</b>	Analog to Digital Converter
<b>AFM</b>	Active Frequency Multiplier
<b>BEOL</b>	Back-End-of-Line
<b>BJT</b>	Bipolar Junction Transistor
<b>BV<sub>CEO</sub></b>	Collector-Emitter Breakdown Voltage
<b>CB</b>	Common-Base
<b>CE</b>	Common-Emitter
<b>CMOS</b>	Complementary Metal-Oxide-Semiconductor
<b>CW</b>	Continuous Wave
<b>EBD</b>	Electrical Balance Duplexer
<b>FEOL</b>	Front-End-of-Line
<b>FFT</b>	Fast Fourier Transform
<b>FMCW</b>	Frequency Modulated Continuous Wave
<b>GaAs</b>	Gallium-Arsenide
<b>GaN</b>	Gallium-Nitride
<b>Ge</b>	Germanium
<b>HBT</b>	Heterojunction Bipolar Transistor
<b>IC</b>	Integrated Circuit
<b>IF</b>	Intermediate Frequency
<b>IL</b>	Insertion Loss
<b>InP</b>	Indium-Phosphide
<b>LNA</b>	Low Noise Amplifier
<b>LO</b>	Local Oscillator
<b>MIM</b>	Metal-Insulator-Metal
<b>MIMO</b>	Multiple-input Multiple-output
<b>MOM</b>	Metal-Oxide-Metal
<b>NF</b>	Noise Figure
<b>PA</b>	Power Amplifier
<b>PAE</b>	Power-Added-Efficiency
<b>PLL</b>	Phased Locked Loop
<b>PRN</b>	Pseudo-Random Noise
<b>RADAR</b>	Radio Detecting And Ranging
<b>RCS</b>	RADAR Cross Section
<b>RF</b>	Radio Frequency
<b>RX</b>	Receiver
<b>SAW</b>	Surface Acoustic Wave
<b>Si</b>	Silicon
<b>SiGe</b>	Silicon-Germanium
<b>SNR</b>	Signal to Noise Ratio
<b>TRX</b>	Transceiver
<b>TX</b>	Transmitter
<b>VCO</b>	Voltage Controlled Oscillator
<b>VSWR</b>	Voltage Standing Wave Ratio
<b>WWII</b>	World War II

# 1 Introduction

## 1.1 Brief History of Remote Sensing

The idea of remote sensing dates back to almost two centuries, starting with the development of flight. One of the earliest examples of remote sensing in history is the balloonists of the 1860s using the newly invented camera to become the first aerial photographers [1]. Another relatively famous example of early applications of remote sensing is the pigeon fleet deployed over Europe at the start of the 20th century [2]. Remote sensing saw rapid development in a systematic level following World War I and later, the Cold War.

Remote sensing reached a global scale with the development of first satellites during the Cold War. It was around this time a new method of remote sensing has emerged, namely, microwave remote sensing. Unlike the conventional method of remote sensing until to date, photography, microwaves do not rely on the sun's light for illumination and could penetrate obstructions such as clouds. These unique properties of the microwaves made the use of this technique favorable over the camera.

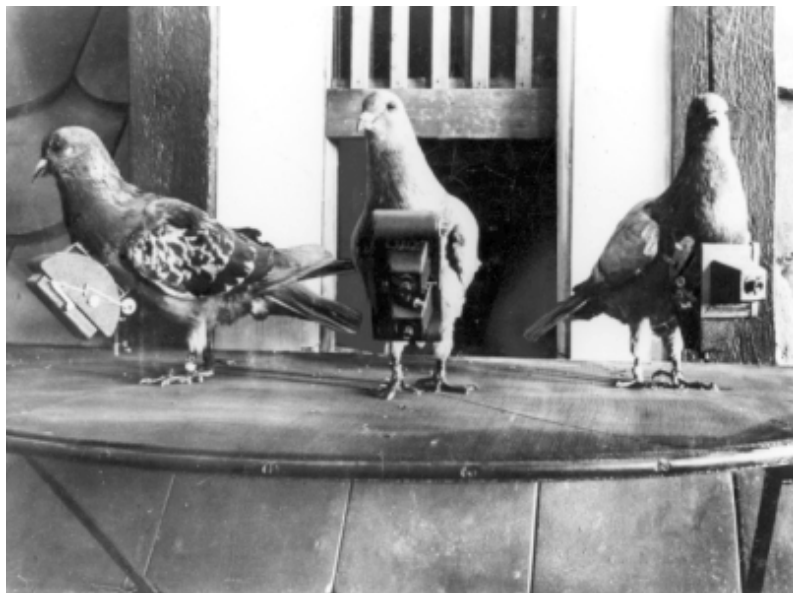


**Figure 1:** Pigeons wearing cameras, 1903 [3]

## 1.2 Microwave Remote Sensing

Microwave remote sensors can be classified into two major categories, separated by their inclusion of an illumination source, as shown in Fig. 2. This illumination source is also defined as the transmitter. Microwave sensors that lack a transmitter are classified as Passive (Radiometers), while the ones that include it are called Active sensors (Radars). Radiometers work on the principle of detecting or sensing the low-level microwave radiations. Since Radiometers lack a transmitter, they rely solely on the detection of the waves emitted from the objects, unlike the active microwave sensors (RADARs), which illuminate their targets with an electromagnetic wave of varying types depending on their classifications. Both active and passive microwave sensors are grouped into sub-classes by the techniques employed to create the aperture. Synthetic aperture systems deploy different antenna-processing methods while real-aperture systems, as the name suggests, use real-aperture antennas. In the interest of brevity, sub-classes of microwave sensors are not discussed in further detail in the scope of this thesis.

Microwave radiation is present in any object with a non-zero temperature, as governed by the Planck's law [5]. This phenomenon is called black-body radiation and creates the basis of passive microwave sensors. Objects with different temperatures and different emissivity characteristics have different levels of black-body radiation. This discrepancy between the objects allows the construction of images once picked up by radiometers [6]. Radiometers have first seen use in the 1930s

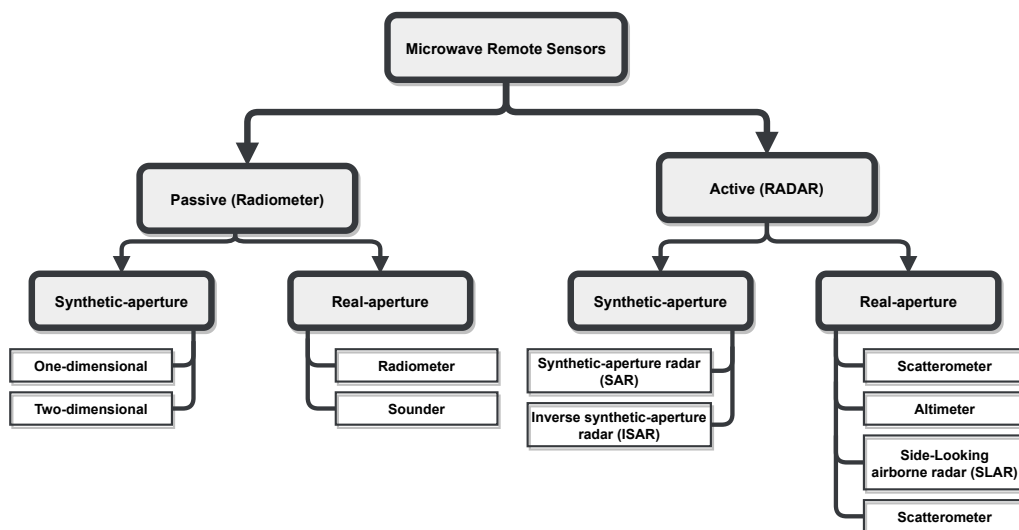
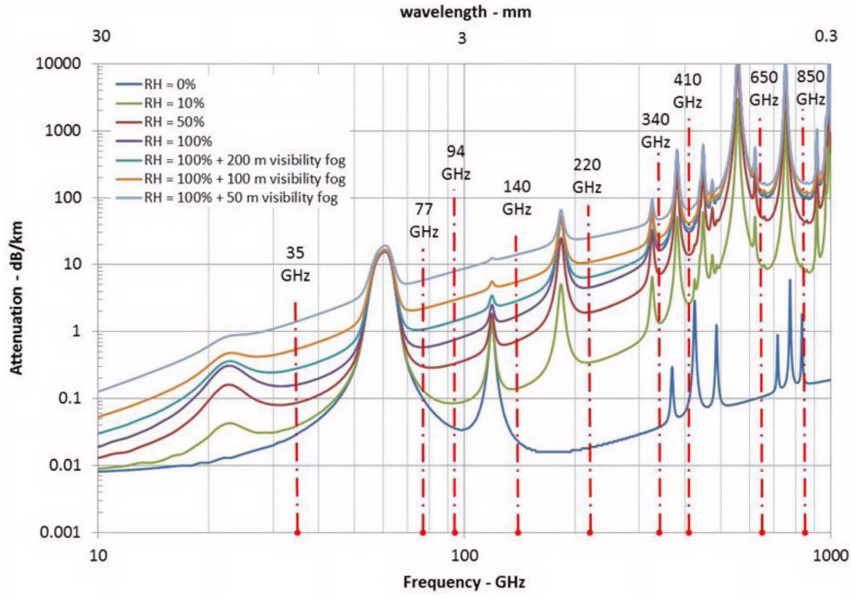


Figure 2: Types of Microwave Remote Sensors [4]



**Figure 3:** Atmospheric attenuation for different conditions of relative humidity (RH)[10].

and are currently see use in applications such as extraterrestrial object observation, surveillance, concealed weapon detection, and non-intrusive imaging.

Active microwave sensors, on the other hand, do not rely on the black-body radiation phenomena. Such sensors, RADARs, send an electromagnetic wave at their targets and collect information from the scattered waves. By collecting these returning waves, RADARs can gather much more detailed information compared to Radiometers, such as distance, velocity, direction, and angle of arrival of the targets [7]. Details on how to acquire such information from the target objects will be explained in Chapter 2. RADAR was invented by Christian Hülsmeyer in 1904 [8], and the first microwave RADAR was invented in MIT Radiation Laboratory during WWII [9]. RADAR systems have seen a diverse range of applications over the years. Starting from the WWII years, one of the primary areas of application for RADAR has been military applications, starting from the detection of planes and ships in WWII. Over the years, significant developments enabled the construction of more advanced RADAR technologies such as phased arrays, SAR imaging radars, and space-borne radars. Towards the end of the 20th century saw the emergence of a new application for RADARs, automotive RADARs.

The constant advances in silicon-based process technologies sparked an ever-growing interest in microwave sensors that operate within the millimeter-wave spec-

trum. Traditionally, circuits centered within the millimeter-wave frequencies, 30 GHz to 300 GHz, were being implemented in III-V technologies such as GaAs, GaN, InP. With the silicon-based technologies starting to become comparable in terms of RF performance, the millimeter-wave spectrum became attractive for civilian applications [11]. Operation within this spectrum comes with significant advantages such as larger bandwidth and smaller die area for increased integration in a single chip. The bandwidth of the system directly translates into the maximum range resolution a RADAR can achieve, allowing millimeter-wave RADARs to detect smaller targets with increased precision. Another major advantage of millimeter-wave frequencies compared to optical remote sensing is the microwaves' ability to operate under harsh conditions such as fog, rain, and dust. These advantages make millimeter-wave frequencies favorable for remote sensing applications. Despite suffering from high free space path loss due to the increased frequency of operation, such applications make use of several windows within the mm-wave spectrum. Fig. 3 shows the atmospheric attenuation in dB/km for different levels of humidity. The peaks in the graphs at frequencies such as 60 GHz and 120 GHz is the result of electromagnetic waves' interaction with water and oxygen molecules [12]. Outdoor remote sensing applications exploit the attenuation windows within the denoted points within in Fig. 3. Modern automotive RADARs utilize the 76-81 GHz band, for purposes such as collision, blind-spot detection, and adaptive cruise control (ACC) in passenger cars [13]. Attenuation windows at 94 GHz and 140 GHz makes the center frequency of W-band (70-110 GHz) [14] and D-band (110-170 GHz) [15] radiometers, respectively. Recently, a new trend for the use of RADARs is the precise detection and the detection of smaller, more complicated targets such as heartbeat and hand gestures, enabled by the larger bandwidth obtained within the mm-wave frequencies [16]. The reduction in the required processing power to detect targets compared to other forms of remote sensing such as cameras, make mm-wave short range RADAR systems attractive for precision detection applications. An example of a modern radiometer and several different RADARs are shown in Fig. 4. (a) Advanced Microwave Radiometer (AMR) that is used to provide tropospheric path delay measurements in support of ocean altimetry, deployed in the Jason-3 Satellite, (b) FPS-117 is a solid-state phased-array long range surveillance radar system, and

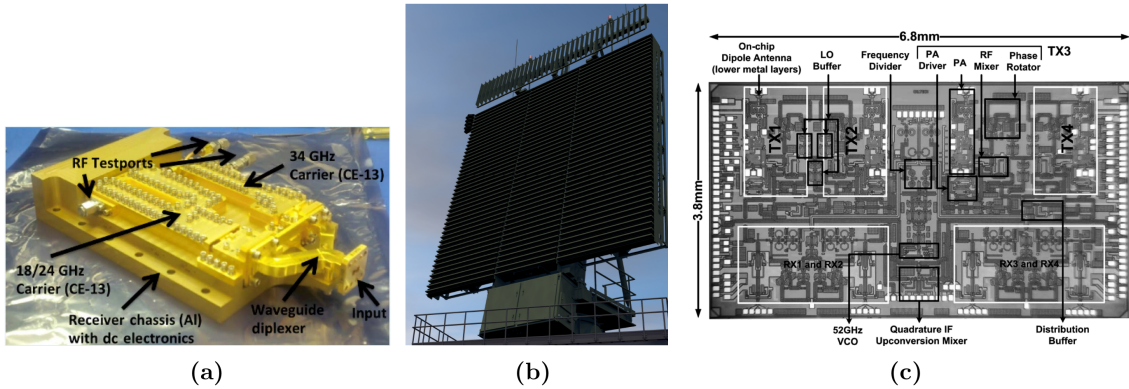


**Figure 4:** (a) Jason-3 AMR [17] (b) FPS-117 RADAR [18] and (c) Fully integrated 77-GHz Transceiver [19]

(c) is a 77-GHz, four-element, single chip transceiver module.

### 1.3 Fundamental RADAR Types

RADAR systems can be classified in various ways with respect to the system architecture, modulation scheme, application area, and frequency of operation. This section aims to provide an overview of the fundamental classes of RADAR systems in two main categories, by architecture and carrier modulation scheme.

#### 1.3.1 Mono- and Bistatic RADAR

RADAR systems are separated into two main groups in terms of architecture, mono- and bistatic. This classification is based on how the antennas of the system are configured. Figure 5 shows a sample system of both Monostatic and Bistatic RADAR transceivers. In Monostatic architecture, both transmit (Tx) and receive (Rx) paths share the same antenna. In Figure 5, the signal splitting between transmitter and receiver is done with the use of a circulator. Ideally, the circulator allows no leakage from the transmit path to the receive path. However, in integrated circuit designs, circulators are very challenging to implement, even more so in the millimeter-wave frequencies. Since circulators are not feasible to implement in those frequencies, alternate solutions such as Rat-race couplers and Electronic Balance Duplexers (EBD) are used to facilitate transmission and reception over a single antenna [20, 21, 22]. These solutions, however, come with several disadvantages, such

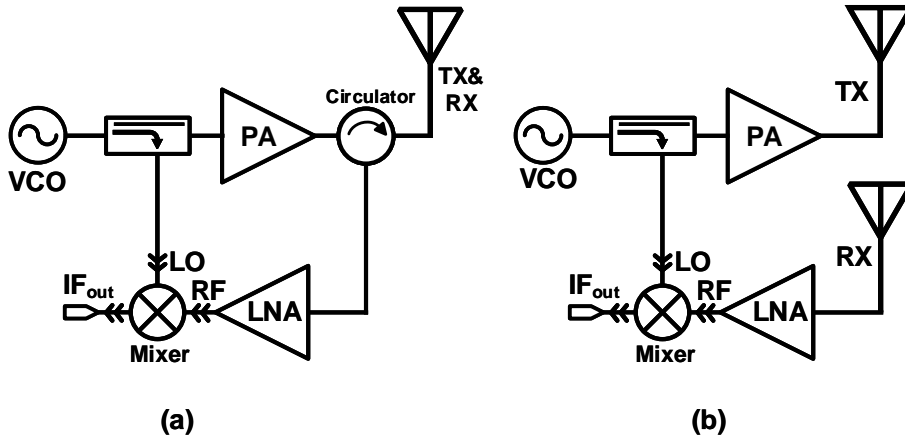


**Figure 5:** Schematic diagram of a sample (a) Monostatic RADAR and (b) Bistatic RADAR

as low Tx-Rx isolation and high insertion loss. Tx-Rx leakage directly affects the receiver sensitivity [23] since the leakage power has the potential to compress the receiver. Usually, an isolation performance of around 40 dB is desirable for monostatic systems. The insertion loss introduced by the component used to split the Tx and Rx signals lowers the transmit output power and also increases the receiver noise figure (NF).

The bistatic configuration is originally defined as a RADAR system where the transmitter and the receiver are in separate places. However, single chip transceivers that do not share the Tx and Rx ports can also be defined as bistatic RADARs, even if the transmitter and receiver are effectively in the same place. These systems include a separate antenna for both transmit and receive paths of the system. Using dedicated antennas usually provide superior leakage performance in the integrated circuit designs, as long as the antennas are placed far apart with respect to their operating frequencies. While the use of separate antennas for Tx and Rx is beneficial for isolation performance, it may come with disadvantages. The most notable drawback is in an integrated RADAR system that utilizes on-chip antennas. Since antenna structures tend to be larger than the overall circuitry, using two antennas instead of one will significantly increase the die area.

### 1.3.2 RADAR Types by Carrier Modulation

RADAR systems employ a diverse set of carrier modulation schemes to obtain information from targets such as velocity, distance, and angle of arrival. However, the modulation of the carrier signal is not always necessary. Continuous-wave (CW) radars send out a transmit signal at a known frequency,  $f_0$  to the target with the use of the transmit antenna. This transmitted signal is then scattered by the target object, and a part of it is picked up by the receiver. If the target object is not still, then the received signal will be shifted from the center by  $f_d$ . This phenomenon is called the doppler shift [7], and it is the fundamental mechanic behind the radar systems. In CW radars, this frequency shift is extracted with the use of a down-conversion mixer to acquire the velocity of the target object. CW radars cannot detect the distance of a target.

Detection of the distance of a target is achieved in CW radars with the modulation of the carrier signal. Frequency modulated continuous wave (FMCW) radars modulate the frequency of the transmit signal at the signal source. The frequency of the transmit signal is modulated as a linear ramp, and this allows the measurement of propagation delay to extract distance information from the received signal. Properties of FMCW radars will be explained in further detail in Chapter 2.

Pseudo-random noise (PRN) modulated radar is another CW radar variant with a different carrier modulation scheme. As the name suggests, the carrier signal in these types of radar systems is phase or frequency modulated with the use of a pseudo-random binary sequence (PRBS) [24], which is usually implemented as a linear feedback shift register. Compared to FMCW radars, PRN radars do not require a linear frequency ramp, which makes it easier to implement in integrated circuit designs [25]. The main drawback of PRN radars is the increased complexity of the required signal processing at the baseband level.

Another common type of radar is called Pulsed radar. Unlike the three variants that were described above, Pulsed radars are not continuous-wave radars. This type of radar works on the principle of sending a burst signal to the target in a short time interval. The receiver picks up the echo of this burst signal. For a known propagation speed of the electromagnetic wave sent to the target object, the distance of the target object can be calculated by measuring the propagation delay between

the received and transmitted burst signals. Similar to the CW radars, the velocity of the targets can be derived from the doppler shift on the received signal.

## 1.4 SiGe BiCMOS Technology

SiGe BiCMOS technology has been the prominent process technology in the realization of RF and mm-wave integrated circuits within the last decade. Matured from laboratory research to the mainstream market within the last two decades, continued advances within this period have enabled the production of fully integrated single-chip systems with comparable performance to their III-V counterparts at a lower cost. One of the most important advantages of SiGe BiCMOS technology over the III-V processes, such as GaAs, GaN, InP, is the ability to integrate the RF front-end with the baseband digital circuitry in a single chip. This aspect of increased integration makes SiGe processes more cost-effective compared to a III-V based process.

Scaled CMOS processes have also improved drastically over the last decade in terms of RF performance, starting to compete with SiGe BiCMOS processes within the last few years. Scaling the transistor dimensions yielded a significant increase in  $f_t/f_{\max}$  performance, and processes such as Fully Depleted Silicon on Insulator became comparable to their SiGe performance [26]. However, deep scaled CMOS processes are more prone to process variations and, have inferior passive performance due to having metal layers that are thinner, and closer to the substrate compared to that of a 130nm SiGe process. Table 1 provides a comparison between the SiGe BiCMOS process with its CMOS and III-V counterparts.

The high performance of the SiGe processes is enabled by bandgap engineering. Ge has a smaller bandgap voltage (0.66 eV) compared to that of Si (1.12 eV). The base region of the heterojunction bipolar transistors (HBT) are formed with the SiGe compound, allowing higher current gain with the increased electron injection as a result of the lower bandgap voltage. Use of smaller structures that are later vertically and laterally scaled also serves to further improve the parasitic performance of the process. In addition, the graded Ge doping improves the base transit time, further improving cut-off and maximum oscillation frequencies [27]. These improvements are critical for the RF performance of the process since the high-frequency performance

**Table 1:** Performance comparison of different semiconductor technologies for radio frequency integrated circuits (Excellent: ++; Very Good: +; Good: 0; Fair: -; Poor: --) [27]

Performance Metric	SiGe HBT	SiGe BJT	Si CMOS	III-V HBT	III-V HEMT
Frequency Response	+	0	0	++	++
1/f and Phase Noise	++	+	-	0	--
Broadband Noise	+	0	0	+	++
Linearity	+	+	+	+	++
Output Conductance	++	+	-	++	-
Transconductance	++	++	--	++	-
Power Dissipation	++	+	-	+	0
CMOS Integration	++	++	N/A	--	--
IC cost	0	0	+	-	--

of a process technology is usually measured with these two parameters. The transit or cut-off frequency,  $f_t$ , is the frequency point where the transistor's current gain ( $\beta$ ) is unity. The effects of the aforementioned improvements on parasitic performance on  $f_t$  can be seen in:

$$f_t = \frac{1}{2\pi} \left( \tau_b + \tau_c + \frac{1}{g_m} (C_\pi + C_\mu) + (r_e + r_c) C_\mu \right)^{-1} \quad (1)$$

where  $\tau_b$  and  $\tau_c$  are the transit time in base and collector regions,  $g_m$  is the transconductance,  $C_\pi$  and  $C_\mu$  are base-emitter and base-collector junction capacitances, and  $r_e$ ,  $r_c$  are the emitter and collector resistances respectively [27]. Any improvements on transit times, emitter/collector resistance, and device parasitics will directly translate into  $f_t$  improvements since it is directly dependant on these parameters.

The maximum oscillation frequency, also called  $f_{max}$ , is defined as the frequency where the power gain of the transistor becomes unity, and it is given as

$$f_{max} = \sqrt{\frac{f_T}{8\pi C_\mu r_b}} \quad (2)$$

where  $r_b$  is the base resistance. In SiGe processes,  $r_b$  can be improved without sacrificing from the current gain by adjusting the Ge doping at the base region.  $r_b$  along with  $f_t$  are also an important parameter in the determination of the minimum noise figure that can be achieved by the process. The relation between the device parameters and the minimum noise figure (NFmin) is given as

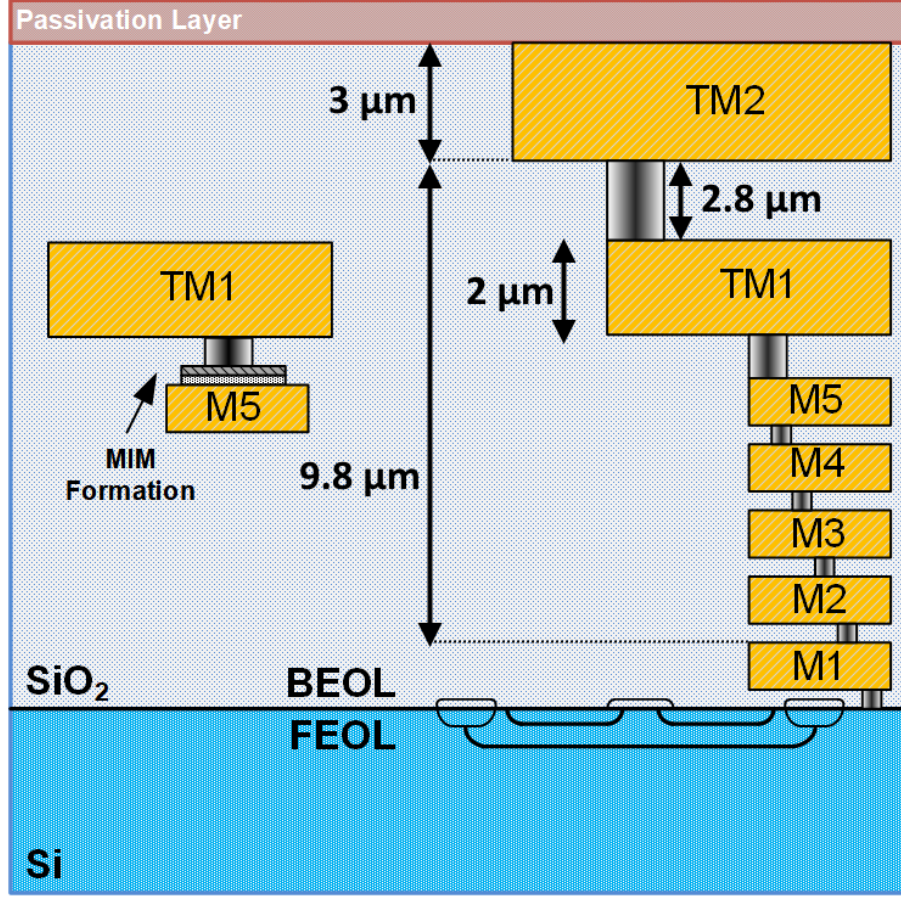


**Figure 6:** BEOL Cross-section view of IHP 0.13 $\mu\text{m}$  SiGe BiCMOS SG13G2 technology.

$$NF_{min} = 1 + \frac{n}{\beta_{DC}} + \sqrt{\frac{2J_c}{V_t} (r_e + r_b) \left( \frac{f^2}{f_t^2} + \frac{1}{\beta_{DC}} \right) + \frac{n^2}{\beta_{DC}}} \quad (3)$$

where  $J_c$  is the collector current density. Improvements on the device parasitics and intrinsic terminal resistances, in turn,  $f_t$  and on  $r_b$  without sacrificing from the current gain, will directly translate into better noise performance for the device. The benefits mentioned in this section play an important role in making the SiGe BiCMOS process a strong choice for the implementation of mm-wave remote sensing systems. The high  $f_t/f_{max}$  performance, the possibility of integration with digital baseband circuits, and the lower/comparable cost compared to III-V and deep scaled CMOS processes make SiGe BiCMOS a competitive choice for the implementation of mm-wave RADARs. For the works presented in this thesis, IHP Microelectronics 0.13  $\mu\text{m}$  SG13G2 process technology is used. The front-end-of-line features npn SiGe HBTs with  $f_t/f_{max}/BV_{CEO}$  of 300 GHz / 500 GHz / 1.6 V as well as both

salicided and unsalicided polysilicon resistors [28]. The cross-section of the process is given in Figure 6. The back-end-of-line (BEOL) includes five thin (Metal1-Metal5) and two thick (TopMetal1 - TopMetal2) aluminum metal layers. Top metallization layers are 2 and 3  $\mu\text{m}$  thick, respectively. Metal-insulator-metal (MIM) capacitors are formed between Metal5 and TopMetal1 layers with a high relative permittivity insulator layer. The majority of the transmission lines in the presented works are implemented with TopMetal2-Metal1 or TopMetal2-Metal3 configurations, which are 9.8 and 7.7  $\mu\text{m}$  apart.

## 1.5 Motivation

Millimeter-wave systems are becoming a part of everyday life with the emergence of many new applications. RADARs are no different as such systems are starting to be used for many different areas. Enabled by the advancements in silicon-based process technologies, the cost of designing circuits and systems operating at high frequencies has become lower. Nowadays, 77 GHz automotive RADARs have become standard equipment in passenger cars [29], and the detection of humans in a highly-cluttered environment is one of the many emerging applications of RADARs. High-resolution RADARs are being used as a part of multi-sensor systems for new applications such as hand gesture recognition, and RADARs provide a solution that is power-efficient and with reduced complexity compared to color and depth sensors [30]. The use of millimeter-wave bands, such as the 122 GHz industrial, scientific, and medical (ISM) band, comes with several advantages. The higher available bandwidth at these frequencies allows the use of a greater RF bandwidth, which directly translates as increased range resolution, allowing the separation of closer targets. The reduced wavelength also allows the circuit designers to build circuits with smaller die areas and, process technologies such as SiGe BiCMOS offer a great opportunity for high-performance RF and digital integration.

A 122 GHz FMCW RADAR front-end that is suitable for high-resolution remote sensing applications such as gesture recognition and vital sign detection is presented in this thesis study, designed and sent to fabrication using IHP's SG13G2 SiGe BiCMOS technology. Bi-static architecture is favored to minimize the TX-RX leakage, which could cripple the system if implemented with monostatic configuration. The

designed circuits work within a frequency range of 110-130 GHz, with the center frequency being the 122 GHz ISM band.

## **1.6 Organization**

The thesis is divided into four chapters. After the introduction, Chapter 2 focuses on a broad overview of FMCW remote sensing with the theoretical background concerning FMCW RADARs. Fundamentals of FMCW RADARs are explained in detail, including the extraction of target information such as range, velocity. Terms like range resolution, RADAR equation, RADAR cross-section are explained. Chapter 2 continues with the challenges of high-resolution sensing, with an overview of micro doppler analysis.

Chapter 3 focuses on the description and analysis of the designed system and its sub-blocks. Design steps, methodology, and the implementation of the designed circuits are explained in detail. Chapter 3 is concluded with system-level simulation results.

Chapter 4 serves as the conclusion of the presented work, and also touches on the possible future work for the system.

## 2 FMCW Remote Sensing

This chapter aims to expand upon the brief overview of FMCW RADARs from the Chapters 1.3.1 and 1.3.2. The necessary theoretical background on the working principles of FMCW RADAR is explained within this chapter. The chapter will start with an explanation of the fundamentals of FMCW radars. Then, methods for the detection of the target object's range, velocity as well as terms such as range resolution, radar cross section (RCS), and RADAR equations are explained in detail. In order to provide a better perspective on the thesis work, challenges of high-resolution sensing, and the concept of multiple output multiple input (MIMO) RADAR are explained towards the end of the chapter.

### 2.1 FMCW Fundamentals

FMCW RADAR is, as the name suggests, a variant of continuous wave radar with the frequency-modulated carrier. As explained in Chapter 1.3.2, unmodulated CW RADARs are unable to detect the range of the object. Such systems can only extract the target's velocity from the doppler shift, and if the target object is still relative to the RADAR system, it will simply fail to detect the object. In FMCW RADARs, the carrier signal is modulated as a linearly increasing frequency ramp with a period. This modulation allows the determination of the distance to the target from the propagation delay information. This modulated signal is also called the Chirp signal.

Figure 7 shows an example of a sinusoidal chirp with a periodical increase in its frequency as a function of time. The frequency ramp shown in this figure is called Sawtooth modulation, from its shape. The chirp signal is defined by a number of parameters, as denoted in Figure 7. The first of these parameters is the start frequency ( $f_C$ ), which is the starting frequency point of the ramp. The next parameter is the bandwidth,  $B$ , which sets the frequency range of the ramp. The bandwidth of the chirp determines the maximum frequency of the carrier signal ( $f_C + B$ ) and also sets the RF bandwidth requirement of the system.  $T_P$  is called the chirp period or chirp duration, which is the dedicated time for the one chirp cycle to complete its rise from  $f_C$  to  $f_C + B$ . The slope of the chirp can be calculated by dividing the

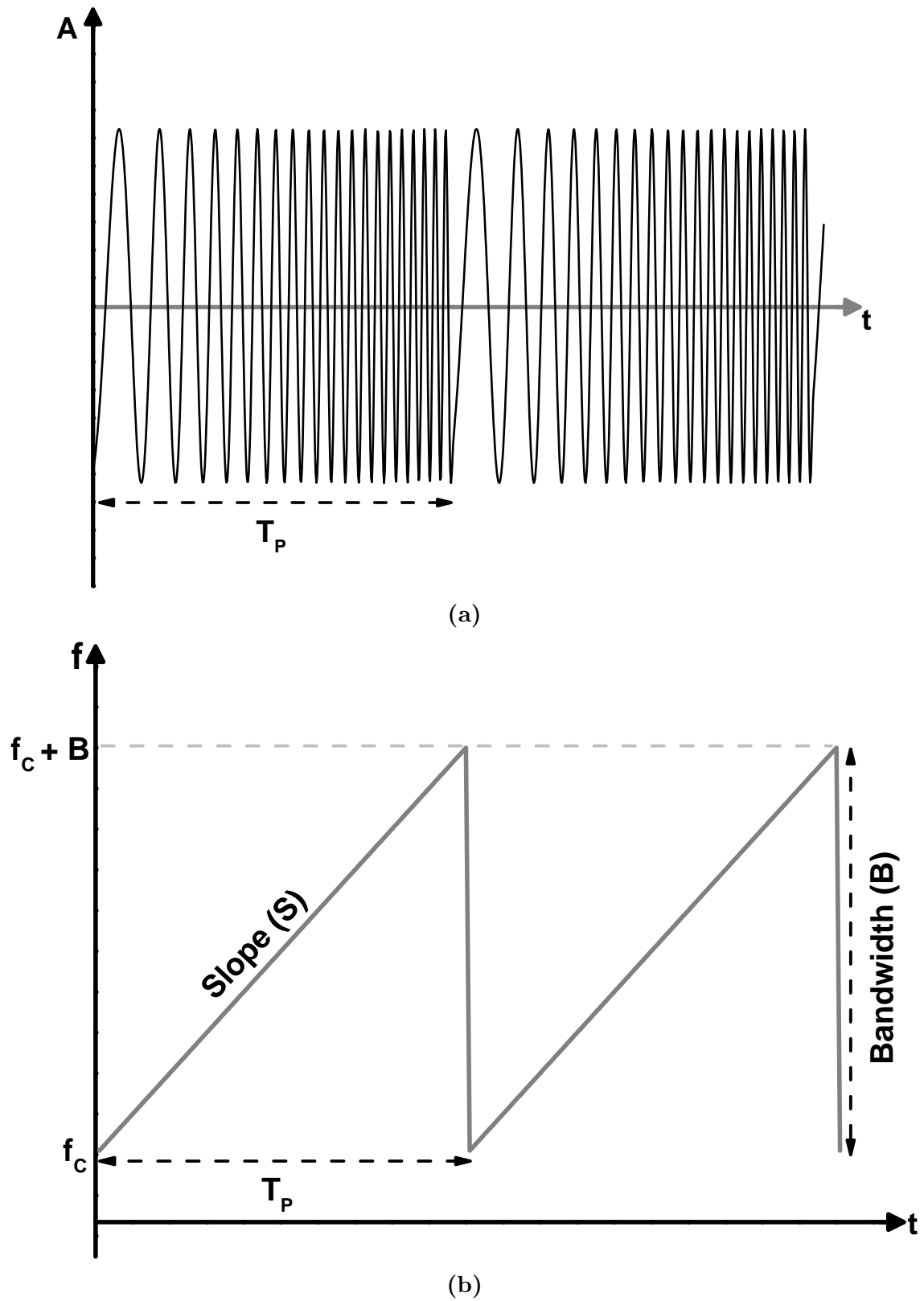


**Figure 7:** (a) A sawtooth-shaped chirp signal with amplitude as a function of time, and (b) its corresponding behavior on the frequency domain.

chirp's bandwidth,  $B$ , to its period.

Equation 4 shows the mathematical expression for a waveform consisting of an up-chirp, similar to the one shown in Figure 7. It is important to note that these equations are valid only for one period of the chirp.

$$f_t(t) = f_c + St \quad \text{where} \quad S = \frac{B}{T_P} \quad (4)$$

Translating this equation to the time domain yields a signal  $x_t$

$$\begin{aligned} x_t(t) &= A_t \cos(2\pi f_t(t)t) \\ &= A_t \cos(2\pi f_c t + 2\pi S t^2) \end{aligned} \quad (5)$$

It is important to understand the mechanisms behind the detection of an object's range and velocity with the FMCW RADARs. The fundamental working principle can be summarized as follows. First, the chirp signal is generated. A sawtooth type linear frequency ramp can be obtained with the use of a voltage-controlled oscillator (VCO). The control voltage of the VCO can be controlled with a sawtooth waveform to change the output frequency of the oscillator. The transmitted wave hits the targetted object and the reflection is collected by the receiver. The received signal is then mixed with a copy of the transmitted signal, where both signals are essentially subtracted in the frequency domain, to acquire the intermediate frequency (IF) signal. The IF signal contains information about the target object and has to be processed accordingly to extract the desired information. Figure 8 shows an example of transmitted and received signals in the frequency domain and the resulting IF signal. For any target object at a distance,  $R$ , the received signal will return after a certain time delay. If the target is motionless relative to the RADAR, a doppler shift will not be observed. In this example, both a time delay of  $\tau$  and a doppler shift  $f_d$  is observed. The delay due to the distance results in a frequency difference called the beat frequency ( $f_{beat}$ ). For an object in motion relative to the RADAR, the IF spectrum includes both the beat and doppler frequencies. The following chapters will expand upon how to extract range and velocity information from the IF spectrum.

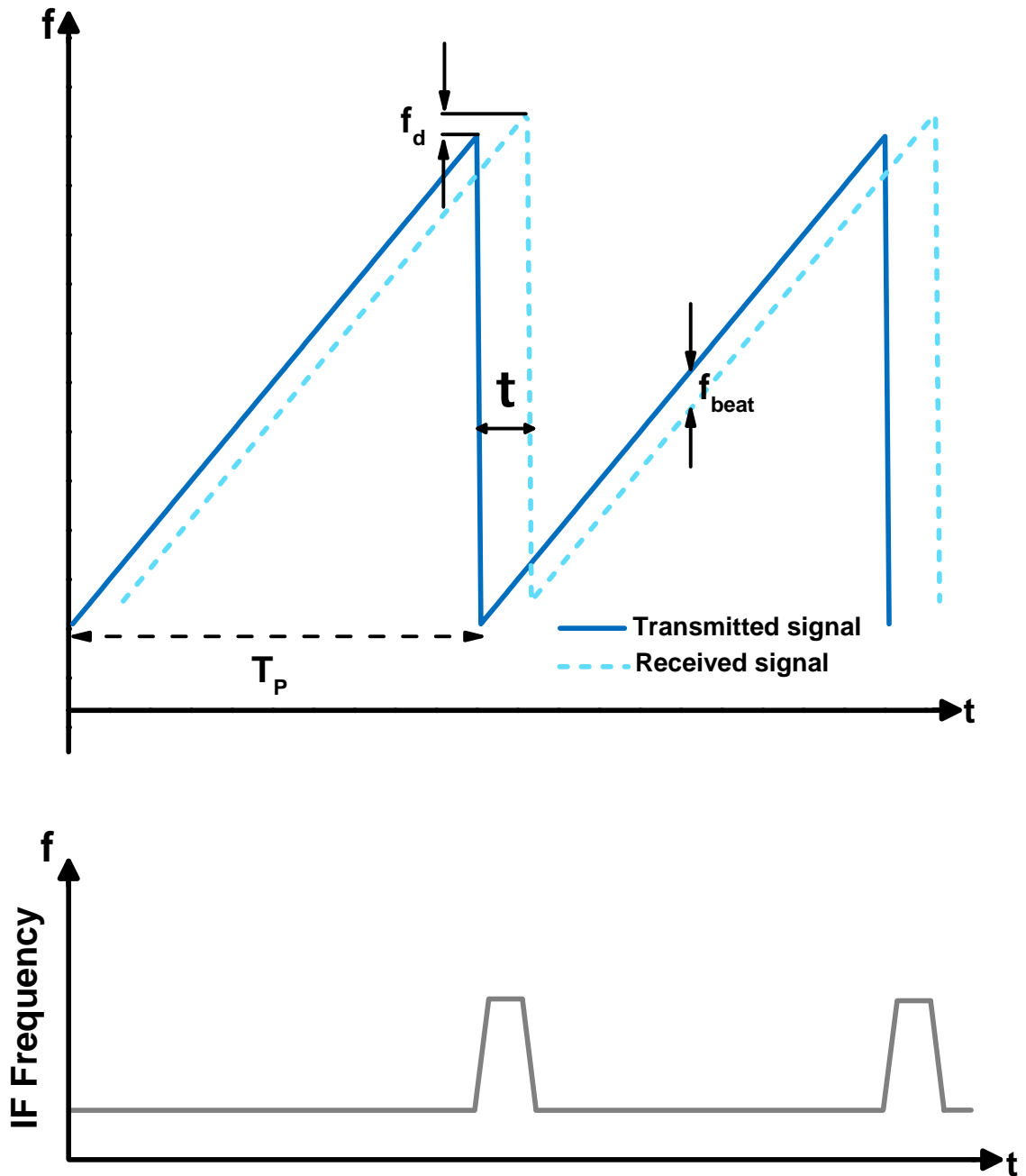


Figure 8: Transmitted and received signals and the resulting IF signal of a FMCW RADAR using sawtooth modulation.

### 2.1.1 Distance Detection

The ability to detect the distance or range of the object is the defining property of FMCW RADARs compared to the CW Doppler RADARs. This property is a result of the frequency-modulated transmitted signal, as discussed within the previous section. The received signal will return with a certain delay due to the distance between the antenna and the target object. This delay is common for all forms of modulation types, Sawtooth, triangular, etc. As previously presented in Figure 8, the time delay  $\tau$ , is a function of the object's distance to the transmit antenna and can be expressed as

$$\tau = \frac{2R}{c} \quad (6)$$

where  $R$  is the target's range, and  $c$  is the speed of light.  $\tau$  is also referred to as Round-trip time since the delay is simply the result of the transmitted electromagnetic waves traveling the distance to the target twice with the velocity of  $c$ . For simplicity, the objects that will be investigated in this section will have no relative velocity with respect to the RADAR system. Otherwise, the doppler shift created by the target's velocity is also added to the beat frequency and appears as an error on the distance measurement. Figure 9 shows two scenarios and the resulting IF tones. A single object with no relative velocity will create a constant beat frequency and this tone can be expressed as

$$f_{beat} = S \frac{2R}{c} \quad (7)$$

where  $S$  is the rate of change or the slope of the chip signal. The slope of the chirp can be written in terms of the chirp duration,  $T_P$ , and chirp bandwidth,  $B$ . To obtain an expression for the range of the target object, Equation 7 can be rearranged as follows

$$R = \frac{cT_P}{2B} f_{beat} \quad (8)$$

This equation will give the range of the single object that was detected by the RADAR. For the case of multiple targets being present, as also shown in Figure 9, multiple IF tones will be generated. These tones can be separated by taking discrete Fourier Transform (DFT) - usually a fast-Fourier transform (FFT). The resulting IF

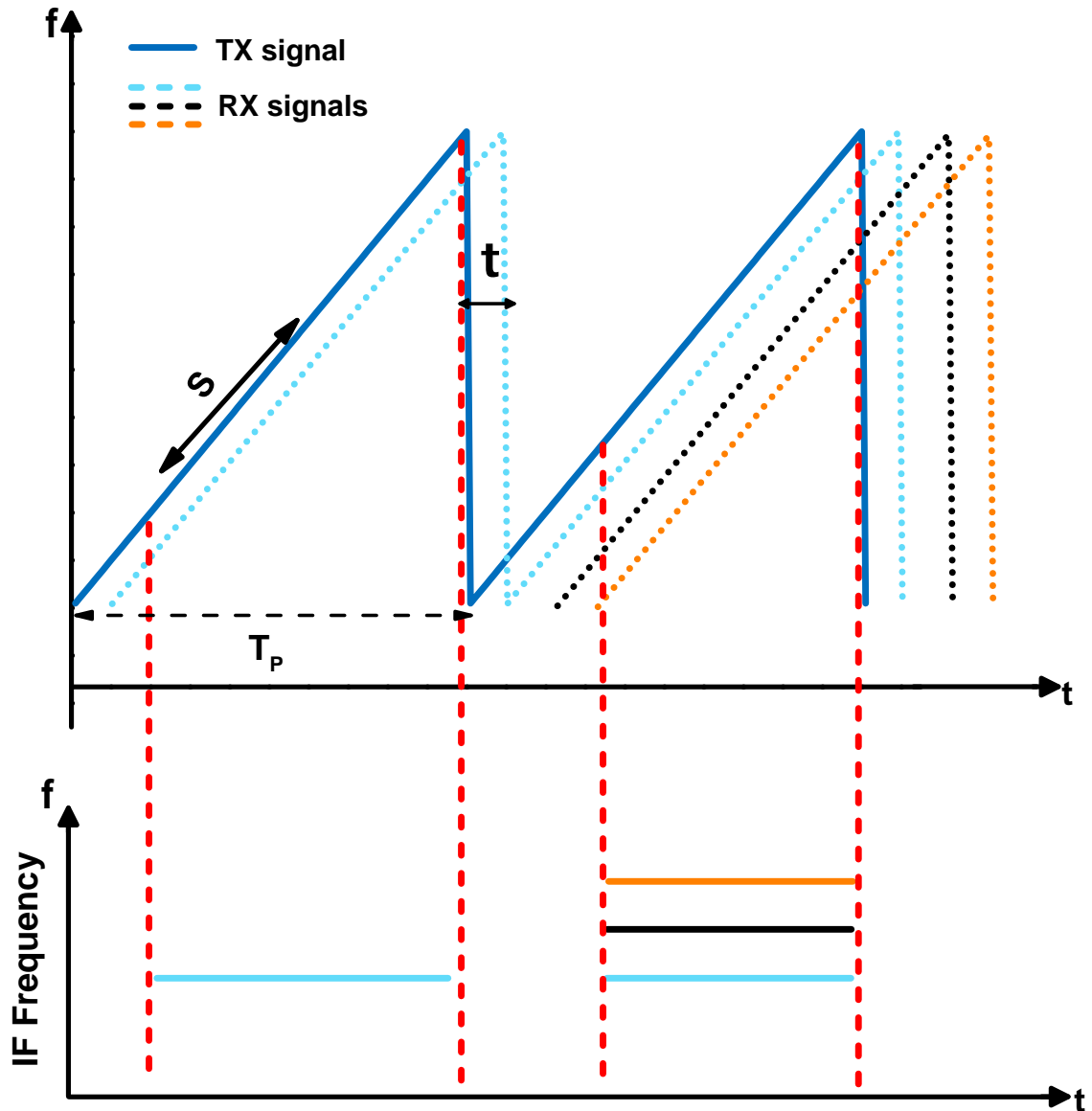


**Figure 9:** Transmitted and received signals and the resulting IF tone(s) for both single and multiple target detection.

spectrum will contain multiple peaks for each respective target objects at different ranges. For higher accuracy range measurements, the phase of the IF signal can be investigated. The IF signal's phase is more sensitive to changes compared to its frequency, which makes it possible to detect very small changes in the target's range, enabling applications such as vibration measurements and vital sign tracking [31].

### 2.1.2 Range Resolution

As explained in the previous section, the presence of multiple targets will result in multiple IF tones with varying frequencies. This scenario is where the term Range Resolution becomes important. The range resolution of an FMCW RADAR is the system's ability to separate multiple targets. This can also be explained as the minimum separation between two different targets that allows the system to differentiate them and not detect them as one single target.

According to the Fourier transform theory, the minimum resolvable frequency difference is limited by the inverse of the observation period. In other words, the minimum resolvable frequency difference can be expressed as

$$\Delta f > \frac{1}{T_P} \quad (9)$$

where  $\Delta f$  is the frequency difference between the two IF tones and  $T_P$  is the chirp period. Equation 9 shows that in order to distinguish two targets, they have to create IF tones that have a frequency difference larger than the inverse of the chirp period. Recalling Equation 7 and using in combination with Equation 9, the range resolution of an FMCW RADAR can be obtained as

$$\begin{aligned} f_{beat_1} &= \frac{S2R_1}{c} & f_{beat_2} &= \frac{S2R_2}{c} \\ \Delta f &= \frac{S2(R_2 - R_1)}{c} & \text{and taking } (R_2 - R_1) &= \Delta R \\ \Delta R &> \frac{c}{2ST_P} = \frac{c}{2B} & \text{since } B &= ST_P \end{aligned} \quad (10)$$

As shown in Equation 10, the range resolution of an FMCW RADAR is directly proportional to the modulation bandwidth. Therefore, the use of mm-wave frequencies has become favorable for high-resolution sensing applications. For example, the short-range 77 GHz automotive radar band has a bandwidth of 5 GHz, 76-81 GHz, whereas the 24 GHz automotive radar only has a bandwidth of 200 MHz. This makes the 77 GHz band more suitable for short-range radar applications. Similarly, D-band frequencies (110-170 GHz) have become attractive for high-resolution RADAR based imaging.

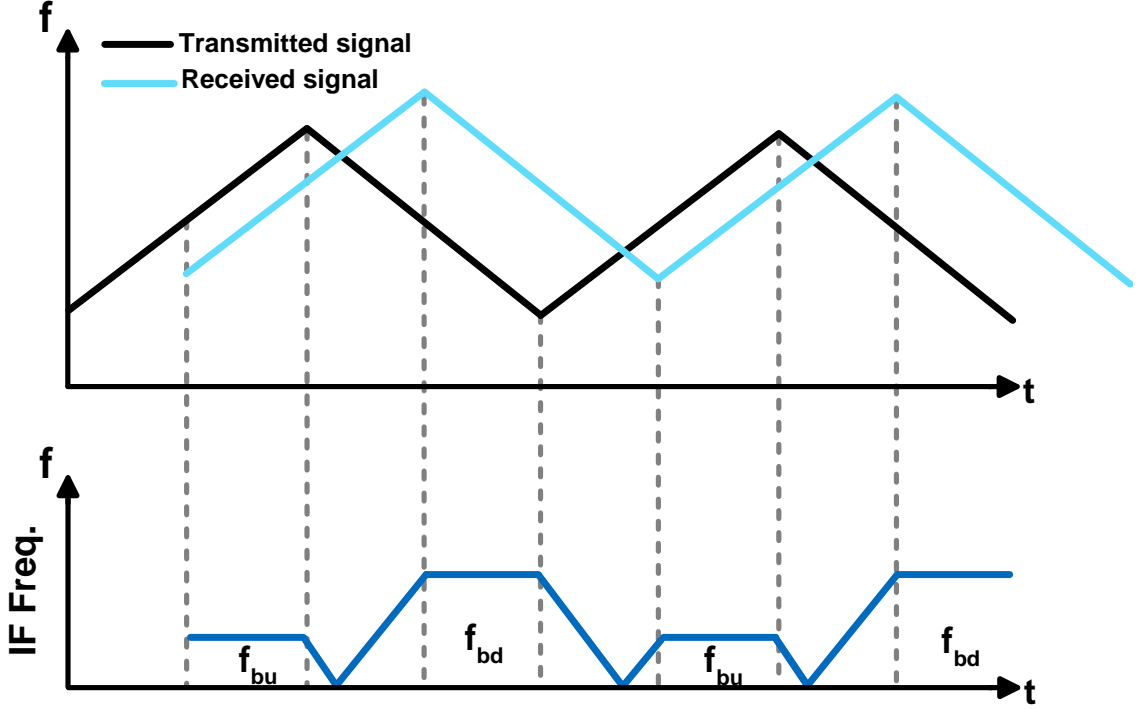


**Figure 10:** Transmitted and received signals and the resulting beat frequencies triangle modulated chirp.

### 2.1.3 Velocity Detection

The detection of velocity is rather complicated in FMCW RADARs compared to unmodulated CW RADARs. In unmodulated CW RADARs, the doppler shift observed at the IF spectrum will give the relative velocity of the target object, making the velocity detection simple. However, in FMCW RADARs that use saw-tooth modulation, the presence of both time delay and Doppler shift complicates the detection of target velocity. Recalling Figure 8, the resulting IF frequency contains both the  $f_d$  and the frequency difference due to the time delay caused by the round-trip time.

One method to measure the velocity of the target in the saw-tooth modulation scheme is to send out two chirps with a small time separation. Given that these chirps are sent out fast enough, they will both have the same IF frequencies and thus the same peaks after the first FFT. However, these peaks will have different phases, and this phase difference can be written as

$$\Delta\phi = \frac{4\pi v_r T_P}{\lambda} \quad (11)$$

where  $v$  is the relative velocity of the object,  $\lambda$  is the wavelength of the transmitted signal, and  $T_P$  is the chirp period. Equation 11 can be rewritten as follows to derive an expression for the velocity.

$$v_r = \frac{\lambda}{4\pi T_P} \quad (12)$$

In saw-tooth modulated FMCW RADARs, to extract this phase difference, usually, a second FFT is taken after the initial FFT that is taken to extract range information [32]. To extract velocity information easier, another form of frequency modulation becomes favorable. In triangle modulated FMCW RADARs, the same time delays and doppler shifts as the saw-tooth modulations are still present. However, for one section of the modulation cycle, the doppler shift adds up the beat frequency while it subtracts for the other section. This is presented in Figure 10 with two different beat frequencies appearing on the IF spectrum, up and down beat frequencies  $f_{bu}$  and  $f_{bd}$ . Unlike the saw-tooth modulation, the doppler frequency, and the relative velocity can now be extracted by

$$\begin{aligned} f_d &= \frac{2v_r}{\lambda} \\ f_d &= \frac{f_{bd} - f_{bu}}{2} \\ v_r &= \frac{\lambda}{4} f_{bd} - f_{bu} \end{aligned} \quad (13)$$

This property of the triangle modulation makes it favorable over saw-tooth modulation for the simplicity of relative velocity extraction.

#### 2.1.4 RADAR Equation

The properties and the theory discussed within Section 2.1 have been specifically for FMCW RADARs. However, to fully grasp the concepts behind the detection and extraction of target information with FMCW RADARs, some of the basic terminologies have to be analyzed. These terminologies are important as they play a vital role in the correct detection and measurement of the signals.

First of these terminologies is the well-known RADAR equation. RADAR equation is important to determine parameters such as received power, signal to noise ratio (SNR), required antenna gains for a fixed received power at a fixed range, and

more. The RADAR equation is derived from the ratio of the power density incident on the target and the power available at the receiver. For a simple bi-static radar system, the power density incident on the target at a range  $R$  to both transmit and receive antennas can be expressed as

$$S^i = \frac{P_t}{4\pi R^2} G_t \quad (14)$$

where  $P_t$  is the transmit power,  $G_t$  is the transmitter antenna gain and the term  $1/R^2$  is the spherical spreading loss factor [33]. Only a certain part of this incident power will be intercepted by the target object. The ratio of intercepted power by the object to the incident power density is a function of RADAR cross section (RCS) of the target, which will be covered in more detail in the following chapter. The intercepted power by the target can be expressed as

$$P^i = \sigma S^i \quad (15)$$

which in turn will be scattered by the object and arrive at the receiver as

$$S_s = \frac{P^i}{4\pi R^2} \quad (16)$$

similarly to Equation 14. The power that will be collected by the receiver antenna, assuming no polarization losses, can be expressed as

$$P_r = A_{er} S_s \quad \text{where} \quad A_{er} = \frac{\lambda^2}{4\pi} G_r \quad (17)$$

where  $A_{er}$  is the effective aperture area of the receiver antenna which can be rewritten in terms of gain ( $G_r$ ) as shown above. Combining Equations 14 to 17 allows us to express the received power level in the following form

$$P_r = P_t \frac{\lambda^2 G_r G_t \sigma}{(4\pi)^3 R^4} \quad (18)$$

This expression, famously called the RADAR equation, can be modified further by adding an additional term on the denominator -usually denoted as  $L$ - to represent losses such as polarization losses, internal attenuation factors on the Tx and Rx

paths, reflection losses and more.

### 2.1.5 RADAR Cross Section (RCS)

RADAR cross section (RCS) can be intuitively called a target object's ability to reflect the incoming RADAR signals in the direction of the receiver. Under the farfield conditions, RCS is defined as the ratio of uniformly scattered power density  $S^s$  of a target to the incident power density on the target,  $S^i$  [34]. Recalling these terms from Equations 14, 15, and 16, RCS of the target object can be written as a combination of Equations 15 and 16

$$\sigma = \frac{4\pi R^2 S^s}{S^i} \quad (19)$$

RCS is normalized to the power density incident on the target. This removes the dependence of RCS to the distance of the target object to the transmitter as well as the transmitted power level. RCS is defined to characterize the target objects and this notation allows it to be a measure of the target's properties rather than parameters such as transmitted power, receiver sensitivity, and, the position of the receiver [34]. RCS primarily depends on the material and the geometry of the object, as well as the wavelength of the signal sent to the object. The unit of the RCS is square meters or dBsm in dB scale, which comes as a comparison to signal reflected from a perfect sphere of cross-sectional area of  $1 \text{ m}^2$ .

## 2.2 High Resolution Sensing

High-resolution sensing is one of the emerging application areas for FMCW RADAR systems. These applications usually involve detection of targets at short to medium ranges and have high accuracy requirements. RADAR systems have become attractive for industrial sensing applications with increasing range-resolution and accuracy performances. One such work is presented in [35], where the system achieves an accuracy of  $200\mu\text{m}$  at a range of 50mm. As briefly mentioned in Chapter 1, the use of mm-wave frequencies enables the transmitted signals to penetrate through dust and fog, allowing the RADAR system to make accurate measurements in harsh conditions.

One of the main challenges for short-range, high accuracy/resolution sensing is the low reflectivity of the target objects. This property results in a low RCS for the target object. Low RCS for the target will directly result in a low received signal level, recalling the Equation 18 from Chapter 2.1.4. The use of high-frequency bands such as the 122 GHz ISM band brings the opportunity of increased bandwidth. However, the requirement to detect targets with low RCS also means that a high dynamic range for the receiver is needed, which is more challenging to achieve in high frequencies.

Other limits on the accuracy of an FMCW RADAR can be summarized as the signal-to-noise ratio (SNR), the phase noise of the transmitted signal, and the linearity of the chirp/ramp signal. Noise in a RADAR system both degrades the range resolution and maximum range. The SNR for the receiver can be written as

$$SNR = \frac{P_r}{P_n} \quad (20)$$

Typically, the overall noise in the system includes thermal noise,  $1/f$  noise from the active devices, and the phase noise of the frequency synthesizer. Modeling the noise as purely thermal gives the following expression

$$P_{nth} = \frac{kT_n B_n}{T_s B_n} \quad (21)$$

where  $k$  is the Boltzmann constant,  $T_n$  is the noise temperature,  $T_s$  is the sampling interval, and  $B_n$  is the bandwidth. The term  $T_s B_n$  in the denominator is called the processing gain, and it is a result of sampling the beat frequency at a small noise bandwidth during the sampling time [36]. Combining Equation 18 from Chapter 2.1.4 and 21, the SNR due to the thermal noise is equal to

$$SNR = \frac{\lambda^2 P_t G_r G_t \sigma T_s}{(4\pi)^3 R^4 k T_n} \quad (22)$$

Phase noise directly degrades the SNR of a RADAR system. The transmitted chirp signal's linearity is also affected by the phase noise since it adds a phase and frequency disturbance to the chirp signal, reducing the range resolution and accuracy by degrading the peak shape of the IF signal [37]. In a RADAR system where the received signal from the target is downconverted with a copy of the transmitted

signal, also called homodyne, the effects of the phase noise and ramp non-linearities are decreased due to the phase noise sources being correlated [38].

### 2.2.1 Micro Doppler Effects

In high-accuracy detection applications such as hand gesture recognition, vital sign, and vibration detection, subtle motions of the target object play an important role. As previously discussed, the relative motion of the target object to the RADAR system causes a frequency shift, and it is defined as the Doppler effect. Originally introduced in 2006 for coherent laser-based RADAR systems, the concept of micro-motion and micro-Doppler is a relatively new set of terms for microwave RADARs [39]. The tiny motions of a target object such as vibrations, and rotations are classified as micromotions. These micromotions impose frequency modulation onto the RADAR's echo signal [41]. Examples of such motions are fixed-wing airplane propellers, helicopter rotors, and even human movements. In fact, the detection of human behavior and vital signs have been one of the major areas that utilize micro-doppler effects [42, 43]. The extraction of micro-Doppler effects has increased complexity in signal processing compared to conventional velocity and range measurement, usually requiring very fast FFTs and the use of advanced algorithms such as neural networks. An example of micro-Doppler signature of a person in motion is shown in Figure 11.

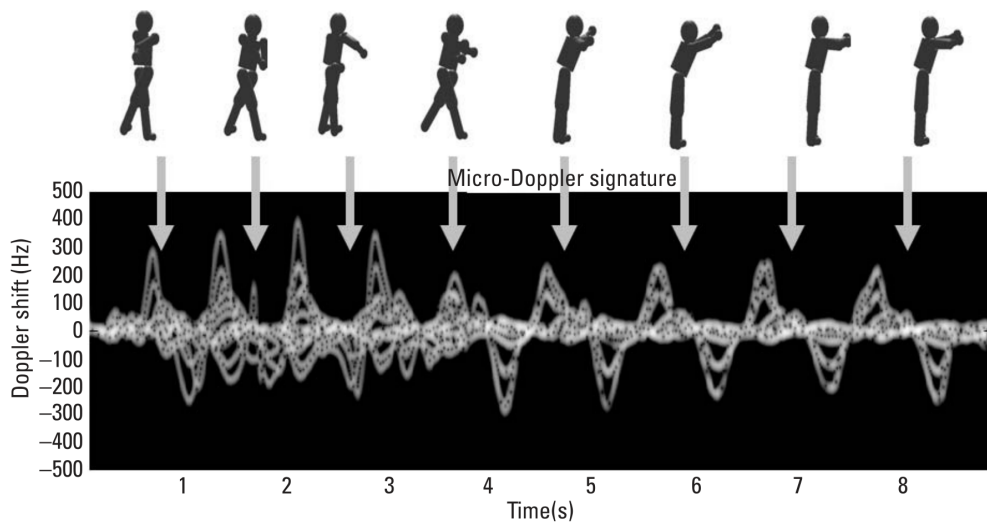


**Figure 11:** The micro-doppler signature of a person for different movements. [40]

## **3 122 GHz High Resolution FMCW Radar Front-End**

This section provides information regarding the properties, specifications, and results of the designed system. The general working principle of the designed system is provided in Section 3.1, giving insight into possible target scenarios and the theoretical calculations for the determination of the performance specifications. The following sections explain the design steps, methodologies, and the simulation results for each respective sub-block of the system. A comparison to the state-of-the-art for the key sub-blocks are included within their respective sections. Section 3.8 presents the system-level simulation results, discussion on the overall performance, as well as a comparison to the prior art.

### **3.1 Detailed Overview of the Designed System**

#### **3.1.1 System Architecture, Specifications and Design Considerations**

The complete block diagram of the designed system is given in Figure 12. It consists of a low-noise amplifier (LNA), a power amplifier (PA), a mixer, a LO buffer amplifier, a single-ended to differential power splitter, and an x16 active frequency multiplier (AFM). Differential architecture is used except for the output of the frequency multiplier. Integrated on-chip Marchand baluns are included at the Tx and Rx ports for measurement purposes. The RADAR system uses bistatic architecture, with separate ports (and antennas) for Tx and Rx ports for maximum Tx-to-Rx isolation. The full system along with the breakouts of sub-blocks are sent for fabrication.

The general working principle of the system can be summarized as follows. The off-chip VCO-PLL chain generates the chirp signal necessary for FMCW operation. This signal will be connected to the chip with the use of wire bonds, which will show no major degradation on the signal at the 6-8 GHz range. The chirp signal coming from the VCO-PLL chain is fed into the AFM, where the frequency of it is multiplied by 16 to bring it up to 122 GHz. Since the AFM uses the push-push configuration, the output is single-ended. To preserve the differential architecture, this signal is fed into a single-ended to differential power splitter. This block both serves as a

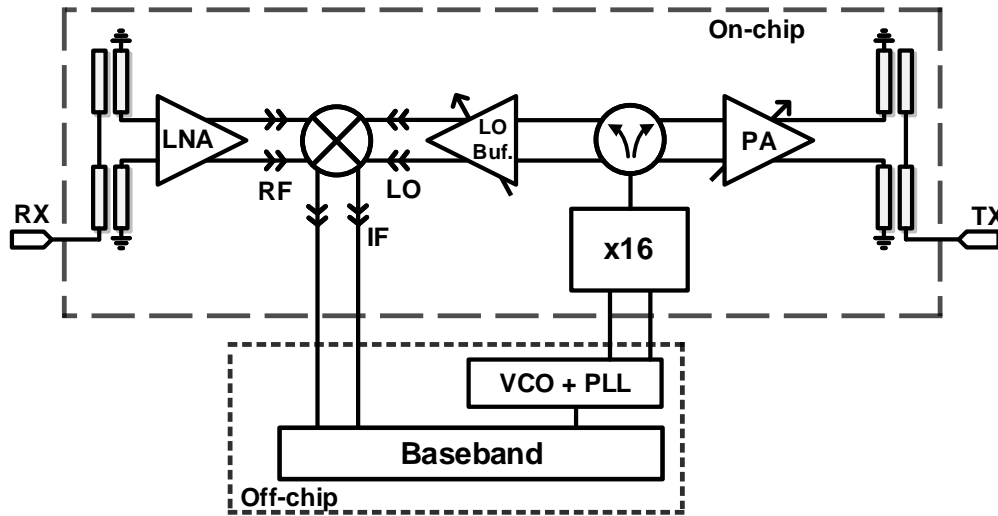


**Figure 12:** The block diagram of the designed system

balanced-unbalanced (Balun) and a power divider, which will be explained in detail later. The chirp signal flows into the PA following this block, while a copy of it is split to the LO buffer to be mixed with the received signal. The PA amplifies the chirp signal to be transmitted, which flows to the Tx output of the system, to be fed to the Tx antenna.

The Rx antenna collects the scattered signal from the object. The received signal is then amplified by the LNA. The amplified signal from the LNA is fed to the Mixer's RF port differentially, to be downconverted by the copy of the transmitted chirp. The copy of the transmitted signal, amplified by the LO buffer to a desirable level is mixed with the received signal. The resulting IF signal is taken out of the chip to be processed by the baseband circuitry. Since the IF signal is usually of low-frequency, baluns and DC-blocking capacitors will be included as off-chip components. As previously discussed in Chapter 2, FFT is utilized to extract the target information from the IF spectrum. Since this requires both the digitization and processing of the signal, it can be performed with the use of an FPGA.

As previously discussed throughout Chapter 2, there are a few important requirements for a RADAR system for high resolution/accuracy sensing applications. The first of such demands is the high RF bandwidth. All of the designed sub-blocks operate in an RF bandwidth between 110-130 GHz. While the ISM band centered within 122.5 GHz has an allocated bandwidth of only 1 GHz, there have been several

works that utilize a higher bandwidth centered at 120 GHz, showing a potential for future band allocations [44, 45]. The maximum theoretical range resolution achievable by using the 122 GHz ISM band can be calculated using Equation 10 from Chapter 2.1.2 as 15 cm. While this is a relatively high range resolution, it wouldn't be enough for the high-resolution requirements of applications such as hand gesture recognition. By utilizing the full bandwidth of 110-130 GHz, the system can achieve up to <1 cm theoretical maximum resolution. As mentioned in Chapter 2.2, the phase noise of the frequency synthesizer has the potential to degrade the range resolution of the system. An x16 active frequency multiplier (AFM) is utilized instead of a fundamental, integrated VCO. This means the off-chip VCO works at a frequency range of 6.875 GHz - 8.125 GHz, assuming the full bandwidth is utilized. This comes with several advantages, one of which is the relaxation of the tuning range of the VCO, enabling high modulation bandwidths after the multiplication. In terms of phase noise performance, frequency multiplication is comparable, if not better than building an integrated fundamental VCO with a frequency divider for off-chip PLL. Frequency multiplication adds a phase noise on top of the generated signal, and it is expressed as  $20\log(M)$  where M is the multiplication factor. Assuming the frequency multiplier circuit has no additional contribution to the phase noise, a multiplication factor of 16 introduces an additional 24 dB phase noise to the signal generated by the off-chip VCO. Since a VCO operating at 8 GHz can achieve much better phase noise performance compared to a 120 GHz VCO, the 24 dB phase noise addition is tolerable for the system.

Another major problem for RADAR systems is the Tx-Rx leakage, which is also called the self-interference. This phenomenon is especially prevalent in mono-static RADAR systems where the Tx and Rx paths share the same antenna. Since in CW and FMCW RADARs, transmitted and received signals are very close in frequency, recalling from Chapter 2, the resulting IF signal is usually in the range of 0-50 MHz range [46]. As previously discussed within Chapter 2, high-resolution short-range detection with RADAR have even lower frequency tones at the IF spectrum. Most immediate of problems due to the Tx-Rx leakage can be summarized as compression of the LNA and the mixer. A more prominent problem can be described as follows: The leaking Tx signal is downconverted with a copy of itself at the mixer, and since

these signals are at the same frequency, they generate a constant signal at the IF output of the mixer. The resulting signal is called DC-offset [47], and it degrades the SNR of the receiver, limits the dynamic range of the ADC that digitizes the signal for FFT. Especially in short-range applications, a large peak at DC after the FFT limits the system's ability to distinguish targets close-by with low beat frequencies. Considering the aforementioned challenges, bistatic architecture is preferred for the designed RADAR system to maximize Tx-Rx isolation, with the Tx and Rx ports being placed on opposite ends of the chip. Essentially, for the single-chip bistatic transceiver, the Tx-Rx isolation is limited by the coupling from the Tx port to the Rx port. Moreover, the Tx-Rx isolation can be further improved in bistatic RADAR systems by using different polarisations for Tx and Rx antennas.

Lastly, the differential architecture is utilized for the system for several advantages. In high frequency designs, the parasitics on the grounds present a major problem. Balanced designs have the opportunity to utilize virtual grounds, have higher gain, and improved stability. In addition, the differential architecture introduces common-mode noise immunity, and increases the distortion free dynamic range of the system.

### 3.1.2 Theoretical Calculations of Possible Target Scenarios

The detection of short-range, low-RCS targets with a high-resolution comes with a set of challenges, as discussed within previous Chapters. Consequently, the designed system and its sub-blocks should be able to satisfy certain performance parameters to enable the aimed applications. The first possible application area is the hand gesture recognition, for human-machine interfaces, such as dashboard control in passenger cars [16]. The first requirement for precise detection is the range-resolution, which is directly related to the chirp bandwidth. To get a sub-cm resolution performance, high modulation bandwidth is required. The designed system aims a bandwidth of 20 GHz, between 110-130 GHz. As previously discussed, one of the major challenges in RADAR detection is the SNR. This is especially prevalent in scenarios where the target object has very-low RCSs, resulting in lower received signal levels. Typically, for a detection probability of %99 with a false-alarm ratio of  $10^{-10}$ , around 16 dB SNR is required [7]. However, an SNR down to 10 dB is still

acceptable.

A study to determine the RCS of the human hand is presented in [48], where the worst-case RCS between 60-90 GHz is measured as -45 dBsm. Using this RCS value in conjunction with Equation 18 from Chapter 2.1.4, the received power for 122 GHz carrier can be calculated for a sample scenario of human hand detection at a range of 30 cm. Setting the antenna gains as 6 dBi, reported in [49] for an on-chip folded dipole implementation,  $P_{Tx}$  as 5 dBm including the transition losses to the antenna, the received power is calculated as -92.2 dBm. With the received power calculated, the SNR can also be calculated. However, of the noise floor and SNR is not straightforward, since the B in the well known  $kTB$  is not the full modulation bandwidth. In fact, the bandwidth to be used for the noise floor and SNR calculation is limited by the FFT sampling interval, as it was shown in Equation 22. Using a sampling interval of 1ms, and 15 dB NF, the noise floor and SNR are found as -114 dBm and 22 dB respectively. As made evident, even in this optimistic scenario, the calculated SNR is nearly at the required 16 dB level. Lastly, the detection of shorter-range targets means that the generated beat frequencies are closer to the DC level. Therefore, the 1/f noise of the mixer needs to be considered, as well as the DC offset created by the Tx-Rx leakage. Table 2 summarizes the minimum required system performance specifications.

**Table 2:** Summary of the required system performance parameters for reliable short-range, high-precision detection.

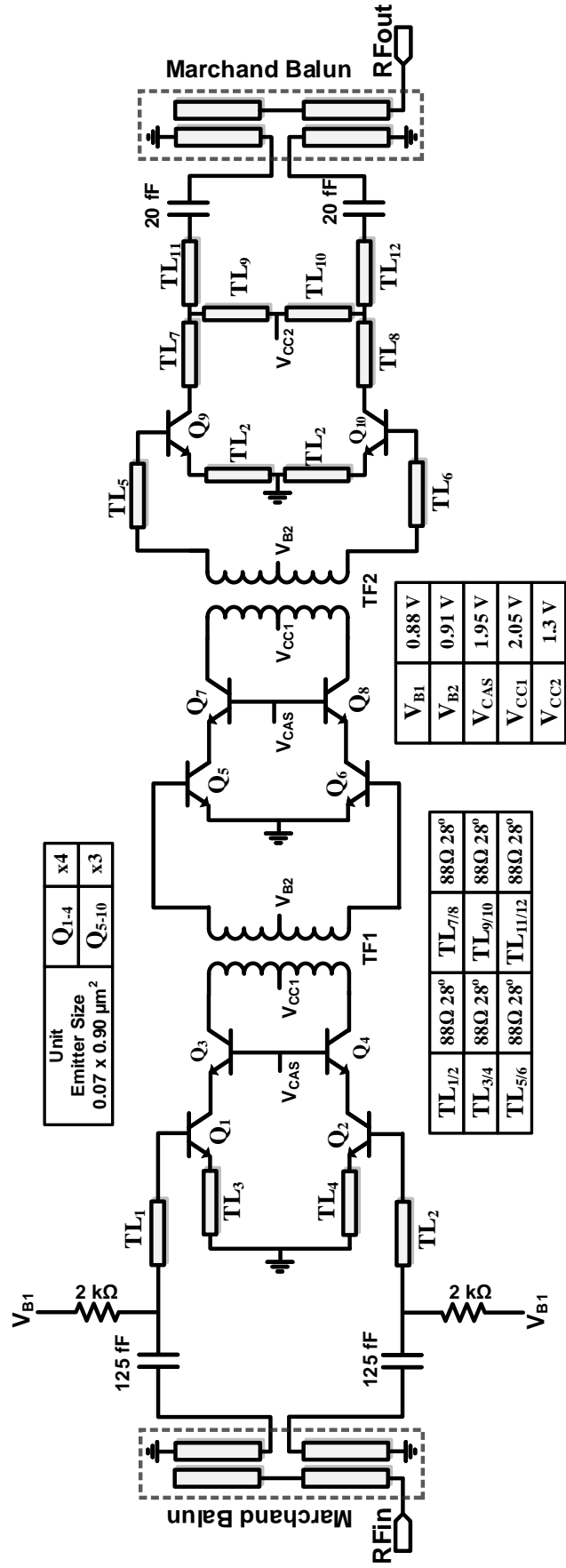
<b>Parameter</b>	<b>Value</b>
Center Freq. (GHz)	122
Bandwidth (GHz)	20
Max. Range (m)	$\sim 1$
Max. Range Res. (cm)	$< 1$
$P_{Tx}$ (dBm)	$> 5$
RX NF (dB)	$< 15$
SNR (dB)	$> 10$

## 3.2 Low-Noise Amplifier

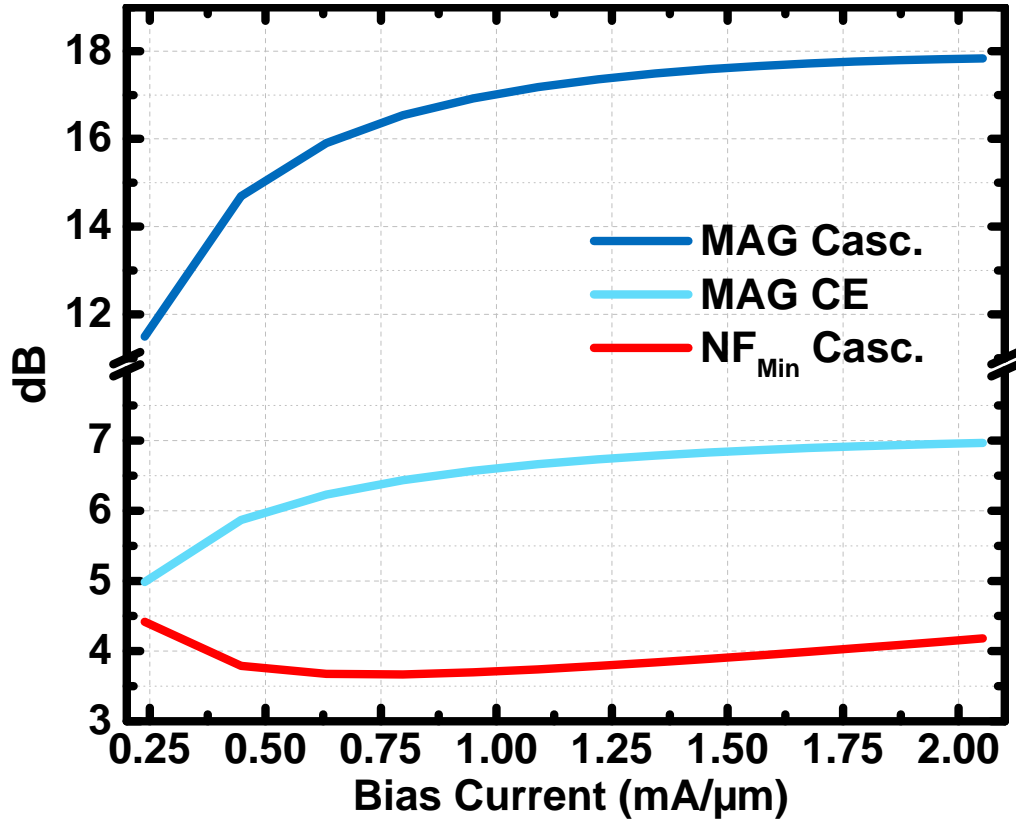
### 3.2.1 Circuit Design and Implementation

The low-noise amplifier is the first and most important block for the receiver chain, regardless of the application. As discussed within the previous chapters, the SNR of the receiver directly limits several performance parameters of a RADAR system. In applications where the target object's RCS is low, the received signal of the RADAR will be weak regardless of the target's range. Therefore, the amplification of the received signal is required. Moreover, to keep the receiver's SNR at a reasonable value, the NF of the receiver needs to be as low as possible. The receiver chain consists of the LNA and the downconversion mixer before the IF signal is taken off-chip. From the well-known Frii's Equation, given that the LNA has high enough gain, it will suppress the more noisy mixer and determine the receiver NF.

The schematic of the designed LNA is shown in Figure 13. The designed LNA utilizes three stages, with the first two stages implemented as pseudo-differential cascode, and the last stage as differential common-emitter (CE). On-chip Marchand baluns are included on both the input and the output for LNA's breakout for measurement purposes. Traditionally, CE configuration has several advantages over cascode. CE topology presents a better noise figure performance, primarily due to the low number of transistors, compared to the cascode topology. The inherent low-isolation of the CE topology causes the input and output matching circuitry to influence each other, allowing impedance matching over a high-bandwidth with the co-design of the two. Finally, CE has a lower DC power consumption at the same bias point due to the lower supply voltage requirement. Despite these advantages, CE topology falls short on high-frequencies compared to cascode. The main reason behind this is the low maximum available gain (MAG) of the CE compared to the cascode. Due to the low MAG of CE at the range of 120 GHz, for a cascaded two-stage design, the first stage will fail to suppress the noise of the following stage, which is highly undesirable. To get a high gain and low NF performance from the multi-stage design cascode topology is selected for the first two stages. For the final stage, where noise suppression would no longer be required after the first two stages, CE topology is selected. This is done to exploit the aforementioned advantage of the CE to match the output of the LNA over the bandwidth of 110-130 GHz.



**Figure 13:** The schematic of the designed LNA. (Electrical lengths of the transmission lines are given for 122 GHz, R-C sections used for biasing not shown.)



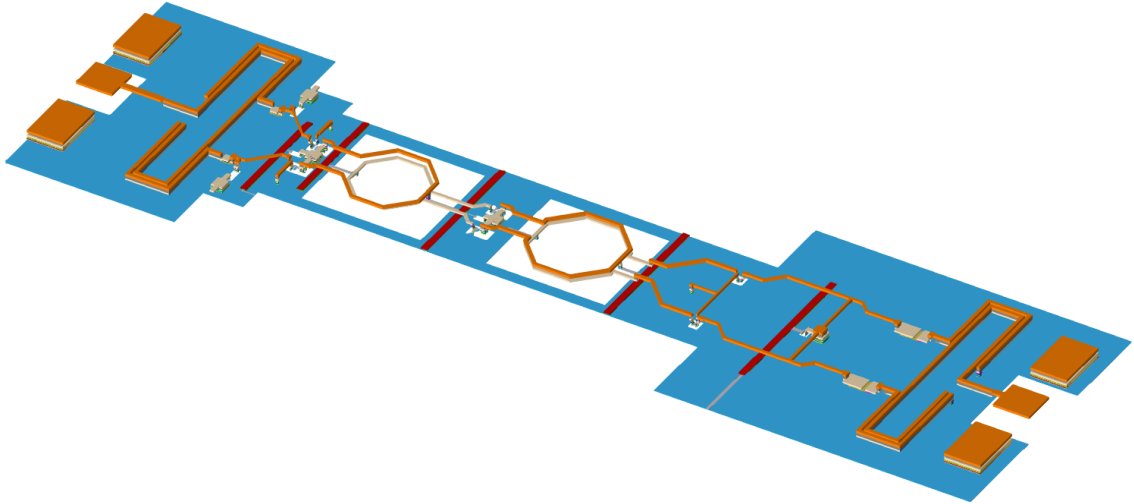
**Figure 14:** Simulated MAG and NFmin of the designed LNA for different values of collector current density.

Figure 14 shows the MAG for both inductively degenerated CE and cascode topologies and the NFmin for the cascode for different collector current densities at 122 GHz. The transistor used for Figure 14 is sized as x4 unit transistor (0.9  $\mu\text{m}$  x 4 emitter length), the bias voltage of the common-base transistor is set to 1.95 V while  $V_{CC}$  for cascode and CE is set as 2.1 V and 1.3 V respectively. The disparity between the MAG of CE and cascode is shown in this figure, where the cascode achieves around 17 dB MAG while CE is around 6.5 dB. From this graph, we can see that to get a reasonable gain performance and to suppress the proceeding stages' NF, the use of cascode topology is necessary.

The first stage, implemented as pseudo-differential cascode, is optimized for minimum NF with a slight trade-off on the gain, biased at a collector current of 0.9 mA/ $\mu\text{m}$ . The transistor's (Q1 and Q2) size is chosen as x4 to facilitate simultaneous noise and power matching. Emitter degeneration, implemented as a microstrip transmission line with TM2-M1 configuration (TL3/4), is used to bring the real part of the input impedance to 50  $\Omega$ . The rest of the input matching

is performed with the use of a series transmission line (TL1/2), a 125 fF metal-insulator-metal (MIM) capacitor, which also acts as a DC blocking capacitor, and the Marchand balun. The base bias of the first stage is connected over a large resistor of  $2\text{ k}\Omega$ . 2 pF bypass capacitors are placed after the resistors to improve low-frequency stability. Interstage matching between the first and second stages is realized with the use of a transformer. The primary winding of the transformer is implemented in the TM2 layer while the secondary is implemented in the TM1 layer. The transformer has a close to 1:1 turn ratio with a primary inductance of 270 pH, and a slightly higher secondary inductance. The primary and secondary winding are slightly misaligned to intentionally decrease the coupling factor ( $k$ ), for an increase in bandwidth [50]. The collector supply voltage is set to 2.1 V, and it is given from the center tap of the transformer. To feed the bias voltage to the center tap of the transformer, the M2 layer is used with an M3 ground shield above to isolate the DC from RF influences.

The second stage is optimized to provide higher gain compared to the first stage, also implemented as pseudo-differential cascode. Recalling Figure 14, the MAG peaks after a certain bias point, as increasing it further will increase DC power consumption and linearity. Considering this, the base bias of the second stage is increased to bring the current density to  $1.5\text{ mA}/\mu\text{m}$ , and the number of transistors is set to x3 to increase current per transistor. The matching for the second stage is fully realized with the use of secondary winding of the preceding stage transformer and the primary winding of another transformer (TF2). The transformer for the second stage has a higher primary inductance of X pH, once again with a turn ratio of 1:1. The gain peaks for the first and second stages are adjusted by the transformers as well, to help provide a flatter gain response. Both base bias and collector supply voltage are fed from the center taps of the respective transformers, saving chip area. The third stage is implemented in fully-differential CE configuration, to exploit the wider matching bandwidth property as mentioned at the start of this section. Consequently, the gain contributed by the third stage is relatively low. T-type matching with transmission lines is utilized at the collector of the CE stage to achieve required wideband matching performance. The 20 fF capacitor at the output is implemented as a metal-oxide-metal (MOM) capacitance with TM1-M5 layers, due



**Figure 15:** 3D Layout view of the LNA.

to its small value. Marchand balun is placed at the output of the circuit for the LNA breakout for measurement purposes while it is omitted in the actual system implementation. The supply voltage of the CE stage is set to 1.3 V, which is well below the  $BV_{CEO}$  for the technology. The base bias is fed from the middle part of the transmission lines TL9/10, where it would be virtual ground.

To prevent low-frequency stability problems, all bias lines utilize R-C sections with increasingly large bypass capacitors with a resistor in between to prevent unwanted frequency response. For the base connection of the common base transistor of cascode stages, a 350 fF bypass capacitor is placed at the center of the differential connection. While that point would already be virtual ground for the frequency range of interest, given that the balun functions correctly, the added bypass capacitor will provide some grounding for signals that are out of the band of interest.

The 3D layout view for the designed LNA is given in Figure 15. All EM simulations are carried out in ADS Momentum. All transmission lines used in the design are implemented in TM2-M1 microstrip line configuration, with M3 crossing underside along the biasing lines. Aside from the 20 fF capacitor at the output, all capacitors are implemented as MIM capacitors provided by the design kit. The M1 ground layer is kept connected under the whole circuit, except the transformers to preserve Q-factor, to avoid modeling inaccuracies in mm-wave frequencies. Input/output RF pads are custom designed to minimize their parasitic capacitance contribution and are included in the EM simulations of the circuit.

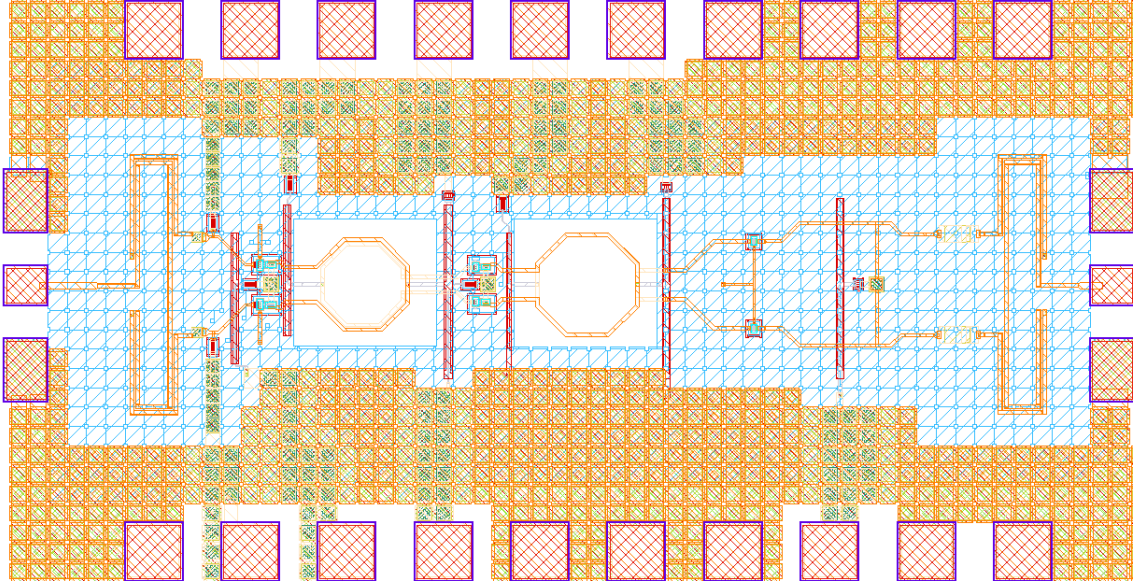


**Figure 16:** Layout of the LNA breakout.

### 3.2.2 Simulation Results

The full layout of the designed LNA is shown in Figure 16. The total chip area is  $0.66 \text{ mm}^2$  (1.1 mm x 0.6 mm), and the effective area excluding the pads and baluns is  $0.24 \text{ mm}^2$ . All pads are kept with  $100 \mu\text{m}$  pitch size while the RF pads are kept with  $75 \mu\text{m}$  to be measured with Infinity GSG-75 WR 6.5 waveguide probes. Grounded metal fillers are kept sufficiently far to minimize undesired interaction between the fillers and transformers/MSLs. Bypass capacitors are absorbed into filler cells to save area. The total quiescent DC power consumption is 39 mW, from the 2.1 and 1.3 V supplies.

The Figures 17 to 20 present the simulation results of the designed LNA. The LNA has a peak gain of 28 dB at 117 GHz with a 3dB BW between 100-128 GHz, including the 2 dB average IL for both the input and output baluns. Subtracting twice the IL of the balun, the peak gain of the LNA is found as 33.4 dB at 119 GHz. The peak shift is due to the negative slope response of Balun's IL. The input and output return losses remain greater than 10 dB between 100-130 GHz range. Similar to the gain, the IL of the input balun is directly added to the NF of the LNA, thus the IL of the balun is subtracted from the overall NF of the LNA. The simulated NF of the LNA is lower than 6 dB within the band of interest, with a minimum of 4.9 dB at 110 GHz. The simulated input-referred compression point is -26 dBm. Table 3 gives a comparison of the designed LNA to the state-of-the-art.

**Table 3:** Performance comparison of the designed LNA with previously reported LNAs implemented using silicon processes.

	Tech.	Center Freq (GHz)	Peak Gain (dB)	3-dB BW (GHz)	NF (dB)	PDC (mW)	Area (mm <sup>2</sup> )	FOM
[51]	28nm CMOS	118	21.7	28	8.4	19	0.26	9.62
[44]	55nm SiGe	125	22.6	20 <sup>+</sup>	9.2 <sup>*</sup>	16	N/A	7.25
[52]	0.13 $\mu$ m SiGe	125	27.5	17	6.5	12	0.39	19.7
[53]	0.13 $\mu$ m SiGe	147	33	42	4.8	28	0.6 <sup>#</sup>	30.4
<b>This<sup>±</sup></b>	0.13 $\mu$ m SiGe	120	33.4	28	4.9	39	0.24 <sup>#</sup>	23.7

<sup>±</sup> Simulation and Balun de-embedded \* Simulation # Area without pads

<sup>+</sup> Inferred from the graph FOM =  $20\log\left(\frac{Gain[abs]\times BW[GHz]}{P_{DC}[mW]\times(F-1)}\right)$

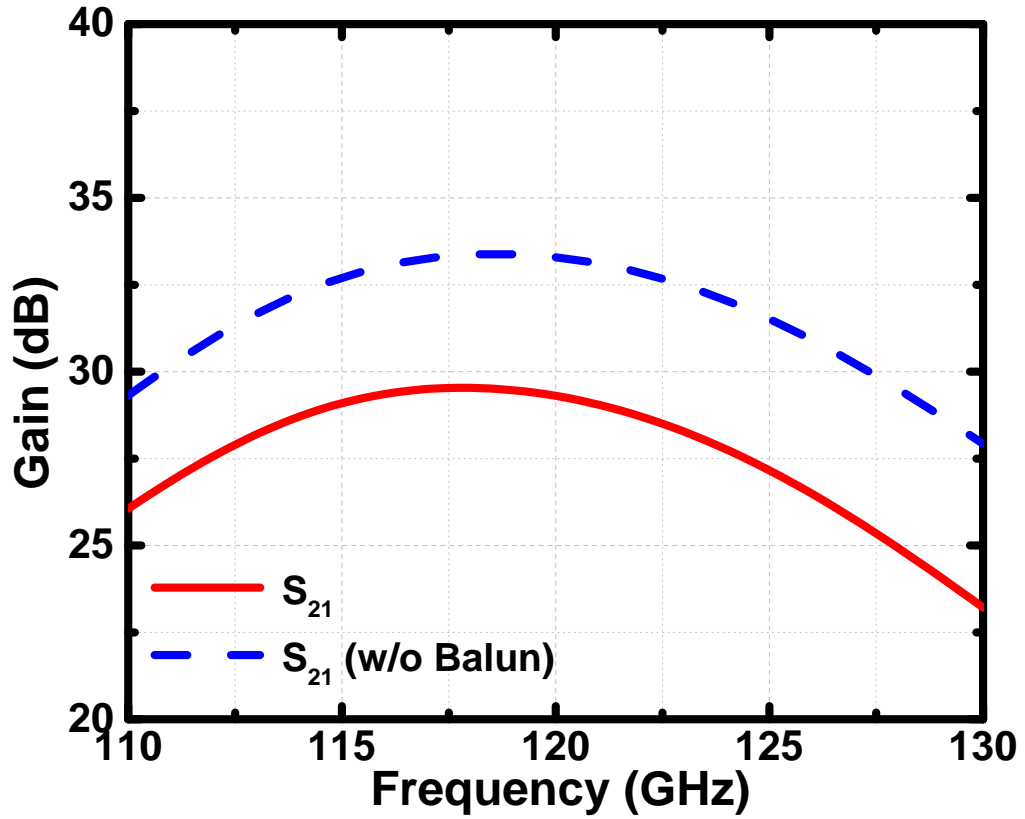


**Figure 17:** Simulated gain of the designed LNA.

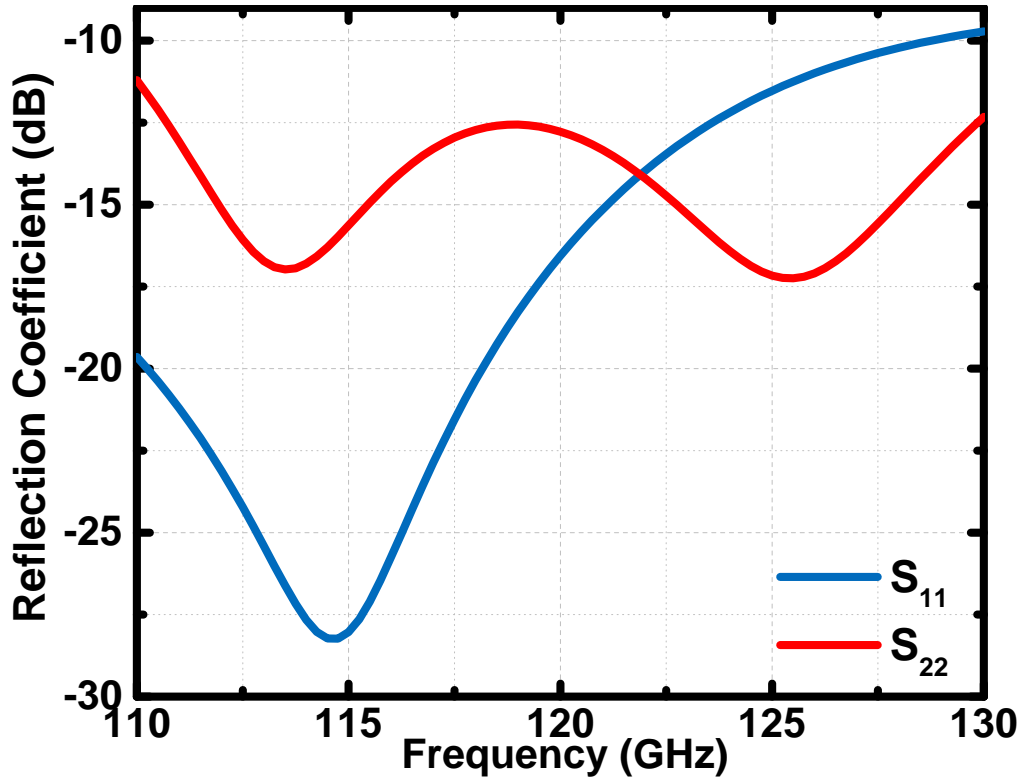


Figure 18: Simulated input and output reflection coefficients of the LNA.

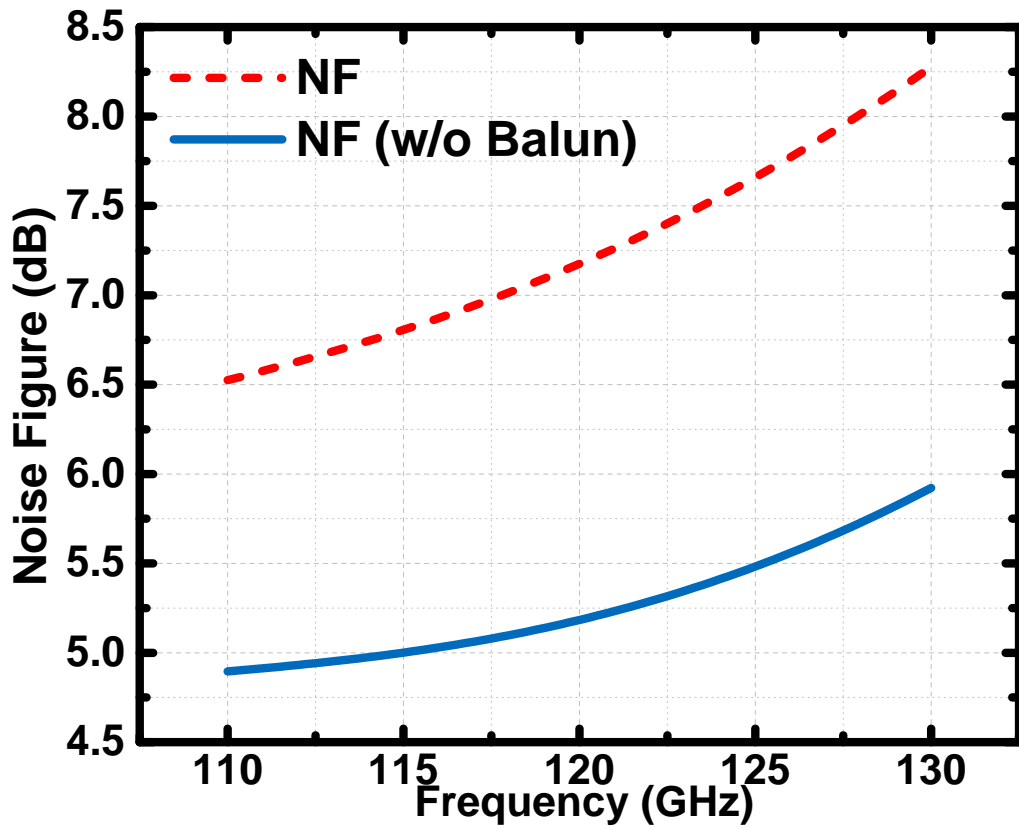


Figure 19: Simulated noise figure (NF) and minimum NF of the LNA.

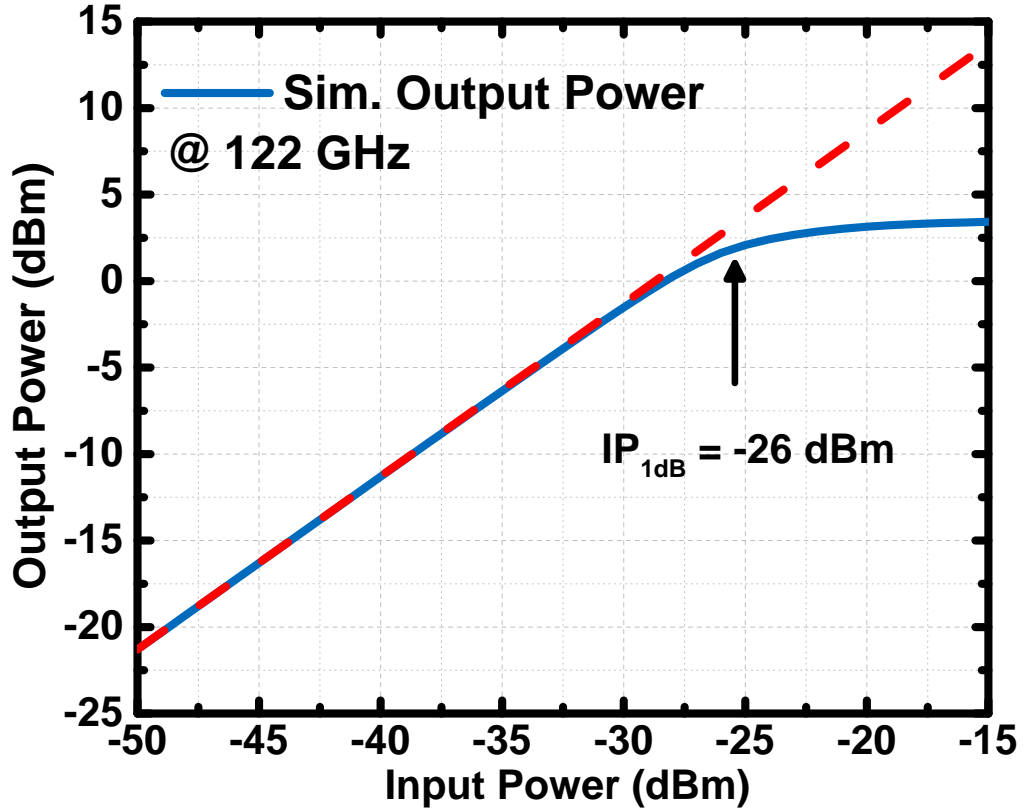


Figure 20: Simulated input referred 1 dB compression point of the LNA at 122 GHz.

### 3.3 Down-Conversion Mixer

#### 3.3.1 Circuit Design and Implementation

The mixer is a key block for almost all receiver architectures as they are required for frequency translation. Similarly, in FMCW RADAR systems, downconversion into IF-domain is required to capture the range and velocity information of the target. Mixers can be categorized as active or passive in terms of operation; and unbalanced, single- balanced or double-balanced in terms of topology. Active mixers are usually made of two main stages, the transconductance stage, where the signal is amplified, and the mixing stage where the RF and LO signals are multiplied to obtain the IF signal. Both passive and active mixers utilize a switching stage where the mixing is performed, driven by a LO signal of varying amplitude. Active mixers show several advantages over passive mixers, the first of which is the ability to provide conversion gain (CG). Another advantage of the active mixers is the lower required LO drive level since the base terminal (if implemented using HBT) of the transistor is biased at a certain DC level. However, passive mixers

usually exhibit superior linearity performance.

Single or double-balanced configurations are commonly used for the implementation of active mixers as they provide port-to-port isolations. Single-balanced mixers use a balanced LO signal with an unbalanced RF. While single-balanced mixers show 3dB higher CG for a fixed bias current compared to double-balanced mixers, they suffer from LO feedthrough. This feedthrough is a result of the unbalanced RF signal, which contains a DC component. The LO feedthrough mechanism in single-balanced mixers is shown for an input signal of  $V_{RF}\cos(\omega_{RF}t)$  [54]

$$\begin{aligned}
I_{OUT} &= (I_Q + V_{RF}G_M\cos(\omega_{RF}t))\times\left(\frac{2}{\pi}\cos(\omega_{LO}t) - \frac{2}{3\pi}\cos(3\omega_{LO}t) + \dots\right) \\
&= \frac{2}{\pi}I_Q\cos(\omega_{LO}t) + \frac{1}{\pi}G_MV_{RF}\cos((\omega_{LO} - \omega_{RF})t) \\
&\quad + \frac{1}{\pi}G_MV_{RF}\cos((\omega_{LO} + \omega_{RF})t) + \dots
\end{aligned} \tag{23}$$

In double-balanced mixers, both RF and LO signals are balanced, thus eliminating the LO feedthrough shown in Equation 23. For RADAR systems, LO-to-RF isolation is also critical. This leakage would mean the transmitted signal leaking into the received signal port, and as previously discussed within Chapter 2, this will cause the same performance degradations as the Tx-Rx leakage. Considering the superior isolation performance, the topology for the mixer is selected as the double-balanced gilbert cell. Moreover, since the designed system already uses differential architecture, the use of double-balanced topology eliminates the need for additional baluns at RF and LO ports of the mixer.

The schematic of the designed mixer is given in Figure 21. On-chip Marchand baluns are included in the mixer breakout for measurement purposes while they are omitted at system implementation. Since SNR is critical for short-range detection applications, the noise performance of the mixer is important. The RF stage (Q1/2) is biased with a lower current density for a low NF performance, and the optimum transistor size is found as x4 the unit size. The linearity of a gilbert-cell based active mixer is limited by the linearity of the RF stage. Inductive emitter degeneration is used on the RF stage to increase linearity with a trade-off on the gain, and the bias current can be increased to increase the linearity further at the cost of higher DC power consumption. The RF stage is biased to have a collector voltage of 1.55 V, slightly lower than the breakdown of the technology. Another important design

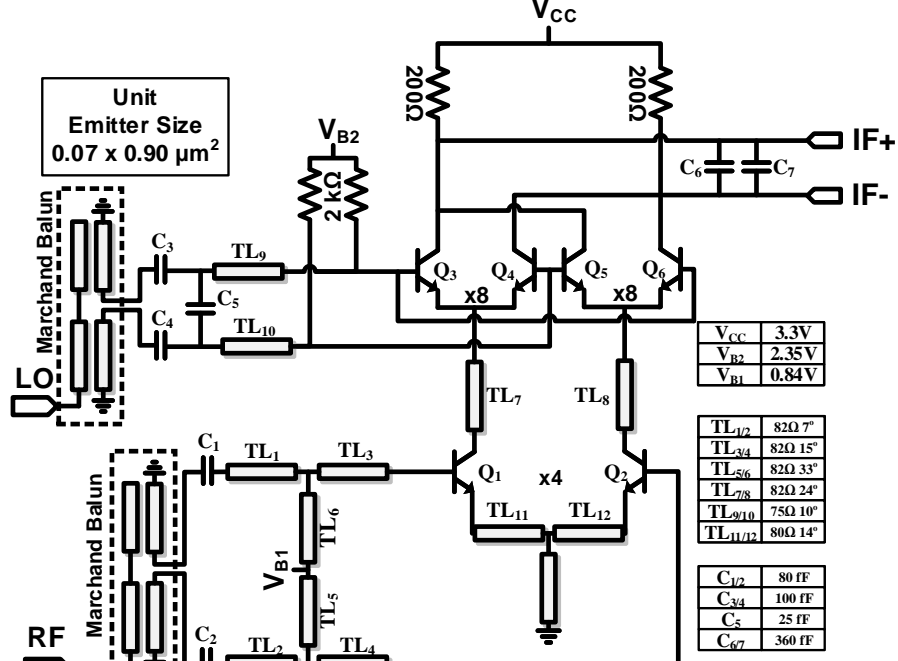
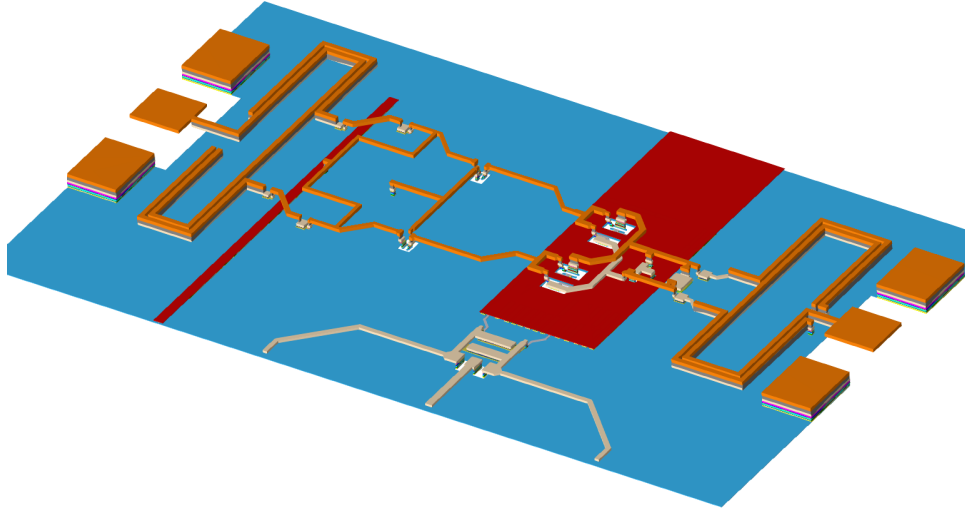


Figure 21: Schematic of the designed Mixer. (Electrical lengths are given for 122 GHz.)

aspect for short-range RADARs is the  $1/f$  noise corner of the mixer. Since targets at low ranges will generate very low beat frequencies, it is important to keep  $1/f$  noise corner as low as possible. Switching transistor size is selected as x8 to lower their noise contribution [54]. The switching transistors (Q3-Q6) are biased to have a  $V_{BE}$  closer to class-B point to ensure proper switching operation. The transmission lines (TL7/8) are used between the RF and switching stages for an increase in conversion gain by reducing the impedance mismatch between them [55]. The tail resistor is replaced by a transmission line to increase voltage headroom. IF outputs of the mixer are taken outside the chip differentially as implementing a balun on-chip, which would work in the kHz range is not feasible. Between the two differential IF output lines, two of 360 fF MIM capacitors are used to improve the RF and LO leakage to the IF port. The load is implemented as a 200  $\Omega$  resistor, which negatively affects the linearity of the mixer. However, while it would potentially provide better linearity, the use of inductors is not feasible at the IF frequency range of interest.

Figure 22 shows the 3D view of the designed mixer. The Marchand baluns used on the RF and LO ports for the breakout version of the Mixer use the same structure as the baluns used in LNA, with the LO balun having been slightly adjusted to fit the geometry. All transmission lines are realized using TM2-M1 configuration, and



**Figure 22:** 3D Layout view of the designed mixer.

similar to the LNA, a Metal-1 ground plane is included under the whole chip. The switching stage includes a Metal-3 ground shield to isolate the IF output, taken from Metal-2, between the two ground planes. All EM simulations are performed in ADS Momentum.

### 3.3.2 Simulation Results

The full layout of the designed Mixer is shown in Figure 23. The mixer occupies a total area of  $0.39 \text{ mm}^2$  ( $0.73 \text{ mm} \times 0.54 \text{ mm}$ ), including pads and baluns. The effective chip area of the mixer, excluding pads and baluns, is  $0.11 \text{ mm}^2$ . The mixer uses the same custom-designed RF pads as in the LNA with a  $75 \text{ }\mu\text{m}$  pitch size. The total DC power consumption of the mixer is 11 mW from the 3.3 V supply. The LO drive of the mixer is selected as -3 dBm to relax the LO distribution requirements within the system. IF output is taken outside the chip differentially, to be connected to an off-chip baseband buffer amplifier to bring up the IF signal to a reasonable level. DC blocking capacitors are omitted in IF since it wouldn't be possible to DC-block without disturbing the response of IF signals at very low frequencies, even with large off-chip capacitors. To avoid  $1/f$  noise degradation caused by large ac-coupling capacitors, a DC-coupled output buffer is preferable after the IF is taken outside the chip. Figures 24 to 28 presents the simulation results for the designed mixer. All simulations use an IF frequency of 20 kHz, and

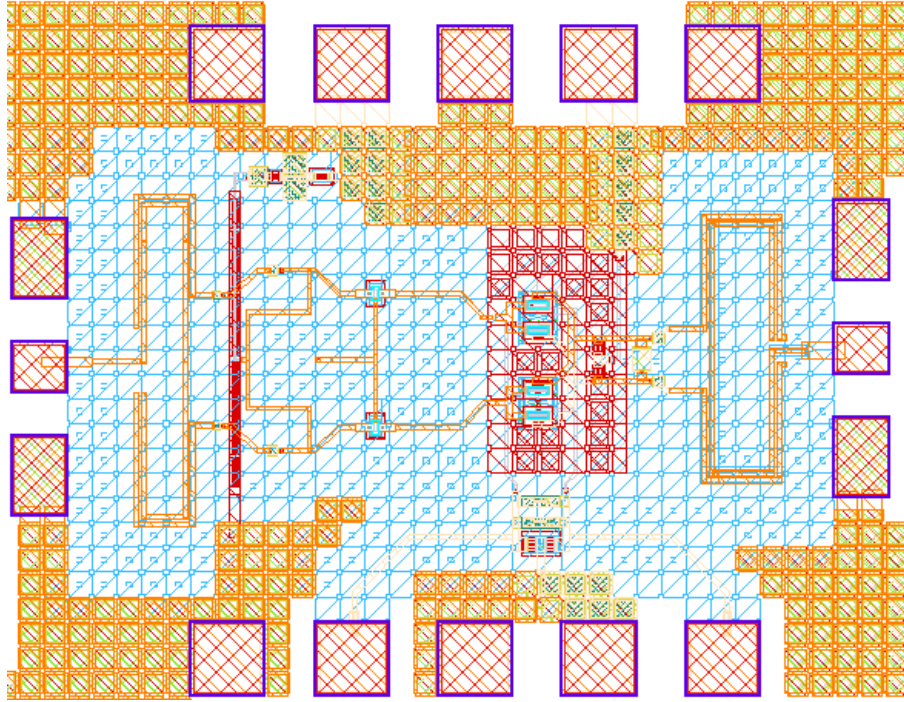


**Figure 23:** Layout of the Mixer breakout.

lowerside LO unless stated otherwise within the respective caption of the figure. The designed mixer achieves a peak CG of 1.24 dB at 110 GHz, including the RF balun, with the 3-dB BW covering the frequency range of interest. The CG and port matchings of the mixer cannot be determined from the S-parameters since the switching stage operates under large-signal conditions. To obtain the correct port matchings, Harmonic Balance simulation is performed, exciting both RF and LO ports at the same time. LO and RF ports well-matched across the 110-130 GHz band, both return losses remaining greater than 10 dB. The port-to-port isolations remain greater than 40 dB between 110-130 GHz, with LO and RF feedthrough suppressed even further with the inclusion of C6/7. Since the image band does not contain a desired signal in RADAR systems, the single-sideband (SSB) noise figure is simulated. SSB NF includes the noise from the image band folding onto the IF frequency, making it 3 dB higher than the double-sideband (DSB) NF, which is generally used in zero-IF mixers. The mixer has an SSB NF lower than 10.75 dB, with a minimum of 9.78 dB at 110 GHz for an IF frequency of 20 kHz. Another important parameter of the mixer performance for short-range detection is the  $1/f$  noise corner. Figure 28 shows the SSB NF of the mixer, for a varying IF frequency between 50 Hz to 45 kHz while the LO is fixed to 122 GHz, to model the received

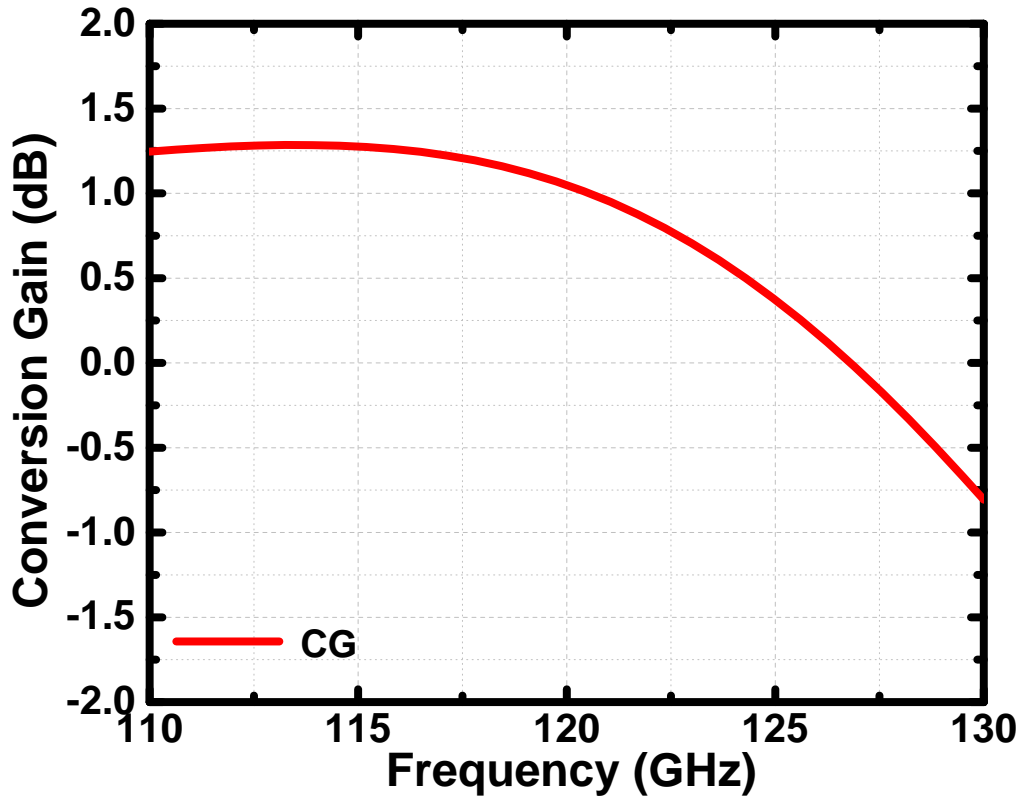


**Figure 24:** Simulated CG of the mixer at a fixed IF of 20 kHz.

signal from an object at very close range. The effect of  $1/f$  noise is seen in low-IF frequencies where the SSB NF starts high and rolls-off after a frequency range. The simulated  $1/f$  noise corner of the mixer is found as 800 Hz. The simulated input-referred 1-dB compression point of the mixer is -5dBm, and it can be improved by increasing the bias voltage of the RF stage at a cost of increased DC power consumption.

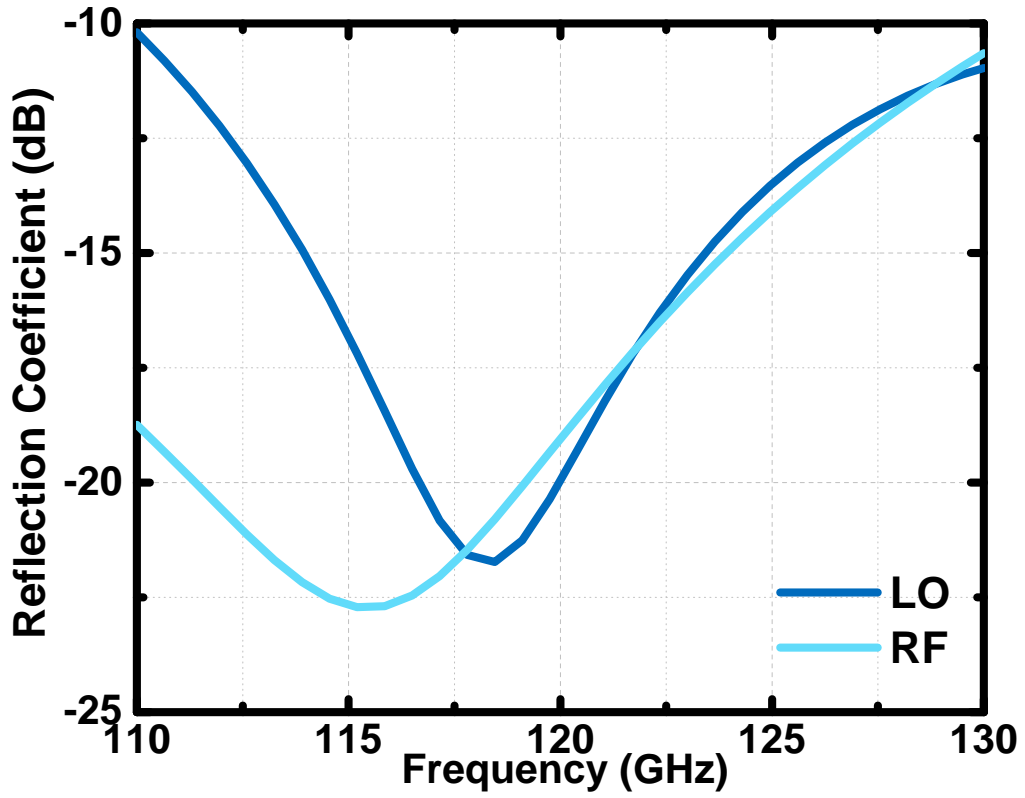


Figure 25: Simulated port matchings of the mixer at a fixed IF of 20 kHz.

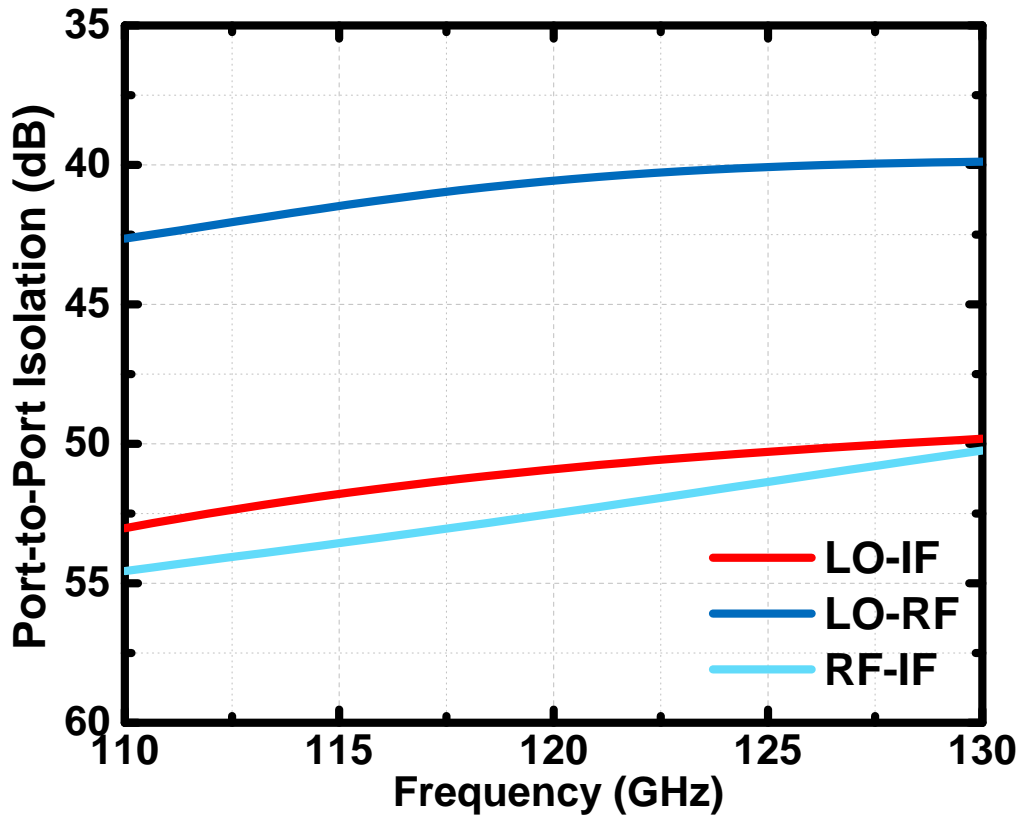


Figure 26: Simulated port-to-port isolations of the mixer.

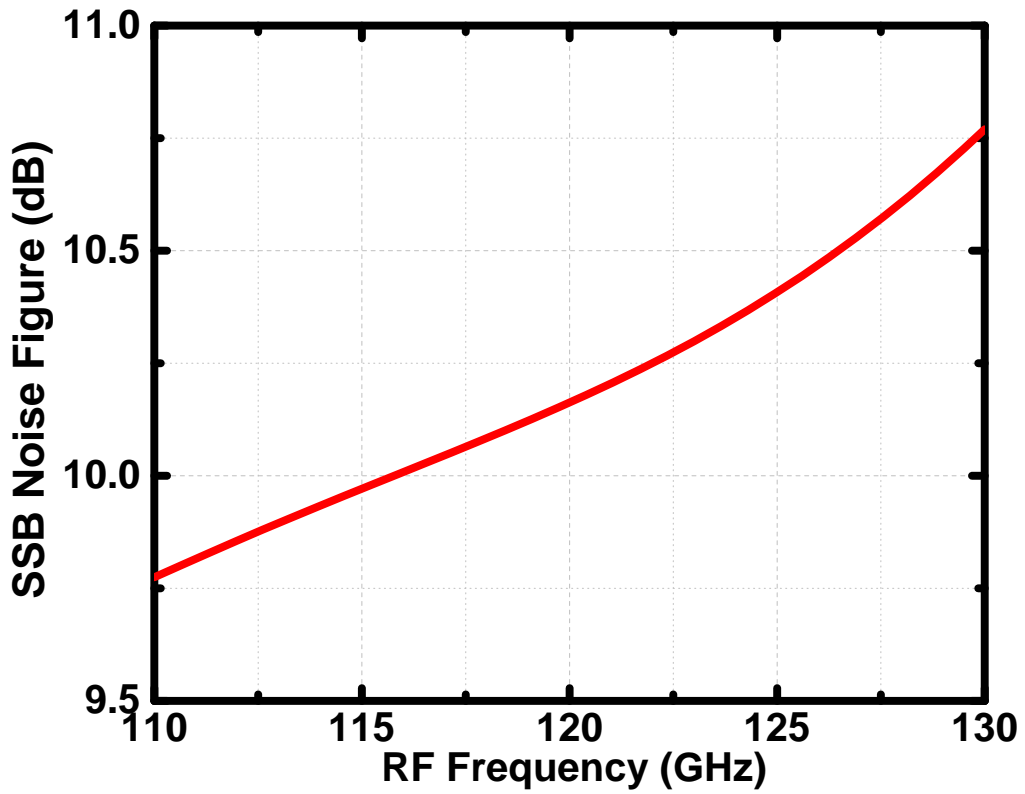


Figure 27: Simulated NF of the designed mixer versus RF frequency.

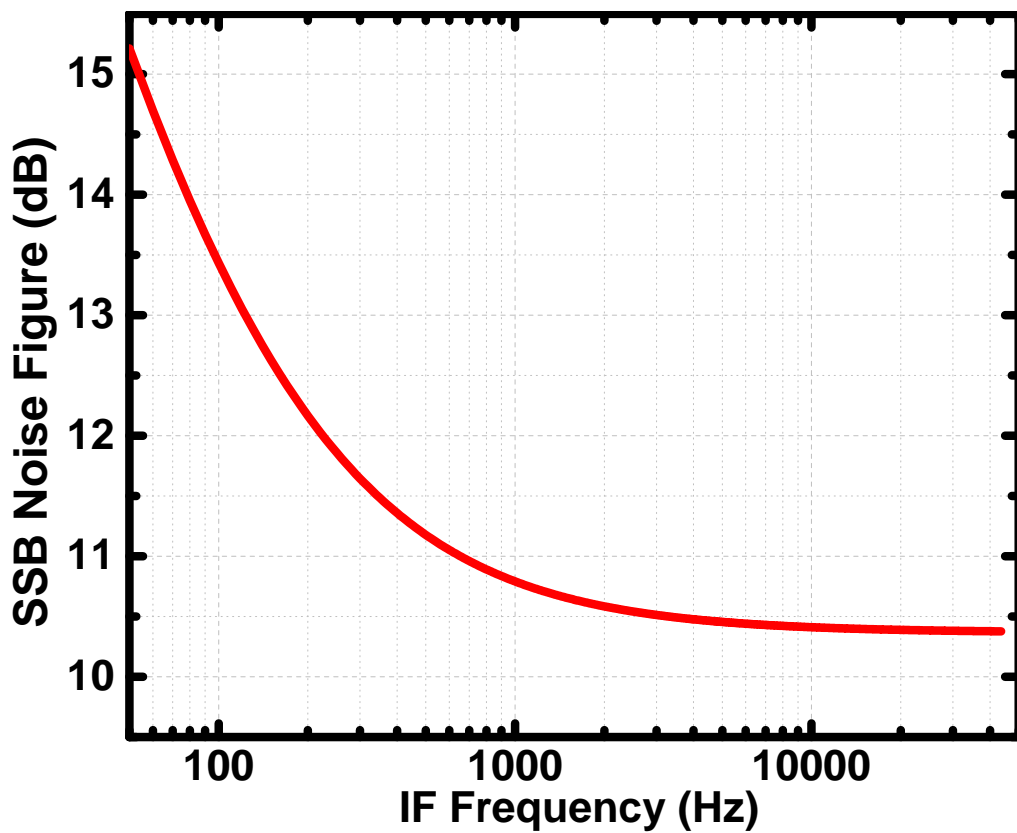


Figure 28: Simulated NF of the mixer versus IF frequency ranging from 50 Hz to 45 kHz in logarithmic scale.

## 3.4 Power Amplifier

### 3.4.1 Circuit Design and Implementation

The power amplifier (PA) plays a vital role in the overall performance of the system since it is the final block in the transmit path. The chirp signal generated by the off-chip VCO-PLL chain will be multiplied up to 122 GHz range in the frequency multiplier, and finally, be amplified at the PA. Several key parameters indicate the performance of a PA. These parameters are gain, output-referred 1 dB compression point (OP1dB), saturated output power ( $P_{sat}$ ), and the power added efficiency (PAE). In RADAR systems, the PA drives the Tx antenna to transmit the signal in the direction of the target object, and this transmitted power is called equivalent isotropically radiated power (EIRP). As previously discussed within Chapter 2, the received power for the RADAR is directly related to the transmitted signal's power. The transmitted power from the PA/antenna combination determines the maximum range of a RADAR system for a fixed Rx NF, considering that a certain level of SNR is required. Having high transmitted power is also important in the detection of targets with low RCS.

PAs are divided into different types of classes concerning their mode of operation. For a CW RADAR system, linear PAs are desirable, such as Class-A and Class-AB, while FMCW can operate with non-linear PAs due to constant envelope modulation. Class-A PAs operate similarly to a conventional amplifier stage and have a full conduction angle. The class-AB PAs are biased to have a lower conduction angle for increased efficiency. For implementing the necessary amplification stage of a Class-A PA, similar topologies investigated in the design of an LNA can be used. CE and cascode stages are commonly used for PA's transconductance stages. The advantages for these respective configurations discussed within Section 3.2.1 are also true for the design of a PA. However, there are other metrics to be considered for the design of an mm-wave PA. While the CE stage has a better power handling performance compared to cascode due to reduced parasitics, for a system that requires high gain on the transmit path, it is not feasible. Cascode topology shows an important property for the PA design. For HBTs, it is possible to achieve higher gain and output power with cascode topology since driving HBTs with forced emitter current is known to increase collector-emitter breakdown voltages  $BV_{CEO}$

[56]. This allows the common-base transistor of cascode to have a higher breakdown and allows the use of a higher supply voltage, thus a greater output voltage swing.

Figure 29 shows the schematic of the designed PA. The PA consists of three pseudo-differential cascode stages. The first stage is biased in a way to enable variable gain operation. A configurable PA introduces a degree of robustness and flexibility to the operation of the designed RADAR system. The gain of the PA can be adjusted to prevent the receiver from saturating while detecting large RCS targets at a very close range. Having a configurable PA in the chip also enables it to be switched between TRX and RX mode. This ability enables the system to be configured as a multiple-input multiple-output (MIMO) RADAR and synthesize virtual antenna elements, which improves the angular resolution and field of view [57]. The variable gain operation is performed by adjusting the base voltage of the common-base transistor, and the PA can be turned off entirely by turning off the bias for the common-base transistor. The collector voltage of the first stage is set to 1.7 V prevent the CB device from breaking down when it is turned off. This means during nominal operation,  $V_{cas} = 1.4V$ , the collector voltage of the CE device is 550 mV, which is still acceptable as HBTs in advanced SiGe nodes still provide a considerable gain while operating in saturation region [58]. One drawback of having low-supply voltage for the first stage means that the linearity of the stage will be lowered. To overcome this, the second and third stages are designed with a higher supply voltage, exploiting the previously mentioned property of cascode topology. The transistor sizes, as well as the bias voltages, are increased for the last two stages for increased gain and power handling. Figure 30 shows the 3D view of the designed PA. For the interstage matching between the first and second stages, a transformer is used. The supply voltage of the first stage, and the base bias for the second stage supplied from the center taps of the primary and secondary windings of the transformer. T-type matching networks are used for the latter two stages with transmission lines. All transmission lines are implemented with TM2-M1 configuration, except in the last stage where TM2-M3 configuration is used. Around the cores of the last two stages, an M3 ground shield is implemented to improve grounding performance. Bypass capacitors are included in the bias lines, and they are kept as close as possible to the base node of the CB transistor to avoid stability issues.

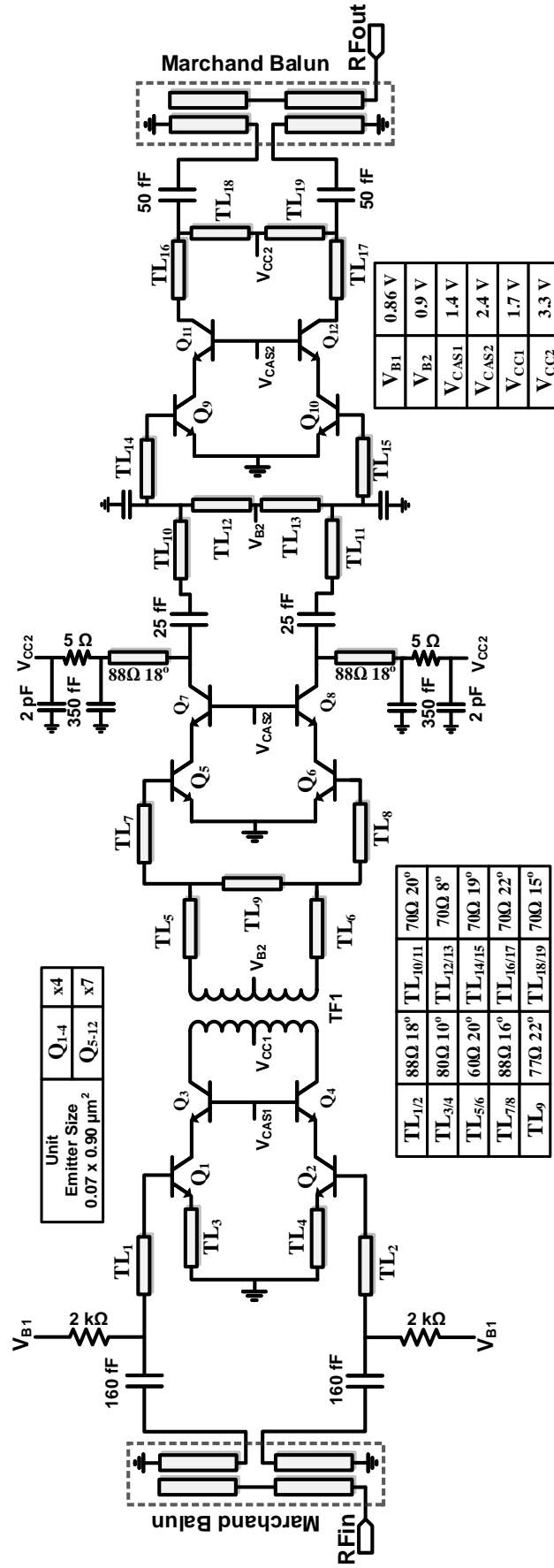
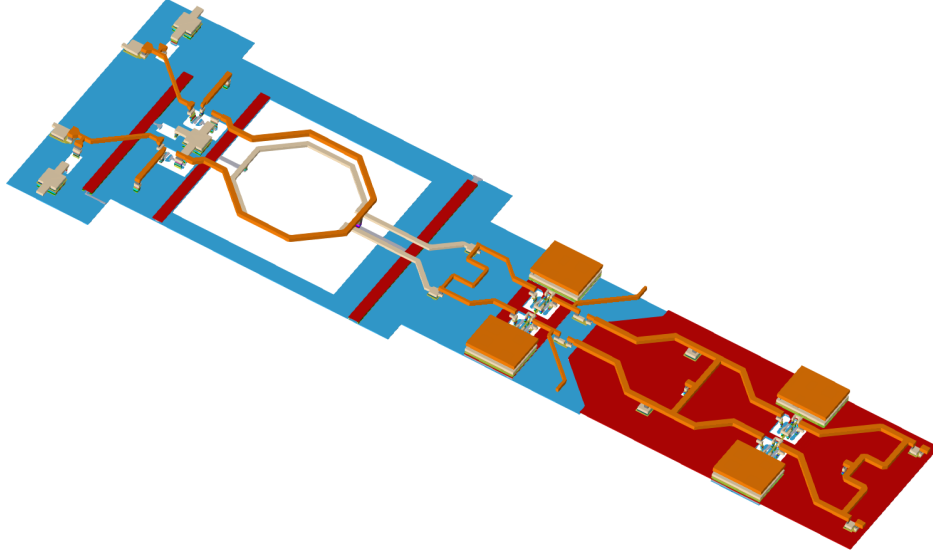


Figure 29: The schematic of the designed PA. (Electrical lengths of the transmission lines are given for 122 GHz)



**Figure 30:** 3D Layout view of the designed PA.

### 3.4.2 Simulation Results

The full layout of the designed PA is shown in Figure 31. Similar to all presented circuit breakouts, Marchand baluns are included for measurement purposes. The total die area including the pads and baluns is  $0.52 \text{ mm}^2$  ( $0.96 \text{ mm} \times 0.54 \text{ mm}$ ), and the effective area is  $0.18 \text{ mm}^2$ . The pad configuration and the metal ground plane under the circuit are similar to the previously presented blocks. The PA draws  $3.8 \text{ mA}$  and  $44 \text{ mA}$  quiescent DC current from the  $1.7 \text{ V}$  and  $3.3 \text{ V}$  supplies respectively. Figures 32 - 35 presents the simulation results for the designed PA. The PA exhibits a peak gain of  $34 \text{ dB}$  at  $121 \text{ GHz}$ , with a  $3\text{-dB BW}$  between  $116\text{-}126 \text{ GHz}$ . The input return loss is greater than  $10 \text{ dB}$  between  $110\text{-}128 \text{ GHz}$  while the output of the PA is matched to a lower impedance for increased power delivery to the load, which can be conjugate matched to an antenna in the future. The PA's simulated output-referred  $1 \text{ dB}$  compression point is  $9.9 \text{ dBm}$ , and the simulated saturated output power is  $11.6 \text{ dBm}$  at  $122 \text{ GHz}$ . The simulated power-added efficiency of the PA is  $\%4$  when operated at  $\text{OP1dB}$  level, while it shows a peak PAE of  $\%7.5$  while operated in the  $\text{Psat}$  level. Table 4 shows a comparison of the designed PA to the state-of-the-art silicon PAs.

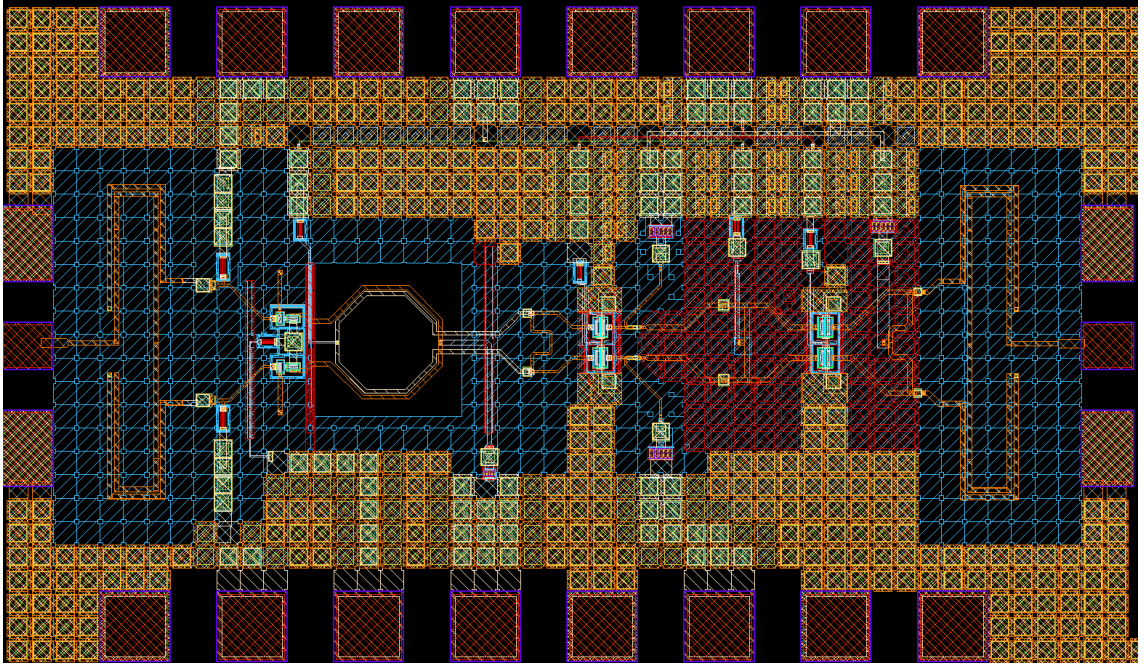


**Figure 31:** Layout of the PA breakout.

**Table 4:** Performance comparison of the designed PA with previously reported PAs implemented using silicon processes.

Ref	[59]	[60]	[61]	[62]	This*
Tech.	16nmFinFET	65nm CMOS	0.13 $\mu$ m SiGe	0.13 $\mu$ m SiGe	0.13 $\mu$ m SiGe
Topology	2-way Combined Neutralized CS	2-way Combined Neutralized CS	Diff. Cascode	Diff. Cascode	Pseudo-Diff. Cascode
Center Freq (GHz)	135	118	139	114	122
Peak Gain (dB)	19	22.3	26	18.5	34
$P_{DC}$ (mW)	162	N/A	N/A	231	152
$OP_{1dB}$ (dBm)	7.1	12.2	0.2	8.5 <sup>+</sup>	9.9
Psat (dBm)	13.1	14	6.2	11.8	11.6
$Pae_{max}$ (%)	11	10.2	3	6.3	7
Area (mm <sup>2</sup> )	0.062	0.34	0.65	0.35	0.18 <sup>#</sup>

\* Simulation # Area without pads + Inferred from the graph

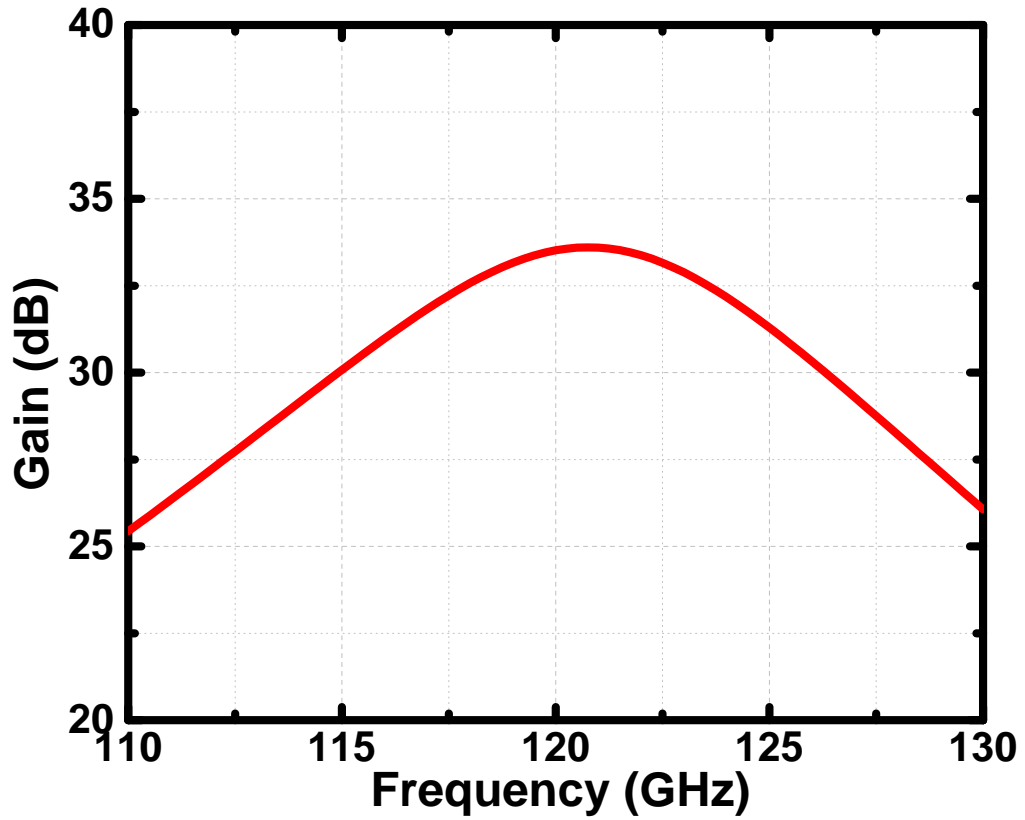


Figure 32: Simulated small-signal gain of the designed PA.

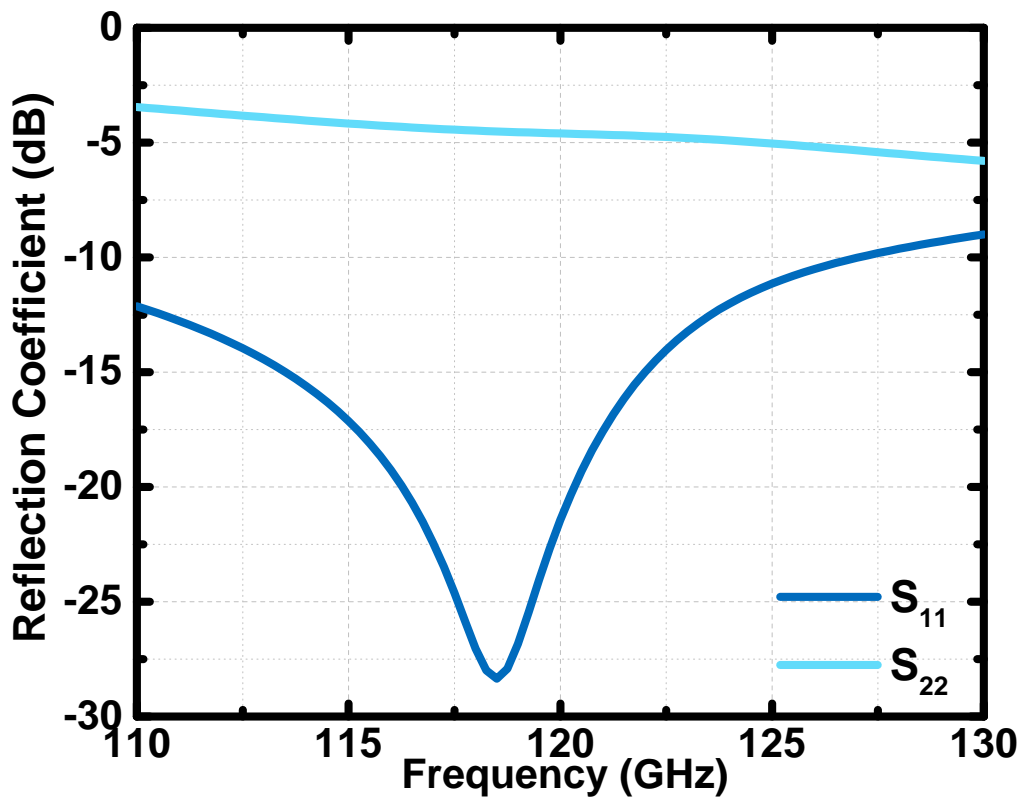


Figure 33: Simulated input and output reflection coefficients of the PA.

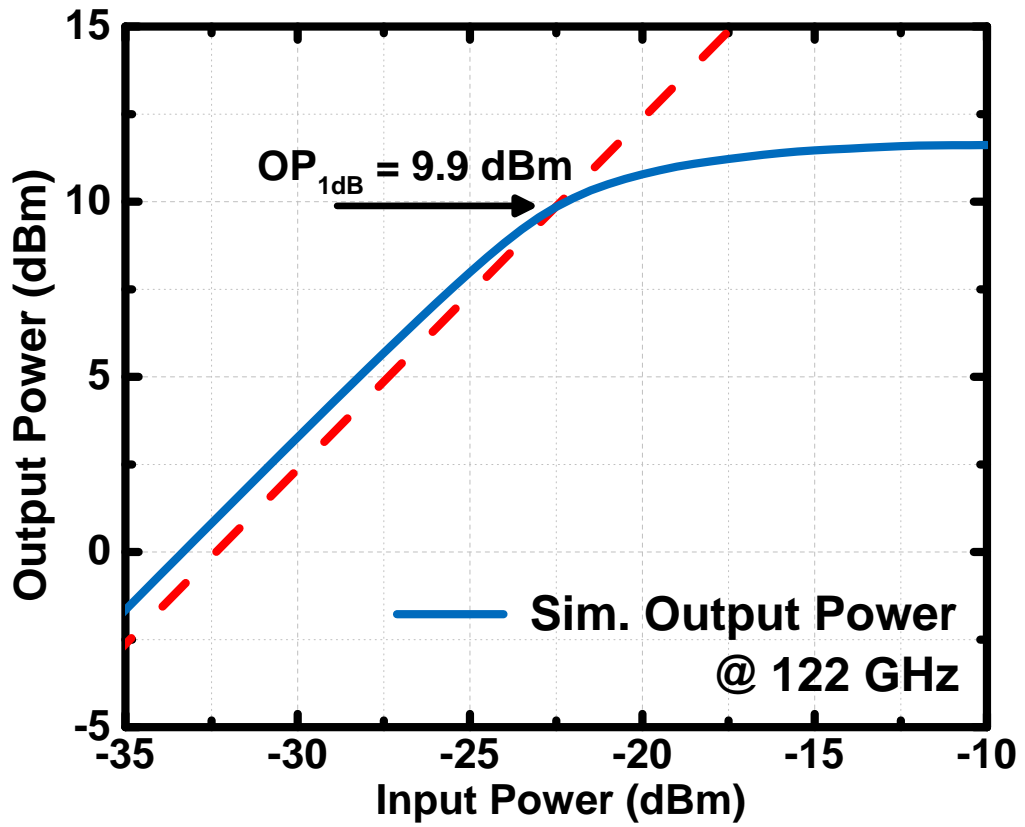


Figure 34: Simulated output referred 1 dB compression point of the PA at 122 GHz.

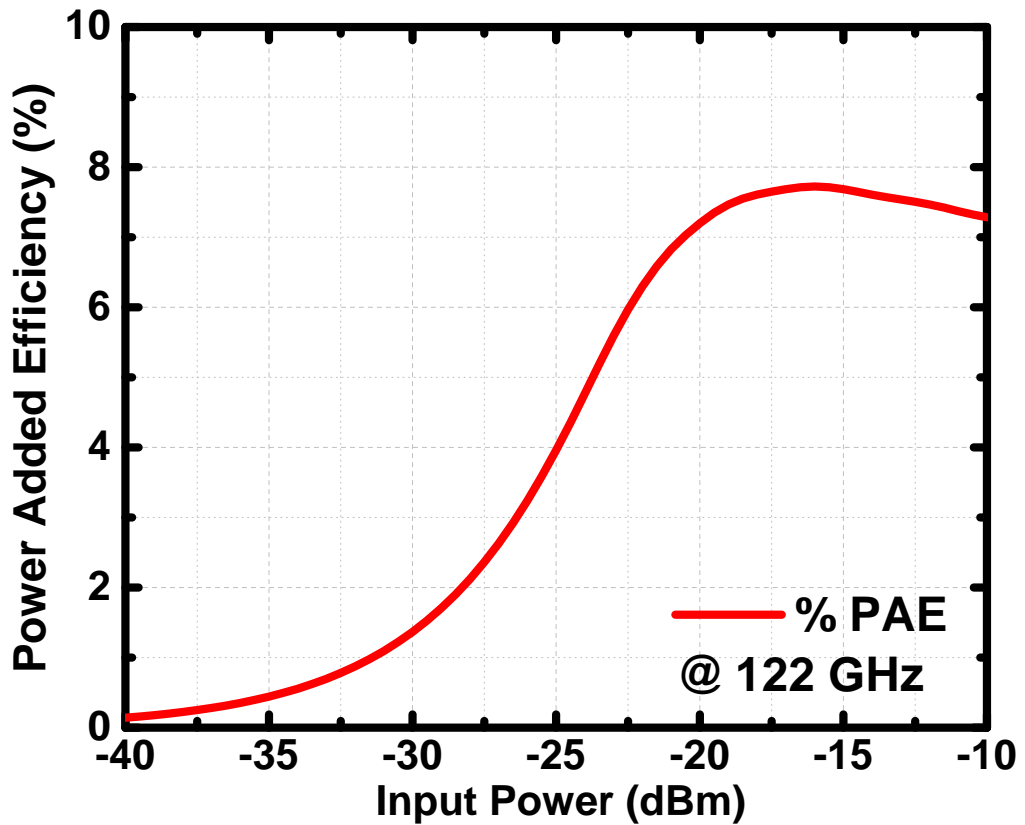
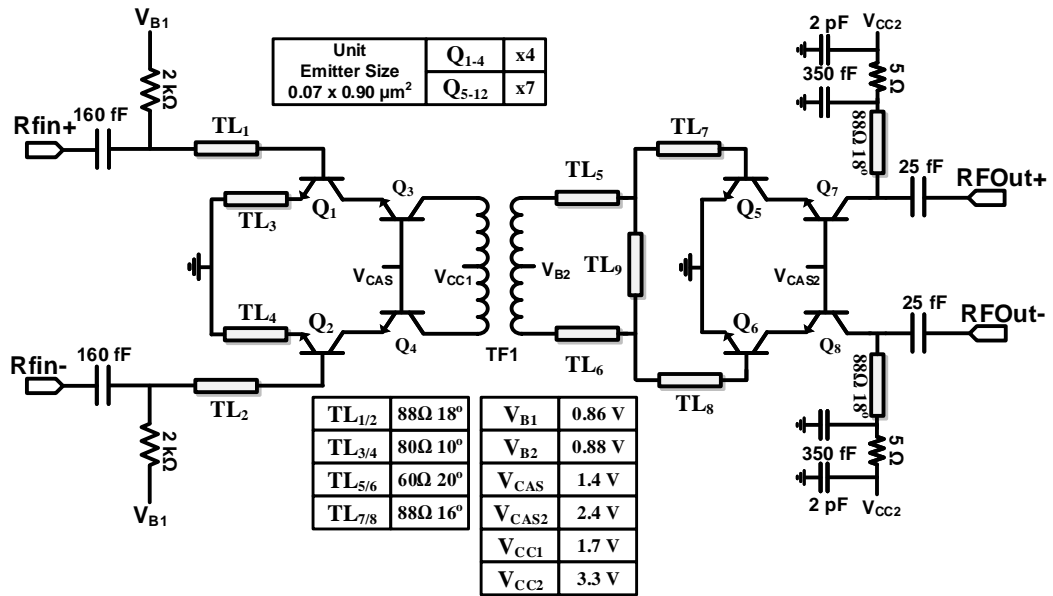


Figure 35: Simulated power added efficiency of the PA at 122 GHz.

## 3.5 LO Buffer Amplifier

### 3.5.1 Circuit Design and Implementation

The LO drive level of the mixer is critical for its performance as it directly affects metrics such as CG, linearity, and NF. In a system-level scope, the LO signal to be fed into the mixer comes from the frequency multiplier by flowing through the single-ended to differential power splitter. Since the multiplier has a limited input power from the VCO+PLL chain, which limits the output power, the amplification of the LO signal is required. The LO signal sees a 6 dB reduction in amplitude, excluding the insertion losses, since it will be subject to both single-ended to differential conversion and power division. Figure 36 shows the schematic of the LO buffer amplifier. The first stage of the designed PA is slightly modified to be used as the LO Buffer. Since it was designed to be configurable to enable MIMO operation, as previously discussed, the use of this stage as LO Buffer enables control over the LO drive level of the Mixer. However, the single-stage provides around 12 dB gain with an OP1dB of 0 dBm. To provide a sufficient gain and linearity performance, a second stage is added to the Buffer amplifier. The bias currents are reduced to limit the output power from the second stage and reduce DC power.



**Figure 36:** Schematic of the designed LO Buffer. (Electrical lengths are given for 122 GHz.)

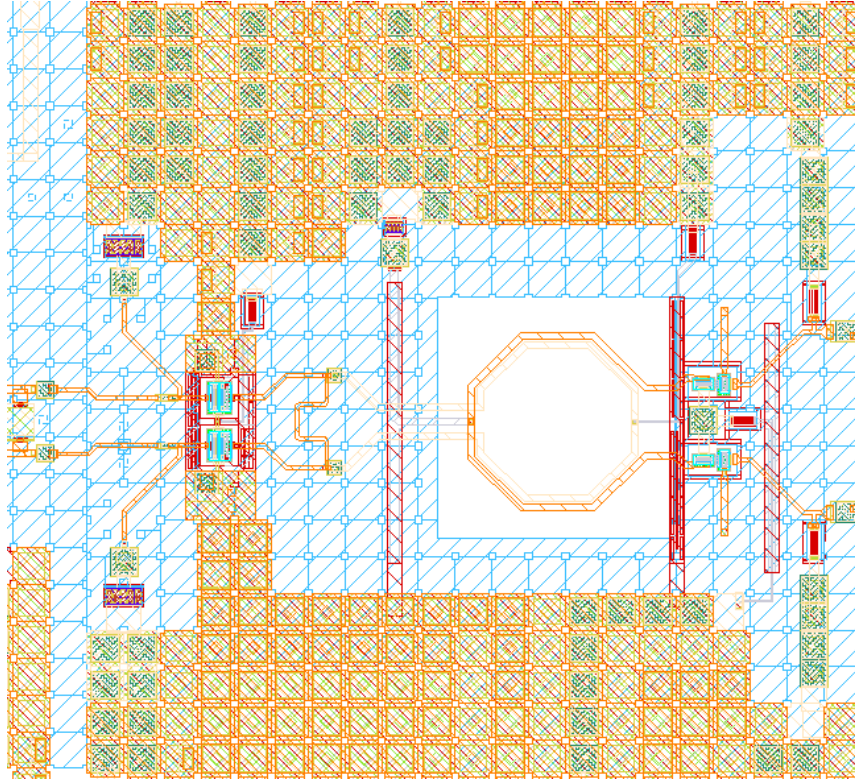


**Figure 37:** Layout of the Buffer Amplifier integrated into the Mixer's LO input.

### 3.5.2 Simulation Results

The layout of the LO Buffer amplifier within the full system is given in Figure 37. The effective area of the LO Buffer is  $0.08 \text{ mm}^2$ . The base bias of the first stage's CB transistor ( $V_{cas}$ ) can be adjusted to adjust the gain of the amplifier. This property is presented in Figure 38 for four different  $V_{cas}$  values. While the initial prototype of the buffer does not include any control circuitry, the gain tuning can be performed by switching different bias circuits. The buffer has a peak gain of 22.5 dB and it can be tuned down to 10 dB without significant degradation in the gain response, and with an acceptable change in matching. The input of the buffer is well matched over the band of interest, while the output is conjugate matched to the balun-less version of the mixer's LO port as shown in Figure 39. Figure 40 shows the simulated linearity performance of the amplifier for  $V_{cas} = 1.4$ , which is sufficient to compensate for the losses and supply the required LO drive to the mixer.

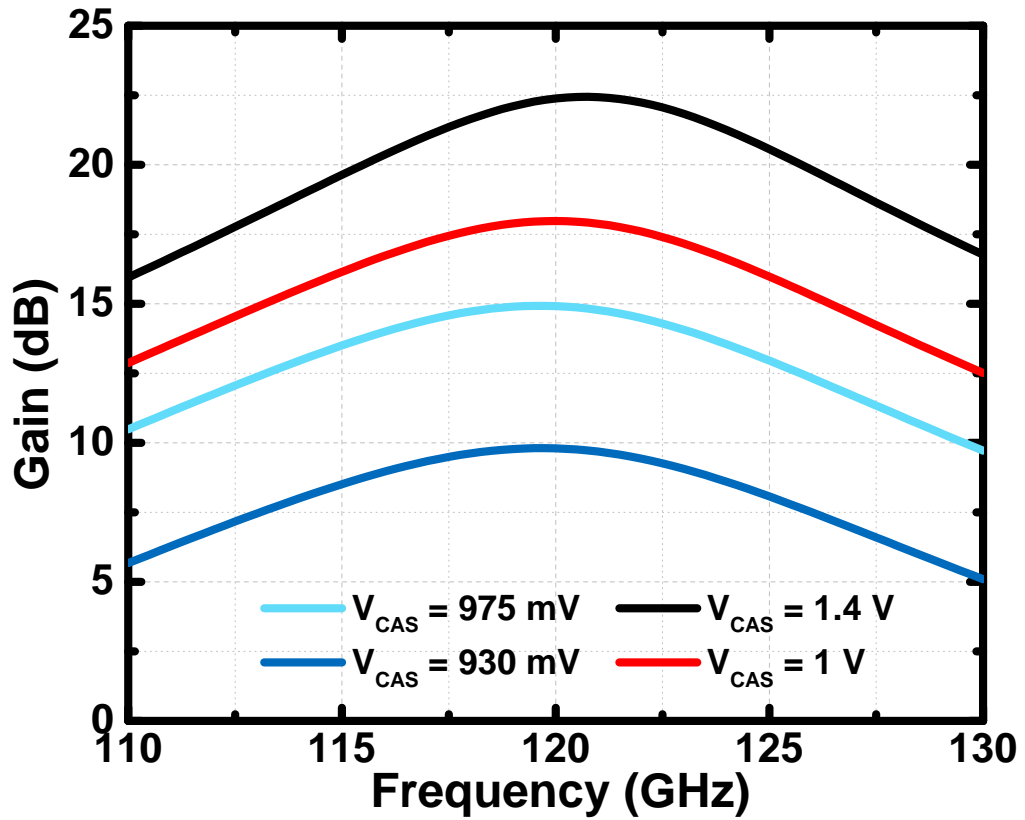


Figure 38: Simulated small-signal gain of the LO Buffer for various control voltages.

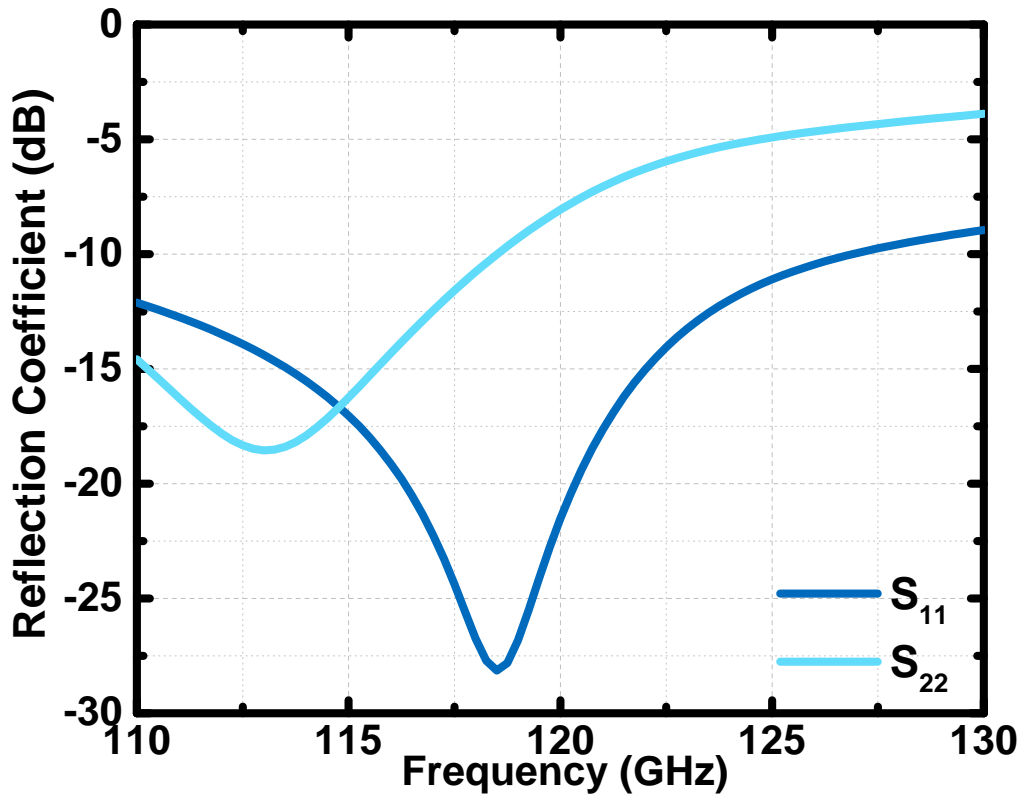


Figure 39: Simulated input and output reflection coefficients of the LO Buffer.

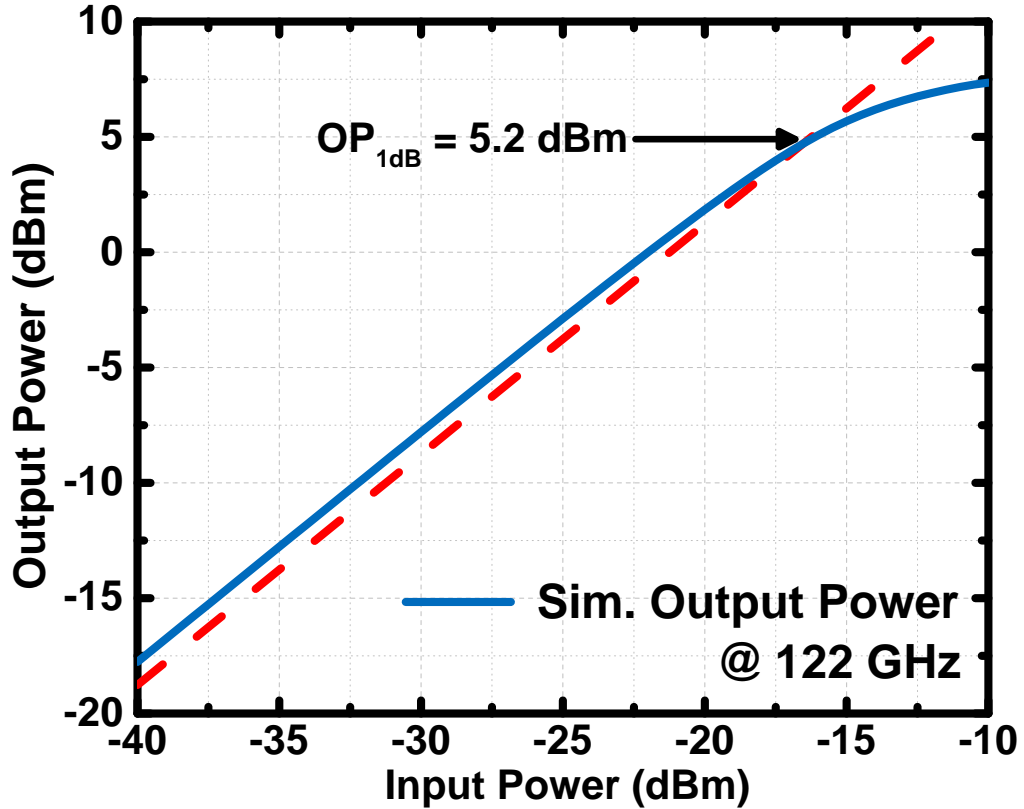
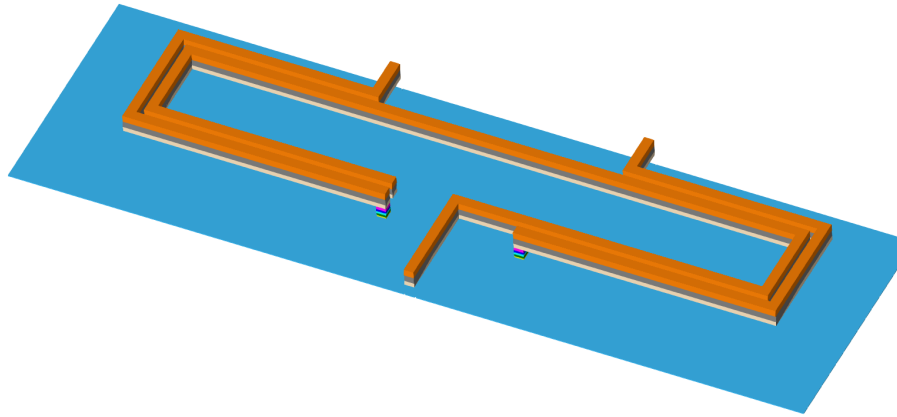


Figure 40: Simulated output referred 1 dB compression point of the Buffer at 122 GHz.

### 3.6 Differential Power Divider and Balun

While differential probes are readily available for the lower frequencies, mainly in GSGSG configuration, they are not available for frequencies above 75 GHz. Measurements in frequencies above 75 GHz are usually performed with the use of frequency extension modules with waveguide probes. As already mentioned within the respective sections for the designed sub-blocks, conversion from the balanced (differential) to unbalanced (single-ended) is necessary for measurements. To perform this conversion, Marchand Baluns are used within the breakouts of the sub-blocks as well as the Tx and Rx ports of the system.

Marchand Balun is made of two sections of coupled  $\lambda/4$  sections. Balanced ends each have a  $\lambda/4$  section with the ends grounded while the unbalanced end has a  $\lambda/2$  section with the end open-circuited. Since Marchand baluns utilize multiple  $\lambda/4$  sections, they are more commonly used in mm-wave frequencies due to smaller wavelength. The 3-D layout view of the designed Marchand balun is shown in Figure 41. The  $\lambda/4$  sections are edge coupled instead of broadside coupled and use



**Figure 41:** 3D Layout view of the Marchand Balun

stacked metals from TM2 to TM1 layers with rows of via connections in between for a reduction in insertion loss performance. The designed balun occupies an area of  $(270 \mu m \times 80 \mu m)$ . Figure 42 presents the simulation results for the designed Marchand balun. The balun shows a maximum phase error of 4 degrees while the amplitude error is less than 0.15 dB between 110-130 GHz. The maximum insertion loss of the balun is 2.35 dB at 130 GHz, with an average of 2 dB between 110-130 GHz.

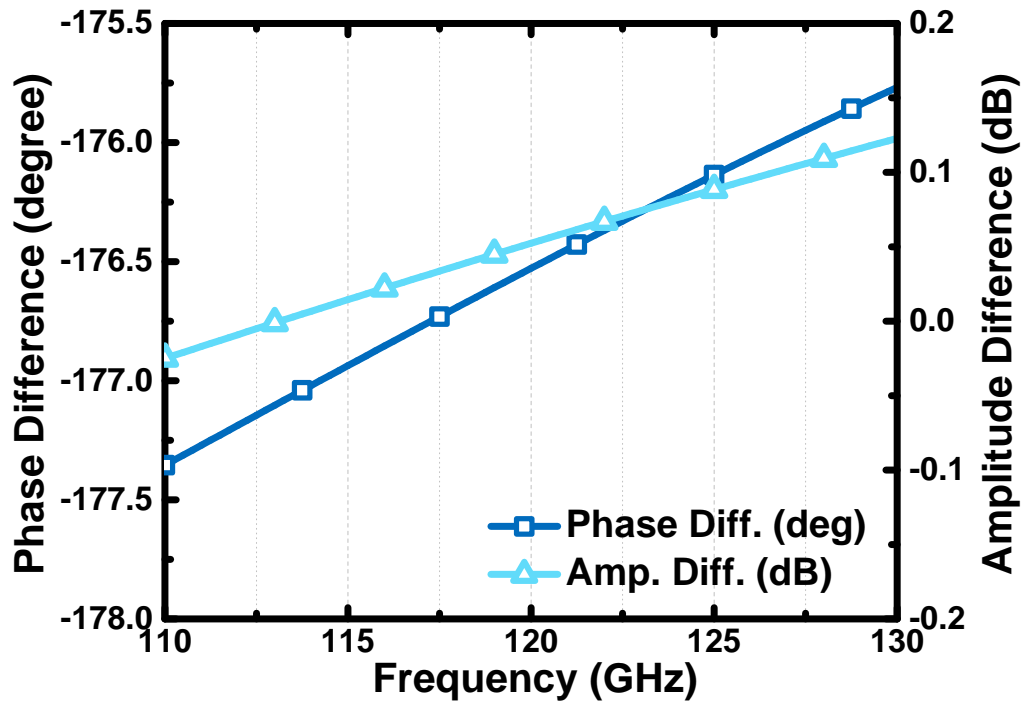


**Figure 42:** Simulated phase and amplitude difference of the Marchand Balun.

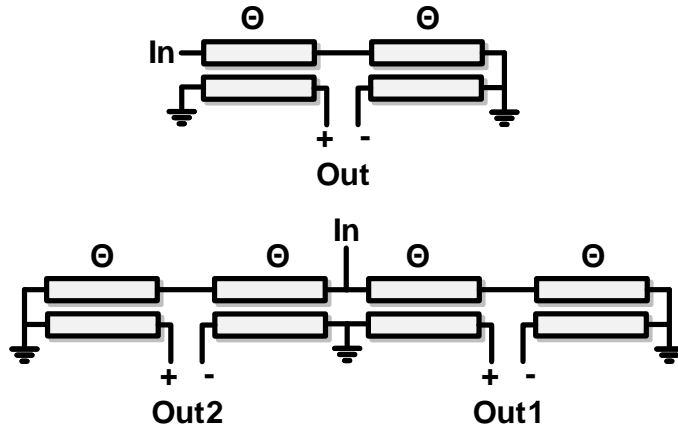


**Figure 43:** Schematic of the modified Marchand balun structure.

Since the Frequency Multiplier in the system is based on the push-push topology, its output is single-ended. This means an additional balun at 122 GHz is required after the frequency multiplier to convert the output to differential to be fed into other sub-blocks. Moreover, since the transmitted signal needs to be fed into both the mixer and PA, a power divider, or a coupler is also required. However, the implementation of a Wilkinson divider and two baluns (or vice versa) would be very inefficient in terms of chip area. As a solution to handle both single-ended to differential conversion and power division, the method proposed in [63] can be used. Figure 43 shows the schematic of the method presented in [63], which works on the principle of the modification of the Marchand balun structure.  $\lambda/4$  sections are swapped with an electrical length of  $\theta$  where  $\theta < \lambda/4$ , and the open-circuited end of the unbalanced port is grounded. Enabled by the form factor reduction due to the use of smaller electrical length, two of these structures can be cascaded to share their unbalanced ports to create a power divider. Figure 44 shows the 3-D layout view of the single-ended to differential power divider (referred to as Balun-splitter). It occupies a total area of  $(200 \mu\text{m} \times 180 \mu\text{m})$ . Since the splitter will be placed in a central location within the designed system, TM2-M3 configuration is used to be able to route DC connections under the splitter while keeping them isolated from the LO signal. Following the analysis from [63], the required electrical length ( $\theta$ ) is found as 32 degrees. The width and spacing between the lines are chosen as  $4 \mu\text{m}$  and  $2.1 \mu\text{m}$  similar to the Marchand Balun.

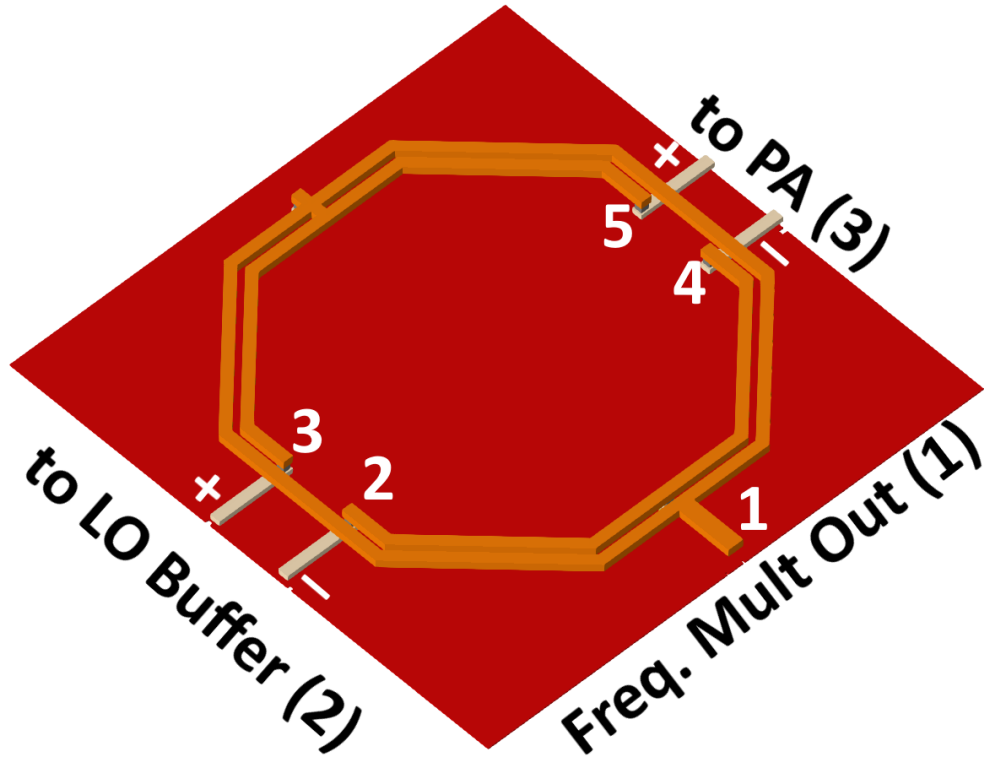


**Figure 44:** 3-D Layout view of the Balun-splitter.

Figure 45 shows the simulated phase difference performance of the Balun-splitter. In this figure, Port 2 refers to Terminals 2-3, and Port 3 refers to Terminals 4-5 from Figure 44. When the splitter is fed from Port 1, the phase at the terminals 2 and 3 are subtracted from each other to find the phase difference from Port 1-to-2. The designed Balun-splitter shows a simulated error of less than 3 degrees between 70-170 GHz, and the phase response for Ports 1-to-2 and 3 are similar. Within the band of interest, the phase error is less than 1.5 degrees. Figure 46 shows the transmission coefficient of the Balun-splitter. This time, only the terminals 2 and 3 at Port 2 are analyzed. It is important to note that there is a 6 dB inherent loss at  $S_{21/31}$  due to the single-ended to differential conversion and power division. This means the designed splitter has a maximum insertion loss of 3.4 dB while the maximum amplitude error is 1 dB at 110 GHz.

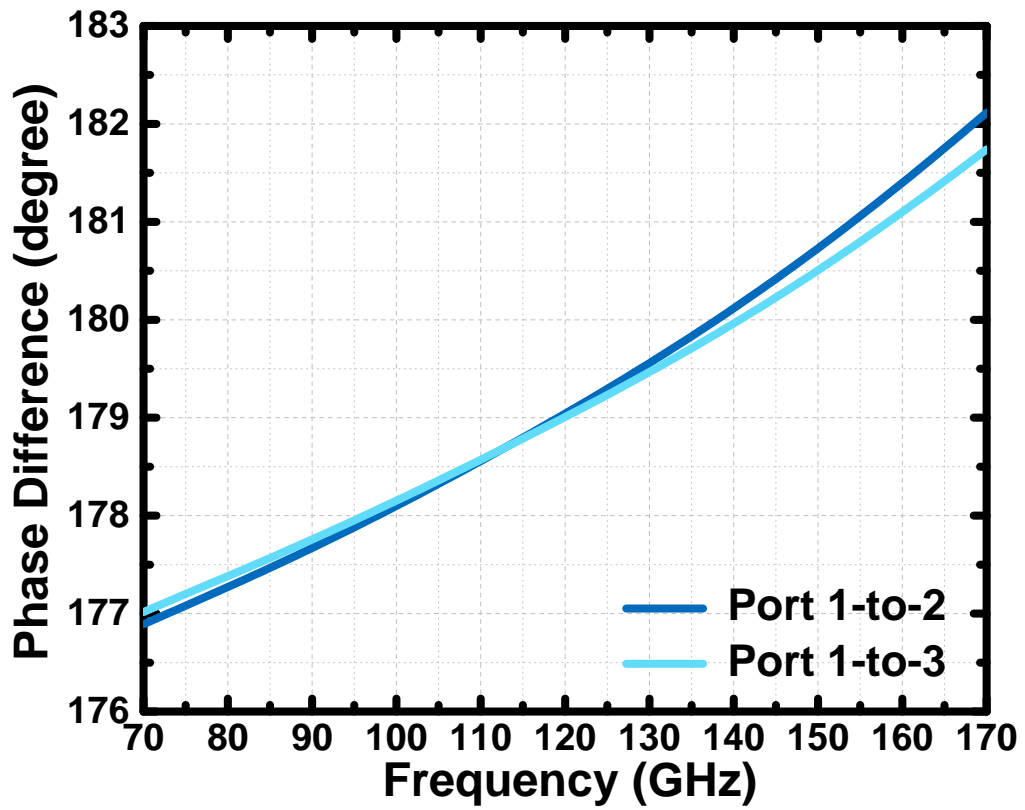


Figure 45: Simulated phase difference at splitter's outputs.

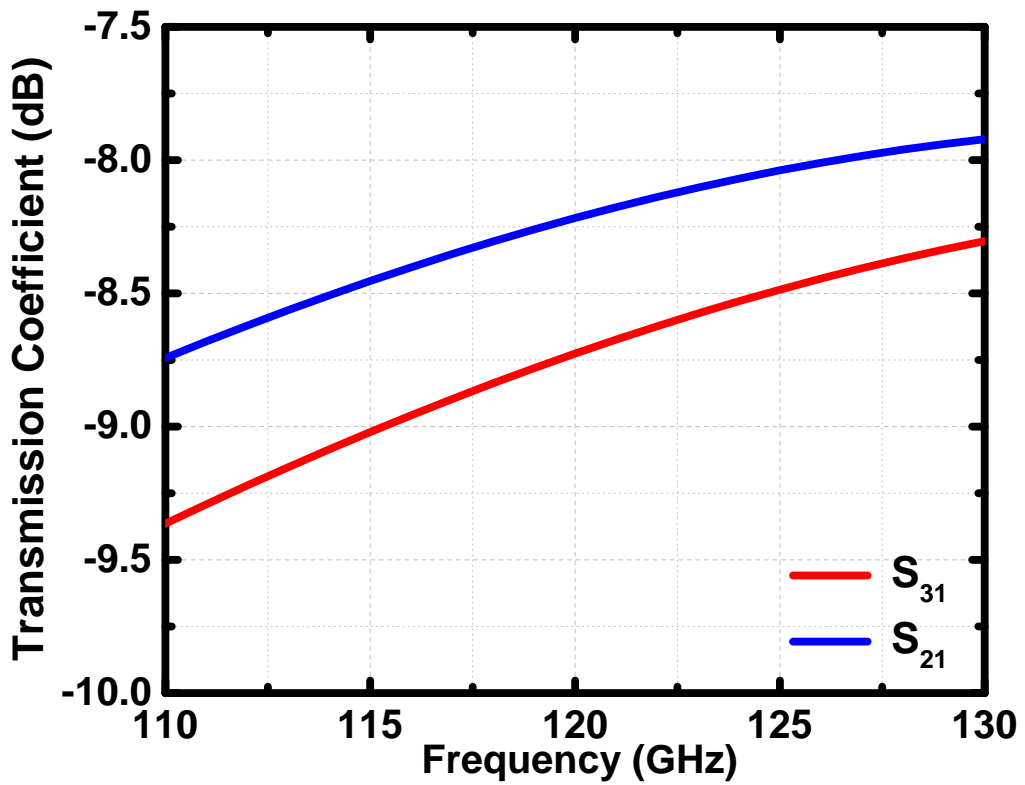


Figure 46: Simulated transmission coefficients of the splitter.

## 3.7 x16 Frequency Multiplier

### 3.7.1 Circuit Design and Implementation

The generation of a chirp signal using a fundamental VCO operating between 110-130 GHz is challenging. The VCO requires a PLL to be locked, which will, in turn, require frequency dividers with a high division ratio. Frequency dividers that operate at high frequencies consume a lot of DC power, which is undesirable for the TRX chip. Frequency multiplication is an alternative solution to this problem. The chirp signal can be generated at a lower frequency, either by using an on-chip or off-chip VCO-PLL chain. The generated chirp signal is then multiplied in frequency to bring it up to 120 GHz range without degrading its frequency modulation scheme.

Frequency multiplication is realized by exploiting the harmonic generation properties of the transistors. Frequency multipliers are grouped into two, similar to mixers, as passive and active multipliers. Passive multipliers generally use diodes such as Schottky or Pin diodes [64]. However, they suffer from high conversion loss and low efficiency. Active multipliers can provide lower conversion loss at the cost of DC power consumption.

The state-of-the-art off-chip VCO-PLL chains support a fundamental frequency up to 15 GHz. This means at least a multiplication factor of 8 is required to bring the output of the VCO-PLL chain to 120 GHz range. Considering the wire-bond transitions and losses of the connector cables at 15 GHz, it is beneficial to use a lower frequency chain to reduce these losses. To generate the chirp signal, LMX2594 from TI is used [65] between the frequency ranges of 6.875-8.125 GHz since the wire-bond transition losses are tolerable at this frequency range. This frequency range corresponds to 110-130 GHz when it is multiplied by 16.

The generation of higher-order harmonics from a single-stage multiplier is disadvantageous in terms of conversion loss, efficiency, and also chip area due to the required filtering. Also, harmonic and fundamental rejection is important for frequency multiplier since the presence of unwanted harmonics with high power levels will disturb the desired signal and introduce additional phase noise. Figure 47 shows the schematic of the designed x16 frequency multiplier. To generate the 16th harmonic of the fundamental frequency of 6.875-8.125 GHz, a four-stage cascaded frequency doubler chain is used. All four doubler stages are implemented in the

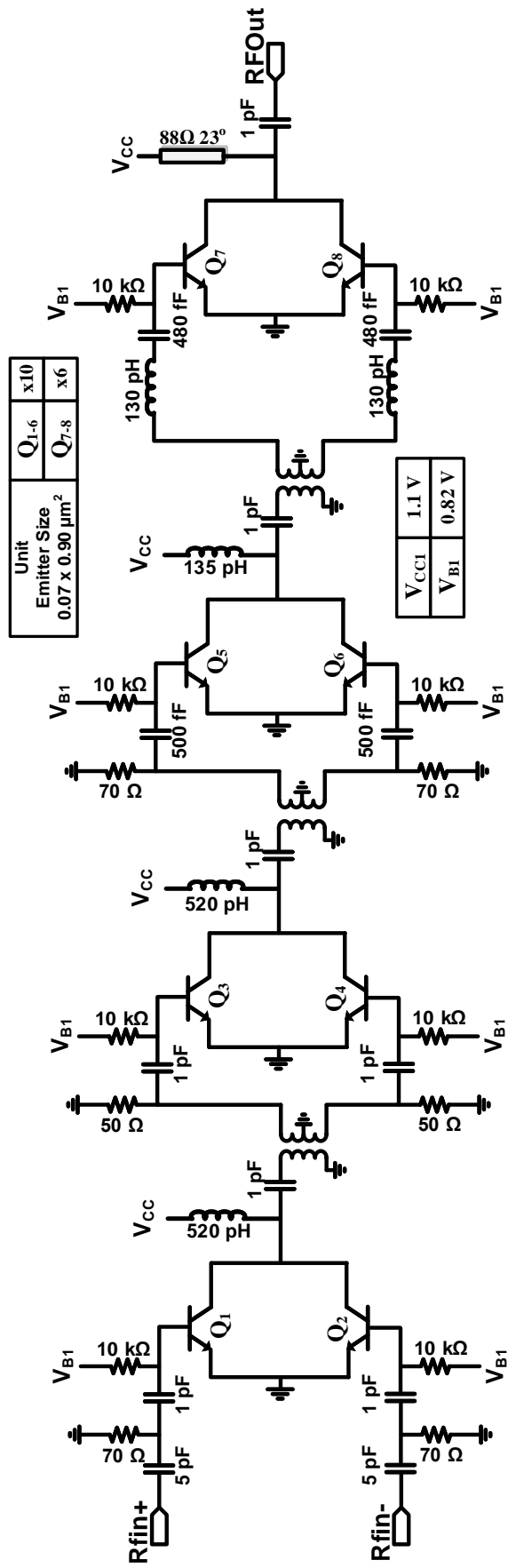
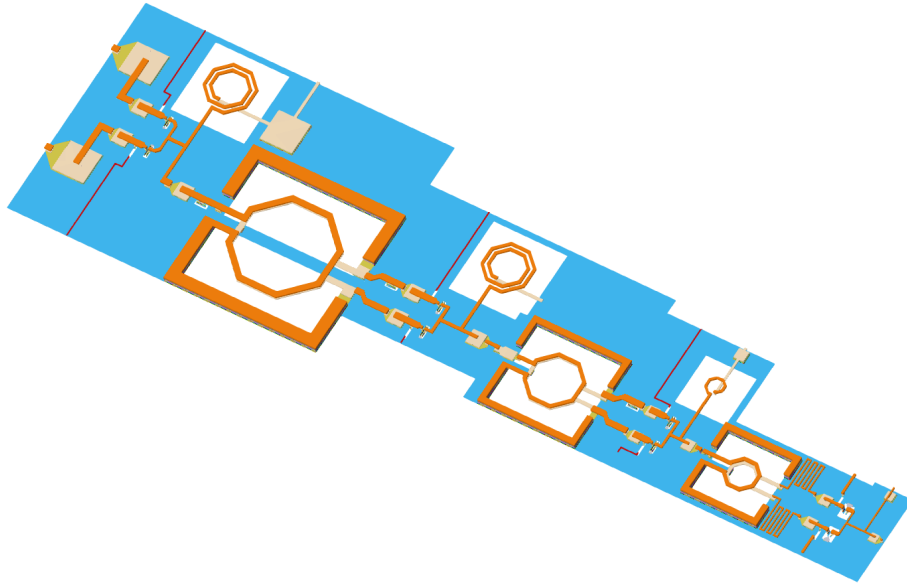
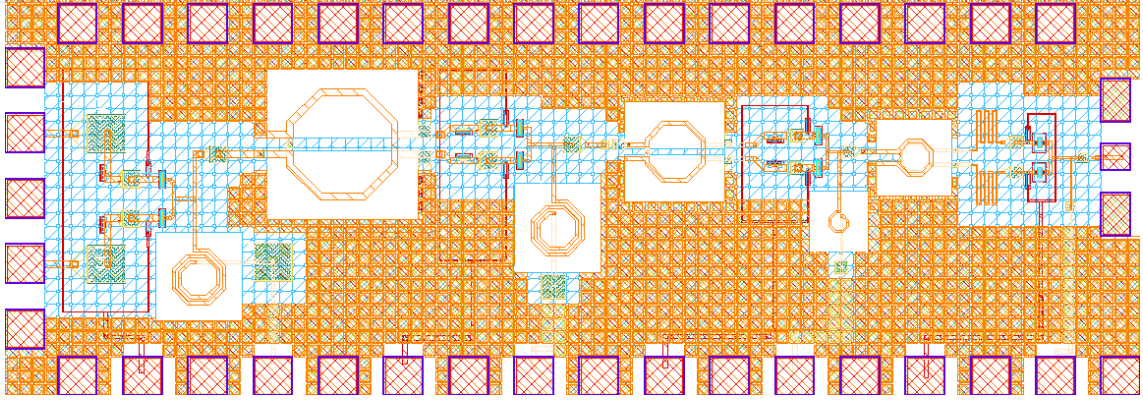


Figure 47: The schematic of the designed frequency multiplier.



**Figure 48:** 3-D Layout view of the x16 Frequency Multiplier.

push-push configuration. The push-push configuration utilizes balanced architecture and works on the principle of suppressing the odd harmonics at the virtual ground point at the collector while combining the in-phase even harmonic components [66]. Push-push doublers have lower DC power consumption, higher efficiency, and lower complexity compared to gilbert-cell based doublers. However, they suffer from worse conversion loss performance, and since it depends on the class-B bias, the conversion loss degrades significantly for lower input powers. For the designed x16 multiplier, the first doubler brings up the frequency to 13.75-16.25 GHz while the fundamental tones are canceled at the collector node of ( $Q_{1/2}$ ). The interstage baluns are implemented as transformer baluns using TM2 and TM1 layers, to provide single-ended to differential conversion for the following doubler stage. The interstage baluns are designed for the frequencies of interest for their respective doubler stages, and they provide limited transmission to higher-order even harmonics. Transistor numbers, as well as the balun form factors, start to get smaller towards the end of the doubler chain since the frequency of interest starts to get higher. The transistors are biased in class-B point to increase the harmonic generation capabilities for maximum output power. Figure 48 shows the 3-D layout view of the designed frequency multiplier. A Metal-1 ground plane is used under the whole circuit, similar to the previously presented sub-blocks. Spiral inductors are used for the lower frequency doubler stages. The input signal can be taken differentially from TI LMX2594 using



**Figure 49:** Layout of the x16 Frequency Multiplier.

wirebond transitions to the PCB, eliminating the need for an area-inefficient on-chip balun at the 7 GHz range. This circuit was designed by Hamza Kandis, who is a member of SUMER Research Group.

### 3.7.2 Simulation Results

The full layout of the designed frequency multiplier is given in Figure 49. The total area of the integrated circuit, including the pads, is  $1.02 \text{ mm}^2$  (1.7mm x 0.6mm). As previously mentioned, the input is left differential, to be measured with a GSGSG probe while the 122 GHz output is single-ended.

Figure 50 shows the simulated input matching of the frequency multiplier between 6.8-8.2 GHz. The multiplier is matched to  $100 \Omega$  differential, and since the multiplier will require wirebond connections to the PCB for the system implementation, the use of off-chip matching circuit after the bondwires is necessary. The conversion loss of the designed x16 multiplier is presented in Figure 51. Since the input power will be supplied by the TI LMX2594 within the system implementation, 0 dBm is selected considering the losses on the connectors and bondwires. The multiplier has a conversion loss lower than 10 dB for an input frequency of 6.875-8.125 GHz, which corresponds to an output frequency range of 110-130 GHz. The simulated harmonic spectrum at the output of the multiplier is shown in Figure 52 for an input frequency of 7.625 GHz. The worst-case harmonic rejection is 31 dBc, between the 16th (122 GHz) and 4th (30.5 GHz) harmonics. The simulated fundamental suppression of the frequency multiplier is greater than 70 dB. 15th and 17th harmonics of the 7.625 GHz, which would fall into the operating frequencies of the PA and LO buffer are suppressed greater than 40 dB.

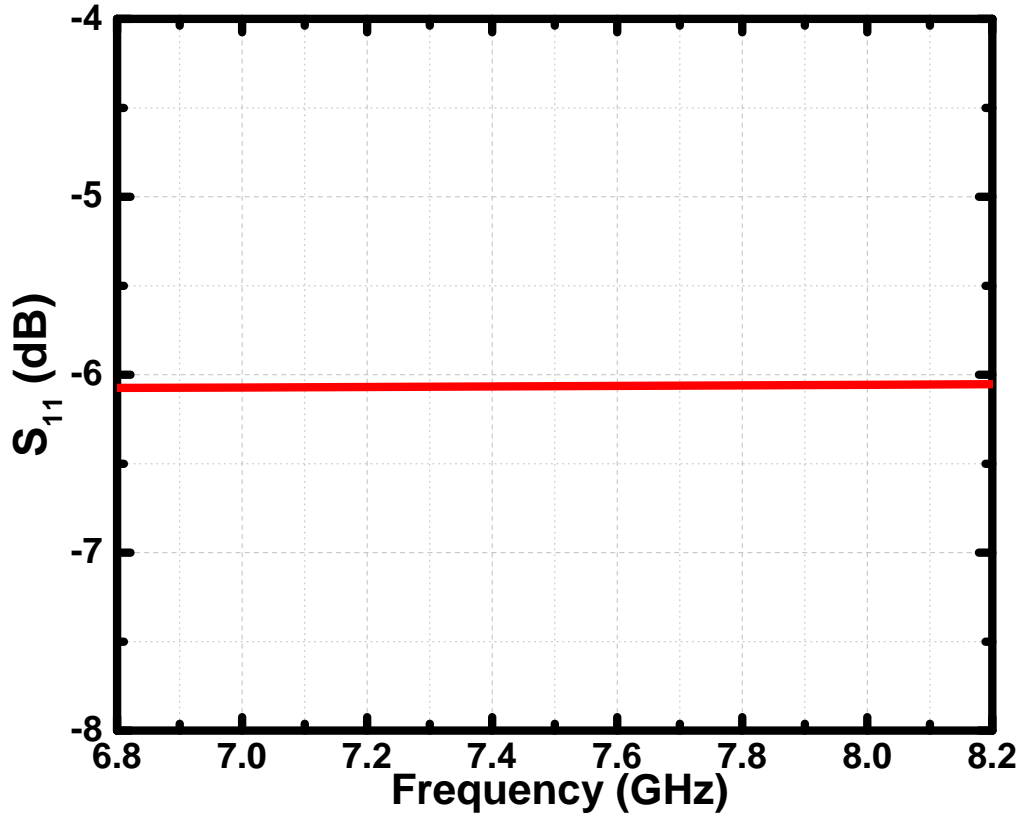


Figure 50: Input reflection coefficient for the frequency multiplier.

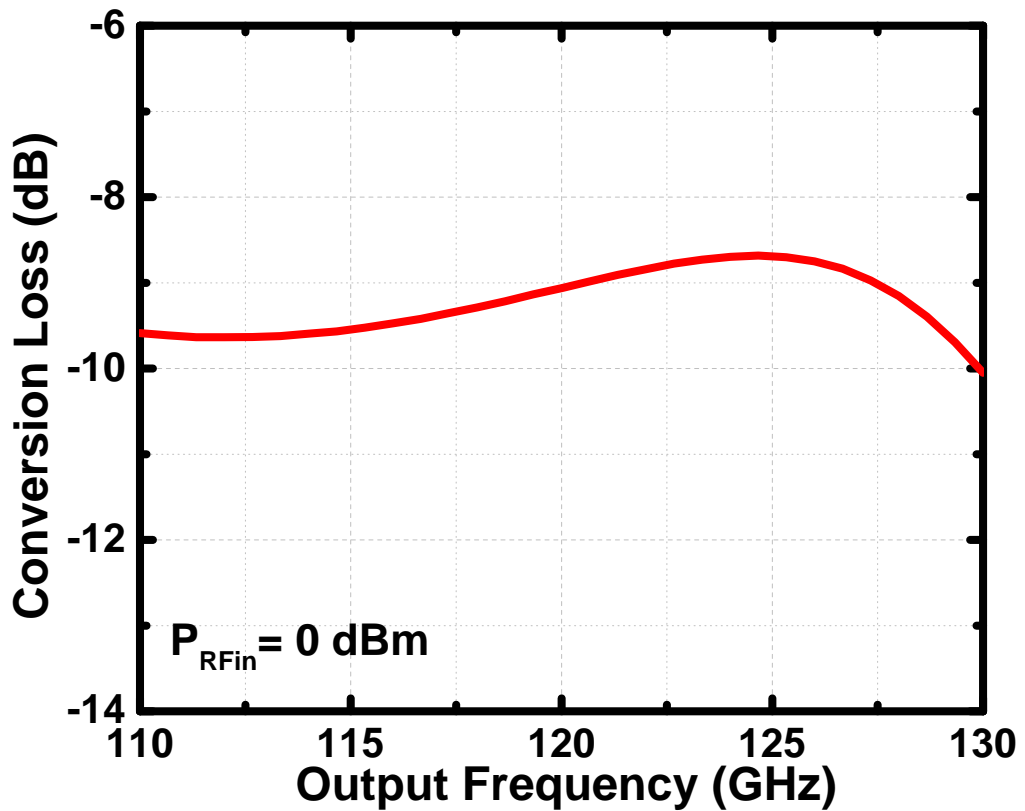


Figure 51: Simulated conversion-loss of the multiplier for a fixed input power of 0 dBm.

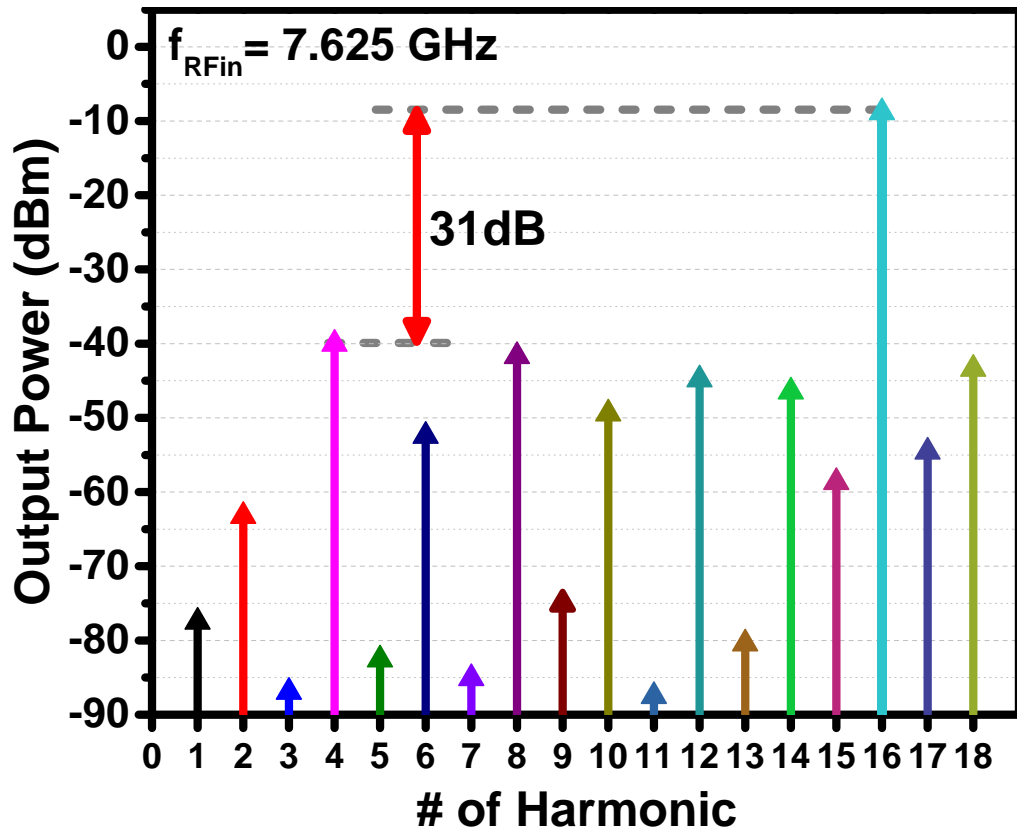


Figure 52: The harmonic spectrum at the output of the frequency multiplier for  $f_{rf} = 7.625$  GHz.

### 3.8 System Implementation and Simulations

All of the presented sub-blocks within the previous chapters are integrated to implement the 122-GHz FMCW RADAR Front-End, as shown in Figure 53. The sub-blocks are outlined within the figure to better show the floorplan of the system. Marchand baluns are included for both Tx-Out and Rx-In ports for measurement purposes, similar to the sub-block breakouts. The external LO between 6.875-8.125 GHz will be taken from TI LMX2594 differentially, to be connected to the chip using bondwires. The single-ended output of the frequency multiplier at 110-130 GHz is routed to the single-ended to differential power divider with the use of a 50- $\Omega$  CPWG with TM2-M3 configuration. The one output of the power divider is connected to the PA while the other output is connected to the LO buffer to drive the mixer. In the Rx side, the LNA is directly connected to the RF port of the mixer since both circuits are built with balanced topologies. The full EM simulations of all designed blocks are combined within Keysight ADS to perform system-level simulations. Simulations are performed using the HICUM model [67], available for the SG13G2 technology, which takes advanced HBT effects into account. For all of the simulations, Marchand baluns at the TxOut and RxIn ports are included.

Figure 54 shows the simulated receiver conversion gain of the system for an IF frequency of 10 kHz while the LO buffer is tuned to supply -3 dBm LO power to the mixer. The full receiver achieves a CG of 31.1 dB at 116 GHz without the inclusion of any baseband circuitry or IF amplification chain. The 3-dB BW covers almost the full bandwidth, from 110-128 GHz. The simulated single-sideband NF of the system is presented in Figure 55. The system has a minimum SSB NF of 9.9 dB at 110 GHz. It is important to note this value includes the 3 dB image noise folding penalty, as well as the average 2 dB insertion loss from the Marchand balun at the input of the receiver. It can also be noted that the 1/f noise corner of the full system still is lower than the selected IF frequency of 10 kHz as there is no significant increase on the SSB NF.

Figure 56 shows the simulated transmitter output power of the system. In this simulation, the input power of the x16 frequency multiplier is kept at 0 dBm, between 6.875-8.125 GHz. 18th order harmonic balance simulation is performed to see the include any adverse effects of the additionally generated harmonics. The full system

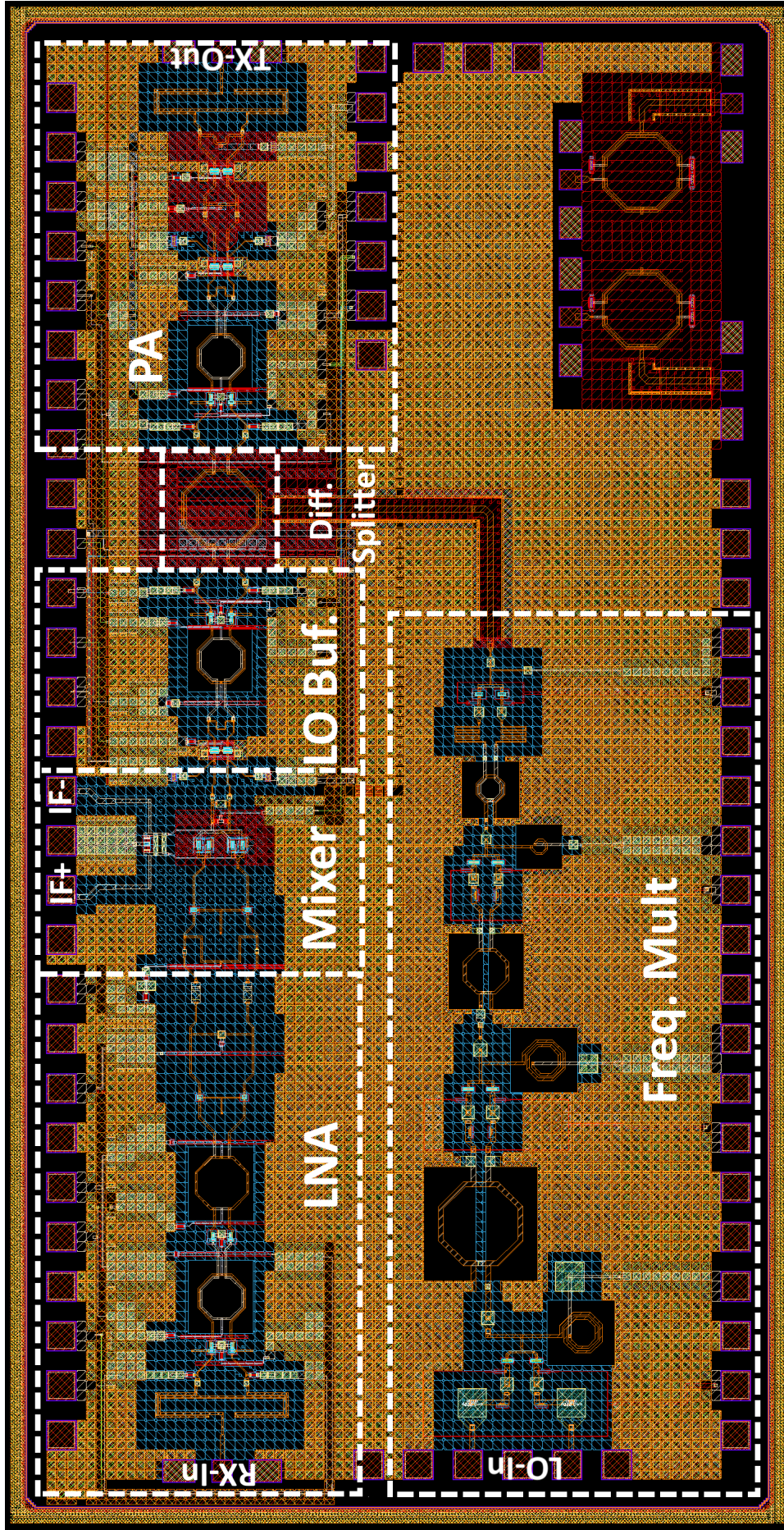
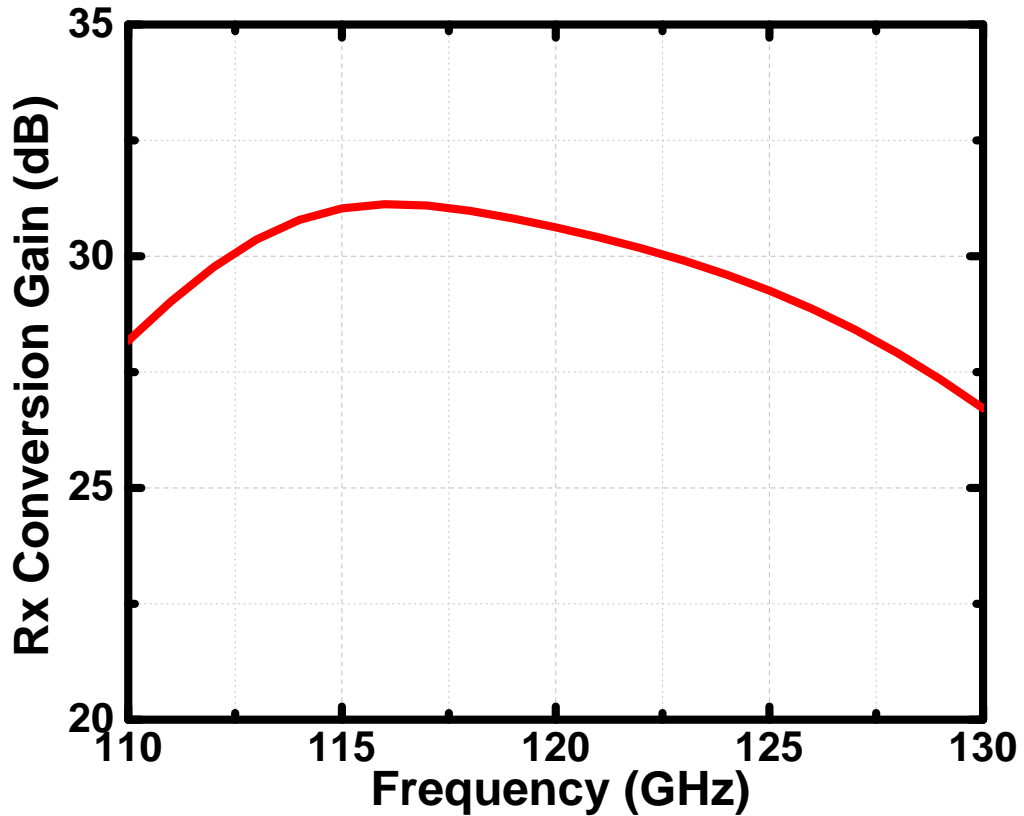


Figure 53: Full layout of the designed 122-GHz FMCW RADAR Front-End.



**Figure 54:** Receiver conversion gain of the full system for an IF frequency of 10 kHz.

has a peak output power of 10.1 dBm for the 0 dBm frequency multiplier input. Recalling Figure 34 from Chapter 3.4.2, it can be seen that PA is operating near saturation. In FMCW systems, the PA can be safely operated in this region due to the constant-envelope modulation, eliminating the need for power back-off [68]. Additionally, the PA can be disabled to bring the system into Rx-only mode by adjusting the tuning voltage of the first stage's CB transistor, bringing the output power to an average of -22 dBm over the frequency. The total power DC consumption of the system is 247 mW. Table 5 presents a comparison of the designed system to the previously reported state-of-the-art FMCW RADAR systems operating at 94 and 122 GHz bands. The designed FMCW RADAR system achieves high Tx power, low SSB NF, high Rx gain, and a low power consumption compared to works with similar levels of integration. The simulation results of the designed system achieves the required performance parameters summarized in Table 2, in Chapter 3.1.2.

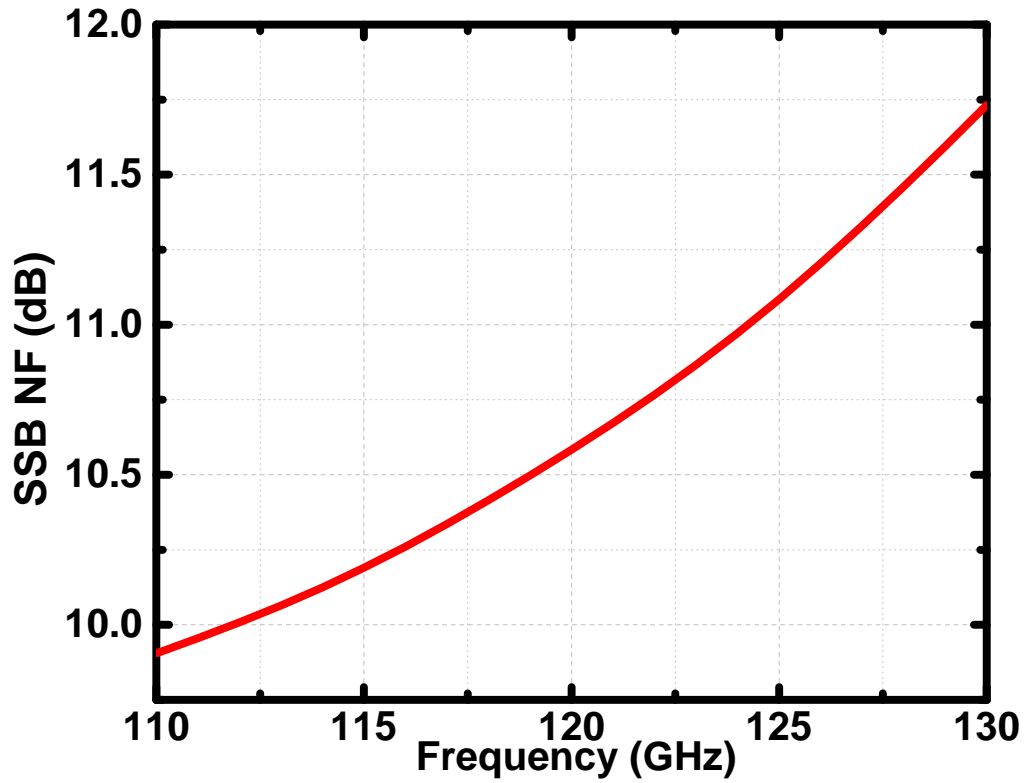


Figure 55: Simulated SSB NF of the system for an IF frequency of 10 kHz.

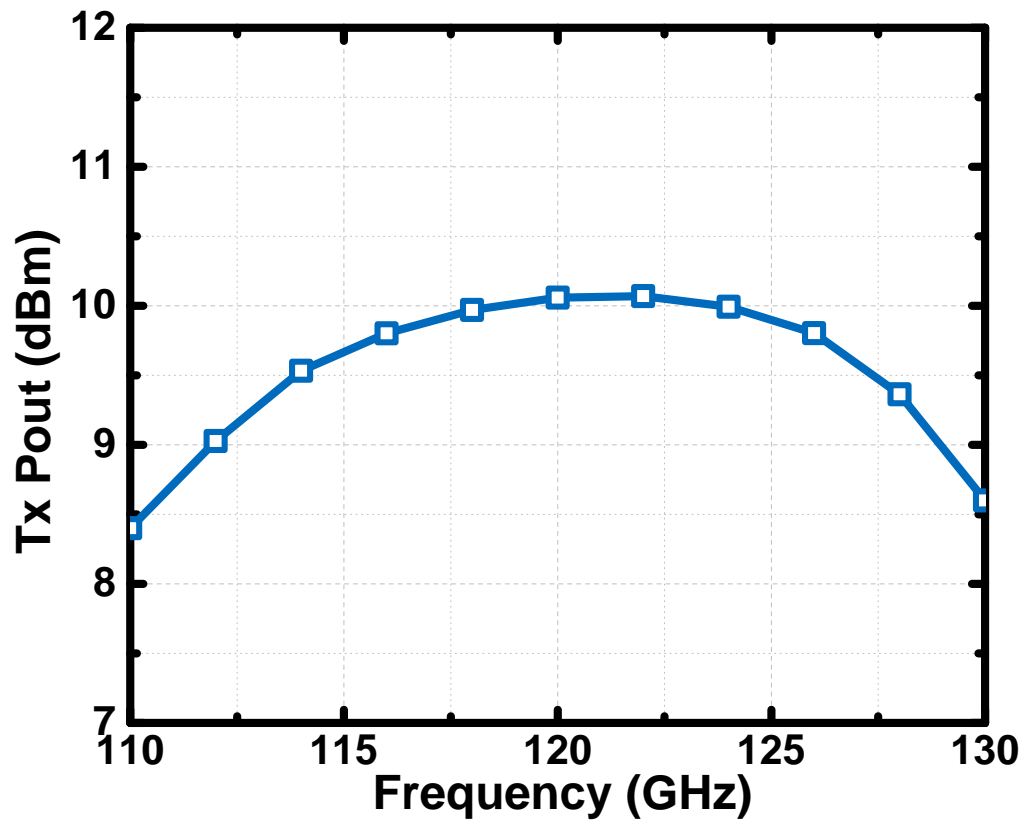


Figure 56: Simulated transmitted output power for 0 dBm multiplier input power.

**Table 5:** Performance comparison of the designed 122 GHz FMCW Front-end with similar reported works in Silicon technologies.

Ref.	[69]	[49]	[70]	[71]	[72]	[73]	This*
Frequency (GHz)	94	122	125	146	122	122	122
Technology	0.13 $\mu$ m SiGe	0.13 $\mu$ m SiGe	0.13 $\mu$ m SiGe	0.18 $\mu$ m SiGe	0.13 $\mu$ m SiGe	0.13 $\mu$ m SiGe	0.13 $\mu$ m SiGe
Level of integration	Int. VCO w/ Freq. Mult 4-TX 4-RX	Ext. LO w/ Freq Mult, BPSK Mod.	Ext. LO w/ Freq Mult.	Int. VCO w/ Freq. Mult	Ext. LO w/ Freq Mult, QPSK Mod. 2-RX 1-TX	Fund. VCO Digital Control & Calibration	Ext. LO w/ Freq Mult.
Ptx (dBm)	6.4	5	3.2	-1	12	-2.5	10.1
GRx (dB)	25	21	15.5 <sup>+</sup>	8.3*	14	25	31.1
SSB Rx NF (dB)	12.5	12.7*	9.5 <sup>+</sup>	19.3*	11*	N/A	9.9
Pdc (W)	0.8	0.627	0.395	0.650	1.2	0.38	0.24
Mod. BW (GHz)	4	10	30	48	20	4	20
Area (mm <sup>2</sup> )	7.4	10.14**	3.1**	3.86	9	2.7	4

\* Simulation \*\* Including on-chip antenna(s) + LNA-only

## 4 Future Work & Conclusion

### 4.1 Summary of Work

For this thesis work, a 122-GHz FMCW RADAR Front-End for high-resolution sensing applications, such as hand-gesture recognition, is designed. The full-system and the breakouts of critical sub-blocks were taped-out in IHP Microelectronics' 130nm SiGe:C BiCMOS technology, SG13G2. The design considerations in the implementation of a short-range, high-resolution FMCW RADAR sensor are discussed in detail, with the necessary theoretical background behind remote sensing and FMCW RADAR covered in Chapters 1 and 2. The design steps, methodology, and the simulation results for the sub-blocks; LNA, PA, Mixer, x16 frequency multiplier, single-ended to differential 2-way power divider, are presented in detail. The system implementation steps, as well as the simulation results of the full-system, are presented with a comparison to the state-of-the-art RADAR systems. The designed system achieves one of the highest Tx output powers while maintaining a low DC-power consumption. The designed Front-end also achieves the highest Rx conversion-gain excluding baseband circuitries and a low SSB NF. The system can operate with a modulation BW up to 20 GHz to enable a range resolution on mm-scale.

### 4.2 Future Works

Due to unforeseen events, the fabrication process of the designed chips was delayed. Since the fabricated chips were not available at the time of this thesis, only the simulation results of the designs are presented. The immediate future work is the measurement and verification of the designed sub-blocks and system. The breakouts of LNA, PA, and Mixer will be available for measurement. For characterization purposes, standalone versions of Marchand balun and single-ended to differential power divider is also sent to fabrication.

For the first system prototype, the measurements will be performed on the probe station. An example measurement setup is shown in Figure 57. The external LO is supplied from the TI LMX2594 VCO-PLL chain, which can be programmed for an output frequency of 6.875-8.125 GHz. The output of the VCO-PLL is brought

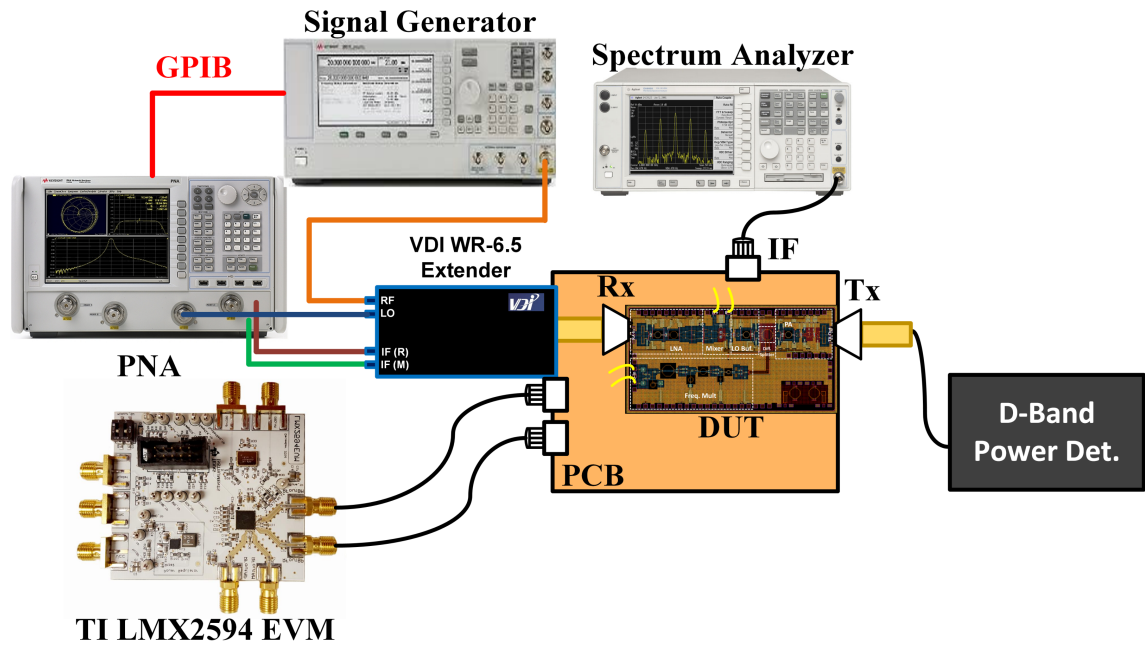


**Figure 57:** Possible measurement setup of the designed system.

to the PCB differentially, using two end-launch connectors. The differential LO is connected to the chip with bondwires. The Tx output power can be measured with the use of an Infinity GSG-75 WR6.5 Probe, and a D-Band power detector (Erickson PM5). The Tx output power can also be measured with the use of a discrete d-band sub-harmonic mixer. Receiver CG can be measured as follows: Using a D-band frequency extender, the Rx input can be supplied from a signal generator. Since the LO is supplied from the VCO-PLL chain, the downconverted IF signal can be tracked in the frequency domain with the use of a spectrum analyzer. Since the IF signal is at a very low frequency, it can be connected to the PCB with bondwires without any significant drawbacks. Noise figure measurements can be performed by swapping the Signal Generator and extender with a D-Band noise source and Faraday Isolator.

Long-term future work is the implementation of Tx and Rx antennas to enable a real-world demonstration of the designed system. Implementation of on-chip antennas was planned in the initial design process, however, they were omitted later for the first prototype. There are different ways of implementing an antenna structure for the system. One way is to use the localized backside etching (LBE) provided within the SG13G2 process to acquire superior antenna efficiencies at D-band frequencies, as reported in [49]. Differential antenna structures are preferred for on-chip imple-



**Figure 58:** Antenna in package approach.

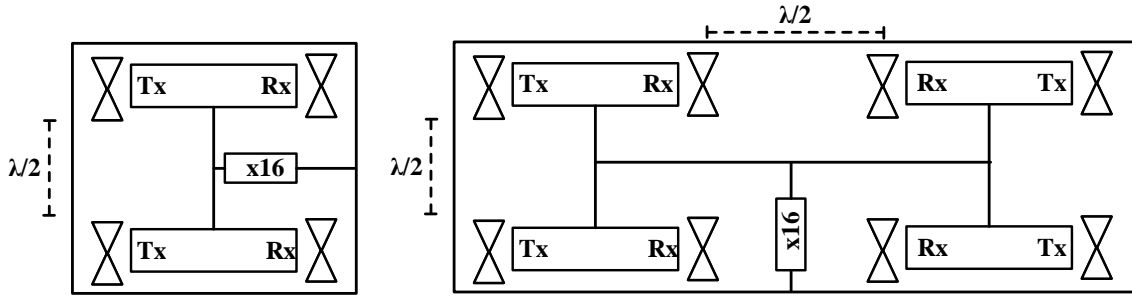


**Figure 59:** 2x1 Array implementation (Left) 2x2 Array implementation (Right)

mentation since the designed chip already uses differential topology, eliminating the need for baluns. The use of bondwire antennas is also reported at 120 GHz [74], which is also a possibility for implementing an on-chip antenna solution. Another solution is to use wirebond transitions to implement the antenna on a different substrate (LTCC), as shown in Figure 58. This could prove to be more costly for the system as bondwires would introduce significant loss at 120 GHz range.

The design of on-chip antennas would also allow a scalable approach for the designed system. By separating the multiplier from the designed system, the rest of the Tx/Rx chain can easily be implemented in an array formation, as shown in Figure 59 for 2x1 and 2x2 configurations with on-chip bow-tie antennas. In this configuration, the reconfigurable PA can be used to synthesize virtual antenna elements and enable MIMO RADAR operation. The compact layout of the TRX cell without the multiplier allows the building of wafer-scale arrays with greater number of elements.

## References

- [1] P. A. P. Association, “History of aerial photography.” [https://www.professionalaerialphotographers.com/content.aspx?page\\_id=22&club\\_id=808138&module\\_id=158950](https://www.professionalaerialphotographers.com/content.aspx?page_id=22&club_id=808138&module_id=158950). Accessed: 2020-07-11.
- [2] “The bavarian pigeon corps (1903).” <http://www.geog.ucsb.edu/~jeff/115a/history/pigeonremotesensing.html>. Accessed: 2020-07-11.
- [3] NASA, “What in the world is remote sensing?.” [https://www.nasa.gov/audience/forstudents/k-4/home/F\\_What\\_is\\_Remote\\_Sensing.html](https://www.nasa.gov/audience/forstudents/k-4/home/F_What_is_Remote_Sensing.html). Accessed: 2020-07-11.
- [4] F. Ulaby and D. Long, *Microwave Radar and Radiometric Remote Sensing*. Norwood, MA: Artech House, 2015.
- [5] R. Loudon, *The Quantum Theory of Light*. OUP Oxford, 2000.
- [6] J. M. Palmer and B. G. Grant, *The Art of Radiometry*. PM184, Bellingham: SPIE, 2009.
- [7] M. Skolnik, *Introduction to Radar Systems*. Electrical engineering series, McGraw-Hill, 2001.
- [8] M. Guarnieri, “The early history of radar [historical],” *IEEE Industrial Electronics Magazine*, vol. 4, pp. 36–42, Sep. 2010.
- [9] E. Britannica, “History of radar.” <https://www.britannica.com/technology/radar/History-of-radar>. Accessed: 2020-07-11.
- [10] R. Martin, C. Schuetz, T. Dillon, D. Mackrides, P. Yao, K. Shreve, C. Harrierty, A. Zablocki, B. Overmiller, P. Curt, J. Bonnett, A. Wright, J. Wilson, S. Shi, and D. Prather, “Optical up-conversion enables capture of millimeter-wave video with an ir camera,” *SPIE Newsroom*, 08 2012.
- [11] J. D. Cressler, “Sige hbt technology: a new contender for si-based rf and microwave circuit applications,” *IEEE Transactions on Microwave Theory and Techniques*, vol. 46, no. 5, pp. 572–589, 1998.
- [12] H. J. Liebe, T. Manabe, and G. A. Hufford, “Millimeter-wave attenuation and delay rates due to fog/cloud conditions,” *IEEE Transactions on Antennas and Propagation*, vol. 37, no. 12, pp. 1617–1612, 1989.
- [13] K. Ramasubramanian and K. Ramaiah, “Moving from legacy 24 ghz to state-of-the-art 77-ghz radar,” *ATZelektronik worldwide*, vol. 13, pp. 46–49, Jun 2018.
- [14] B. Ustundag, E. Turkmen, A. Burak, B. Gungor, H. Kandis, B. Cetindogan, M. Yazici, M. Kaynak, and Y. Gurbuz, “Front-end blocks of a w-band dicke radiometer in sige bicmos technology,” *IEEE Transactions on Circuits and Systems II: Express Briefs*, 2020. doi: 10.1109/TCSII.2020.2968313.
- [15] E. Turkmen, B. Cetindogan, M. Yazici, and Y. Gurbuz, “Design and characterization of a d-band sige hbt front-end for dicke radiometers,” *IEEE Sensors Journal*, vol. 20, no. 9, pp. 4694–4703, 2020.

- [16] K. A. Smith, C. Csech, D. Murdoch, and G. Shaker, "Gesture recognition using mm-wave sensor for human-car interface," *IEEE Sensors Letters*, vol. 2, no. 2, pp. 1–4, 2018.
- [17] F. Maiwald, O. Montes, S. Padmanabhan, D. Michaels, A. Kitiyakara, R. Jarnot, S. T. Brown, D. Dawson, A. Wu, W. Hatch, P. Stek, and T. Gaier, "Reliable and stable radiometers for jason-3," *IEEE Journal of Selected Topics in Applied Earth Observations and Remote Sensing*, vol. 9, no. 6, pp. 2754–2762, 2016.
- [18] L. Martin, "An/fps 117 long-range air surveillance radars." <https://www.lockheedmartin.com/content/dam/lockheed-martin/rms/documents/ground-based-air-surveillance-radars/FPS-117-fact-sheet.pdf>. Accessed: 2020-07-11.
- [19] A. Natarajan, A. Komijani, X. Guan, A. Babakhani, and A. Hajimiri, "A 77-ghz phased-array transceiver with on-chip antennas in silicon: Transmitter and local lo-path phase shifting," *IEEE Journal of Solid-State Circuits*, vol. 41, no. 12, pp. 2807–2819, 2006.
- [20] C. Wagner, H. Forstner, G. Haider, A. Stelzer, and H. Jager, "A 79-ghz radar transceiver with switchable tx and lo feedthrough in a silicon-germanium technology," in *2008 IEEE Bipolar/BiCMOS Circuits and Technology Meeting*, pp. 105–108, 2008.
- [21] N. Van Thienen, Y. Zhang, and P. Reynaert, "Bidirectional communication circuits for a 120-ghz pmf data link in 40-nm cmos," *IEEE Journal of Solid-State Circuits*, vol. 53, no. 7, pp. 2023–2031, 2018.
- [22] H. Kandis, "77 ghz sige bicmos fmcw radar for automotive applications," Master's thesis, Sabanci University, 7 2019.
- [23] H. L. Lee, W. Lim, K. Oh, and J. Yu, "24 ghz balanced doppler radar front-end with tx leakage canceller for antenna impedance variation and mutual coupling," *IEEE Transactions on Antennas and Propagation*, vol. 59, no. 12, pp. 4497–4504, 2011.
- [24] D. K. (auth.), *Millimeter-Wave Receiver Concepts for 77 GHz Automotive Radar in Silicon-Germanium Technology*. Springer Briefs in Electrical and Computer Engineering, Springer-Verlag New York, 1 ed., 2012.
- [25] H. J. Ng, R. Feger, and A. Stelzer, "A fully-integrated 77-ghz uwb pseudo-random noise radar transceiver with a programmable sequence generator in sige technology," *IEEE Transactions on Circuits and Systems I: Regular Papers*, vol. 61, no. 8, pp. 2444–2455, 2014.
- [26] A. Cathelin, "Fully depleted silicon on insulator devices cmos: The 28-nm node is the perfect technology for analog, rf, mmw, and mixed-signal system-on-chip integration," *IEEE Solid-State Circuits Magazine*, vol. 9, no. 4, pp. 18–26, 2017.
- [27] J. D. Cressler, *Silicon-Germanium Heterojunction Bipolar Transistors*. Artech Print on Demand, 1st edition ed., 2002.

- [28] H. Rücker, B. Heinemann, and A. Fox, “Half-terahertz sige bicomos technology,” in *2012 IEEE 12th Topical Meeting on Silicon Monolithic Integrated Circuits in RF Systems*, pp. 133–136, Jan 2012.
- [29] J. Dickmann, J. Klappstein, M. Hahn, N. Appenrodt, H. Bloecher, K. Werber, and A. Sailer, “”automotive radar the key technology for autonomous driving: From detection and ranging to environmental understanding”,” in *2016 IEEE Radar Conference (RadarConf)*, pp. 1–6, May 2016.
- [30] P. Molchanov, S. Gupta, K. Kim, and K. Pulli, “Multi-sensor system for driver’s hand-gesture recognition,” in *2015 11th IEEE International Conference and Workshops on Automatic Face and Gesture Recognition (FG)*, vol. 1, pp. 1–8, 2015.
- [31] Z. Peng, J. M. Muñoz-Ferreras, Y. Tang, C. Liu, R. Gómez-García, L. Ran, and C. Li, “A portable fmcw interferometry radar with programmable low-if architecture for localization, isar imaging, and vital sign tracking,” *IEEE Transactions on Microwave Theory and Techniques*, vol. 65, pp. 1334–1344, April 2017.
- [32] N. Long, K. Wang, R. Cheng, K. Yang, W. Hu, and J. Bai, “Assisting the visually impaired: multitarget warning through millimeter wave radar and RGB-depth sensors,” *Journal of Electronic Imaging*, vol. 28, no. 1, pp. 1 – 15, 2019.
- [33] G. A. T. Warren L. Stutzman, *Antenna Theory and Design*. Wiley, 3 ed., 2012.
- [34] E. Knott, J. Schaeffer, and M. Tully, *Radar Cross Section*. Electromagnetics and Radar Series, Institution of Engineering and Technology, 2004.
- [35] S. Ayhan, S. Scherr, P. Pahl, T. Kayser, M. Pauli, and T. Zwick, “High-accuracy range detection radar sensor for hydraulic cylinders,” *IEEE Sensors Journal*, vol. 14, no. 3, pp. 734–746, 2014.
- [36] K. Thurn, R. Ebel, and M. Vossiek, “Noise in homodyne fmcw radar systems and its effects on ranging precision,” in *2013 IEEE MTT-S International Microwave Symposium Digest (MTT)*, pp. 1–3, 2013.
- [37] M. Pichler, A. Stelzer, P. Gulden, and M. Vossiek, “Influence of systematic frequency-sweep non-linearity on object distance estimation in fmcw/fscw radar systems,” in *2003 33rd European Microwave Conference*, pp. 1203–1206, 2003.
- [38] A. Frischen, J. Hasch, and C. Waldschmidt, “Fmcw ramp non-linearity effects and measurement technique for cooperative radar,” in *2015 European Radar Conference (EuRAD)*, pp. 509–512, 2015.
- [39] V. C. Chen, F. Li, S. . Ho, and H. Wechsler, “Micro-doppler effect in radar: phenomenon, model, and simulation study,” *IEEE Transactions on Aerospace and Electronic Systems*, vol. 42, no. 1, pp. 2–21, 2006.
- [40] V. C. Chen, “Doppler signatures of radar backscattering from objects with micro-motions,” *IET Signal Processing*, vol. 2, no. 3, pp. 291–300, 2008.
- [41] V. C. Chen, *The Micro-Doppler effect in radar*. Artech House, 2 ed., 2019.

- [42] I. V. Mikhelson, S. Bakhtiari, T. W. Elmer, II, and A. V. Sahakian, “Remote sensing of heart rate and patterns of respiration on a stationary subject using 94-ghz millimeter-wave interferometry,” *IEEE Transactions on Biomedical Engineering*, vol. 58, no. 6, pp. 1671–1677, 2011.
- [43] W. Ye and H. Chen, “Human activity classification based on micro-doppler signatures by multiscale and multitask fourier convolutional neural network,” *IEEE Sensors Journal*, vol. 20, no. 10, pp. 5473–5479, 2020.
- [44] H. Mohammadnezhad, H. Wang, A. Cathelin, and P. Heydari, “A 115–135-ghz 8psk receiver using multi-phase rf-correlation-based direct-demodulation method,” *IEEE Journal of Solid-State Circuits*, vol. 54, no. 9, pp. 2435–2448, 2019.
- [45] H. Wang, H. Mohammadnezhad, and P. Heydari, “Analysis and design of high-order qam direct-modulation transmitter for high-speed point-to-point mm-wave wireless links,” *IEEE Journal of Solid-State Circuits*, vol. 54, no. 11, pp. 3161–3179, 2019.
- [46] H. Jia, L. Kuang, W. Zhu, Z. Wang, F. Ma, Z. Wang, and B. Chi, “A 77 ghz frequency doubling two-path phased-array fmcw transceiver for automotive radar,” *IEEE Journal of Solid-State Circuits*, vol. 51, no. 10, pp. 2299–2311, 2016.
- [47] D. Mittelstrass, D. Steinbuch, T. Walter, C. Waldschmidt, and R. Weigel, “Dc-offset compensation in a bistatic 77ghz-fmcw-radar,” in *The 7th European Radar Conference*, pp. 447–450, Sep. 2010.
- [48] P. Hügler, M. Geiger, and C. Waldschmidt, “Rcs measurements of a human hand for radar-based gesture recognition at e-band,” in *2016 German Microwave Conference (GeMiC)*, pp. 259–262, 2016.
- [49] H. J. Ng, M. Kucharski, W. Ahmad, and D. Kissinger, “Multi-purpose fully differential 61- and 122-ghz radar transceivers for scalable mimo sensor platforms,” *IEEE Journal of Solid-State Circuits*, vol. 52, no. 9, pp. 2242–2255, 2017.
- [50] M. Vigilante and P. Reynaert, “On the design of wideband transformer-based fourth order matching networks for  $E$ -band receivers in 28-nm cmos,” *IEEE Journal of Solid-State Circuits*, vol. 52, no. 8, pp. 2071–2082, 2017.
- [51] T. Heller, E. Cohen, and E. Socher, “A 102–129-ghz 39-db gain 8.4-db noise figure i/q receiver frontend in 28-nm cmos,” *IEEE Transactions on Microwave Theory and Techniques*, vol. 64, no. 5, pp. 1535–1543, 2016.
- [52] A. C. Ulusoy, P. Song, W. T. Khan, M. Kaynak, B. Tillack, J. Papapolymerou, and J. D. Cressler, “A sige d-band low-noise amplifier utilizing gain-boosting technique,” *IEEE Microwave and Wireless Components Letters*, vol. 25, no. 1, pp. 61–63, 2015.

- [53] E. Turkmen, A. Burak, A. Guner, I. Kalyoncu, M. Kaynak, and Y. Gurbuz, “A sige hbt  $d$ -band lna with butterworth response and noise reduction technique,” *IEEE Microwave and Wireless Components Letters*, vol. 28, no. 6, pp. 524–526, 2018.
- [54] Keng Leong Fong and R. G. Meyer, “Monolithic rf active mixer design,” *IEEE Transactions on Circuits and Systems II: Analog and Digital Signal Processing*, vol. 46, no. 3, pp. 231–239, 1999.
- [55] D. Alldred, B. Cousins, and S. P. Voinigescu, “A 1.2v, 60-ghz radio receiver with on-chip transformers and inductors in 90-nm cmos,” in *2006 IEEE Compound Semiconductor Integrated Circuit Symposium*, pp. 51–54, 2006.
- [56] C. M. Grens, J. D. Cressler, J. M. Andrews, Qingqing Liang, and A. J. Joseph, “Reliability issues associated with operating voltage constraints in advanced sige hbts,” in *2005 IEEE International Reliability Physics Symposium, 2005. Proceedings. 43rd Annual.*, pp. 409–414, 2005.
- [57] R. Feger, C. Wagner, S. Schuster, S. Scheiblhofer, H. Jager, and A. Stelzer, “A 77-ghz fmcw mimo radar based on an sige single-chip transceiver,” *IEEE Transactions on Microwave Theory and Techniques*, vol. 57, no. 5, pp. 1020–1035, 2009.
- [58] A. Mukherjee, W. Liang, P. Sakalas, A. Pawlak, and M. Schröter, “W-band low-power millimeter-wave low noise amplifiers (lnas) using sige hbts in saturation region,” in *2019 IEEE 19th Topical Meeting on Silicon Monolithic Integrated Circuits in RF Systems (SiRF)*, pp. 1–4, 2019.
- [59] B. Philippe and P. Reynaert, “24.7 a 15dbm 12.8%-pae compact d-band power amplifier with two-way power combining in 16nm finfet cmos,” in *2020 IEEE International Solid- State Circuits Conference - (ISSCC)*, pp. 374–376, 2020.
- [60] H. S. Son, C. J. Lee, D. M. Kang, T. H. Jang, H. S. Lee, S. H. Kim, C. W. Byeon, and C. S. Park, “A d-band cmos power amplifier for wireless chip-to-chip communications with 22.3 db gain and 12.2 dbm p1db in 65-nm cmos technology,” in *2018 IEEE Topical Conference on RF/Microwave Power Amplifiers for Radio and Wireless Applications (PAWR)*, pp. 35–38, 2018.
- [61] Z. Hu, G. Sarris, C. De Martino, M. Spirito, and E. McCune, “Design and linearity analysis of a d-band power amplifier in 0.13  $\mu\text{m}$  sige bicmos technology,” in *2017 IEEE Compound Semiconductor Integrated Circuit Symposium (CSICS)*, pp. 1–4, 2017.
- [62] J. Romstadt, V. Lammert, N. Pohl, and V. Issakov, “Transformer-coupled d-band pa with 11.8 dbm  $P_{\text{sat}}$  and 6.3% pae in 0.13 $\mu\text{m}$  sige bicmos,” in *2020 IEEE 20th Topical Meeting on Silicon Monolithic Integrated Circuits in RF Systems (SiRF)*, pp. 77–80, 2020.
- [63] S. Muralidharan, K. Wu, and M. Hella, “A compact low loss single-ended to two-way differential power divider/combiner,” *IEEE Microwave and Wireless Components Letters*, vol. 25, no. 2, pp. 103–105, 2015.

- [64] D. Shim, W. Choi, J. Lee, and K. K. O, “Self-dynamic and static biasing for output power and efficiency enhancement of complementary antiparallel diode pair frequency tripler,” *IEEE Microwave and Wireless Components Letters*, vol. 27, no. 12, pp. 1110–1112, 2017.
- [65] T. Instruments, “Lmx2594 15-ghz wideband pllatinum™ rf synthesizer with phase synchronization and jesd204b support.” <https://www.ti.com/product/LMX2594#tech-docs>, note = Accessed: 2020-08-04.
- [66] N. Oz and E. Cohen, “A compact 105–130 ghz push-push doubler, with 4dbm psat and 18% efficiency in 28nm cmos,” in *2015 10th European Microwave Integrated Circuits Conference (EuMIC)*, pp. 101–104, 2015.
- [67] M. Schroter and A. Chakravorty, *Compact Hierarchical Bipolar Transistor Modeling with Hicup*. International series on advances in solid state electronics and technology, World Scientific, 2010.
- [68] W. Hung, H. Chen, S. Chou, and L. Lu, “An 18dbm transmitter frontend with 29% pae for 24ghz fmcw radar applications,” in *2012 IEEE Radio Frequency Integrated Circuits Symposium*, pp. 137–140, 2012.
- [69] A. Townley, P. Swirhun, D. Titz, A. Bisognin, F. Gianesello, R. Pilard, C. Luxey, and A. M. Niknejad, “A 94-ghz 4tx–4rx phased-array fmcw radar transceiver with antenna-in-package,” *IEEE Journal of Solid-State Circuits*, vol. 52, no. 5, pp. 1245–1259, 2017.
- [70] S. Yuan and H. Schumacher, “110–140-ghz single-chip reconfigurable radar frontend with on-chip antenna,” in *2015 IEEE Bipolar/BiCMOS Circuits and Technology Meeting - BCTM*, pp. 48–51, 2015.
- [71] T. Jaeschke, C. Bredendiek, S. Küppers, and N. Pohl, “High-precision d-band fmcw-radar sensor based on a wideband sige-transceiver mmic,” *IEEE Transactions on Microwave Theory and Techniques*, vol. 62, no. 12, pp. 3582–3597, 2014.
- [72] M. Furqan, F. Ahmed, and A. Stelzer, “A d-band fully-integrated 2-rx, 1-tx fmcw radar sensor with 13dbm output power,” in *2019 14th European Microwave Integrated Circuits Conference (EuMIC)*, pp. 100–103, 2019.
- [73] W. Debski, W. Winkler, Y. Sun, M. Marinkovic, J. Borngräber, and J. C. Scheytt, “120 ghz radar mixed-signal transceiver,” in *2012 7th European Microwave Integrated Circuit Conference*, pp. 191–194, 2012.
- [74] N. Deferm and P. Reynaert, “A 120 ghz fully integrated 10 gb/s short-range star-qam wireless transmitter with on-chip bondwire antenna in 45 nm low power cmos,” *IEEE Journal of Solid-State Circuits*, vol. 49, no. 7, pp. 1606–1616, 2014.